Concepts and principles of self-n-doping in perylene diimide chromophores for applications in biochemistry, energy harvesting, energy storage, and catalysis

Daniel Powell and Luisa Whittaker-Brooks*

Department of Chemistry, University of Utah, Salt Lake City, Utah, 84112

ABSTRACT

Self-doping is an important method of increasing carrier concentrations in organic electronics that completely eliminates the need to tailor host—dopant miscibility; a necessary step when employing molecular dopants. Self-n-doping can be accomplished using amine or ammonium moieties as an electron source, and is being incorporated into an ever-increasingly diverse range of organic materials spanning many applications. Self-n-doped materials have demonstrated good, and in many cases, benchmark performances in a variety of applications. However, an in-depth review of the method is lacking. Perylene diimide (PDI) chromophores are an important mainstay in the semiconductor literature with well-known structure-function characteristics and are also one of the most widely utilized scaffolds for self-n-doping. In this review, we describe the unique properties of self-n-doped PDIs, delineate structure-function relationships, and discuss self-n-doped PDI performance in a range of applications. In particular, the impact of amine/ammonium incorporation into the PDI scaffold on doping
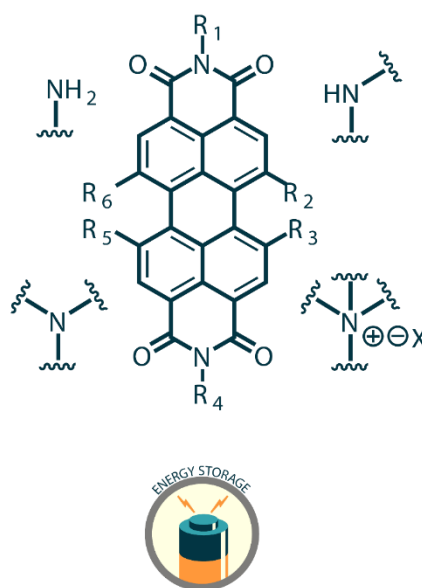
efficiency is reviewed with regard to attachment mode, tether distance, counterion selection, and steric encumbrance. Self-n-doped PDIs are a unique set of PDI structural derivatives whose properties are amenable to a broad range of applications in biochemistry, solar energy conversion, thermoelectric modules, batteries, and photocatalysis. Finally, we discuss challenges and the future outlook of self-n-doping principles.

1. INTRODUCTION

Doping is essential in achieving any functional organic semiconductor with a high carrier concentration regardless of its p/n-type categorization. One common method of n-type doping in organic semiconductors is to treat them with inorganic species that have relatively small ionization potentials (e.g. hydrazine vapor, iodine vapor, sodium metal, etc.) or, more commonly, to combine them with other organic compounds with relatively low electron affinity.[1–4] This is typically accomplished by combining the dopant with the host in the solution phase and casting the mixture into thin films. In many instances, the dopants tend to aggregate together and phase segregate from the host, ultimately altering the morphology of the resulting solid-state matrix. Thus, when the solubility properties of the host and the dopant are even modestly dissimilar from one another, it presents a significant challenge for the fabrication of functional organic materials.[5] Obtaining a homogenous mixture of dopant and organic semiconductor in solution is non-trivial, and the process is made even more challenging when accounting for the role of solvent evaporation during film casting. Improving host/dopant miscibility is a prominent topic in the field. Researchers must select from a variety of available methods to optimize their procedure, and the process is generally approached through trial and error.[6–8] Self-doping has emerged as a promising method of tuning carrier concentrations in small molecule organic semiconductors because it axiomatically mitigates dopant phase segregation and aggregation.

Any single molecule or polymer subunit that contains both an electron donor and electron acceptor can generally be regarded as a self-doping system, and its p-type or n-type categorization will depend on the ionization potentials of the donor and acceptor components. While self-p-doping has long been utilized in polymers,[9–11] self-n-doping remains comparatively underutilized. It has long been known that small molecules can be functionalized with various alkylamino substituents to create intramolecular donor-acceptor scaffolds.[12–17] However, only in more recent years has the technique risen to a level of prominence that has warranted an in-depth review. Primary, secondary, and tertiary amines, as well as quaternary ammonium salts have been incorporated into a wide variety of small molecule and polymer scaffolds for their ability to act as covalently bound dopants. Self-n-doping amine and ammonium moieties have been incorporated as molecular components in a range of materials research fields, such as in low-dimensional perovskite-related hybrids, electron transporting materials in solar cells, thermoelectric composites, work function modifiers, and more.[18–32] While the chemical structures of the self-n-doped semiconductors seen across the literature are diverse, the most common derivatives are fullerenes, perylene diimides, naphthalene diimides, and fluorenes as shown in **Figure 1**. Each scaffold shown here exhibits a unique set of intrinsic physicochemical properties. The manner in which these properties are altered by the addition of amine/ammonium functional groups is non-trivial, and indeed may not be universal among the various host materials. For example, the limitations of anion reduction in self-n-doped fullerenes are disputed,[33–35] but well established in self-n-doped fluorene derivatives.[36] In the interest of providing a thorough and in-depth review, we have limited our discussion to what is arguably the most common scaffold: perylene diimides (PDIs).

N,N'-disubstituted perylene-3,4,9,10-tetracarboxylic acid imides (PDIs) are chromophores belonging to the rylene dye family, and were used as red vat dyes following their initial development in 1913. By the late 1950s, PDIs would become fully commercialized as pigments commonly used in automobile paints and many other dye applications.[37] Today, these dyes are used in ways never imagined by their inventors, and are one of the most heavily investigated small molecules in the organic semiconductor community.[38–40] These chromophores have found application in a surprising breadth of fields including fluorescence spectroscopy, supramolecular assemblies, sensing, and more.[41–44] Ease of synthesis, synthetic modularity, thermal stability, high oscillator strengths, and large fluorescence quantum yields are a few of the reasons these dyes have garnered so much attention.[45] The rise in interest in PDIs has naturally coincided with the field growing progressively more specialized. A given application requires very specific material properties. Consequently, much of the information available on self-n-doped PDIs is fragmented into application-specific citation clusters. This review presents self-n-doped materials as a unique class of structural derivate whose unique and exciting physicochemical properties merit their distinct categorization. We anticipate that the information reviewed here will be of use to researchers spanning a breadth of fields as we discuss this emerging, and often misunderstood, material class.

Self-n-doped PDIs are characterized by a perylene diimide scaffold functionalized with one or more amine or ammonium substituents at one or more R-group locations, which we refer to as N-PDIs (amino-functionalized PDIs) as shown in **Figure 1**. Here, one or more R groups will contain an amine or ammonium salt within any carbon chain or cycle, while the remaining R groups may be composed of hydrogen, any carbon chain, any carbon cycle, or any heteroatom. X corresponds to any monovalent or divalent anionic counterion. Incorporating amines or ammonium salts into

the PDI scaffold strongly affects the material's excited state dynamics and electronic properties. Consequently, PDIs have exhibited great promise in a wide breadth of applications both in solution and in the solid-state, such as nano and sub-nanomolar chemical probes for biological and chemical sensing, protein inhibition, photocatalysis, controllable self-assembly, thin-film polarizers, photovoltaics, thermoelectrics, and batteries.[46–56] A selection of these applications is discussed in greater detail in section 3. We have consolidated the information available on N-PDIs in order to provide insights into the functionality of self-n-doped materials and delineate how these properties make them promising candidates in such a wide range of applications.
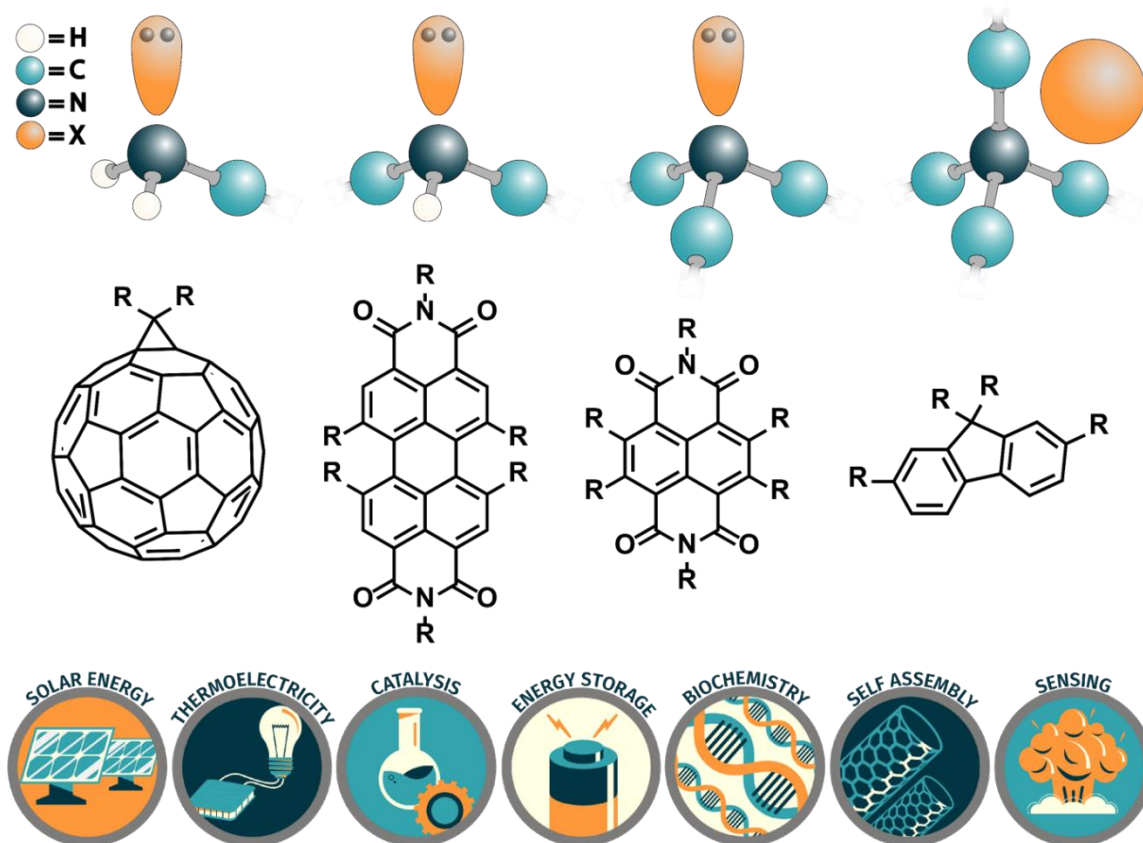
Figure 1. Primary, secondary, and tertiary amines as well as quaternary ammonium salt dopant structures shown at the top are accompanied by the generalized chemical structures of acceptor motifs commonly observed in the literature. From left to right, fullerene, perylene diimide, naphthalene diimide, and fluorene (center). Animated depictions of the many applications of these materials are shown at the bottom.

2. GENERAL PROPERTIES OF PDIs

2.1 Monomers

The photophysical properties of PDIs are rich and have been the subject of critical investigation.[57,58] The acceptor-donor-acceptor (A-D-A) the PDI scaffold sandwiches the electron abundant perylene between inductively withdrawing dicarboxylic acid imides, which induces a bathochromic shift in the absorption spectrum by ~100 nm relative to perylene. The characteristic absorption peaks of PDI, shown in **Figure 2A**, originate from the perylene core.[59] These absorption peaks correspond to ground state $S_0{\rightarrow}S_1$ Franck-Condon vibronic transitions 0-0, 0-1, 0-2, and 0-3 that are typically found in the range of ~420 to ~530 nm, and the emission spectrum is a mirror-image of the absorption spectrum.[60,61] Transient absorption characteristics of PDIs are shown in **Figure 2B**, which typically involve an $S_0{\rightarrow}S_1$ ground state (**^{0}N**) bleach from ~420-530 nm that is often accompanied by stimulated emission at ~590 nm. Concomitant with the ground state bleach is the growth of an absorption transient peaking at ~690 nm and tailing into the NIR attributed to the excited singlet state (**^{1*}N**) absorption transient $S_1{\rightarrow}S_n$ (n > 1).[62] In general, **^{1*}N** quickly relaxes (a few ns) back to the ground state (**^{0}N**). Intersystem crossing is typically not observed in PDI monomers as the triplet state energy level is relatively low-lying from S_1, and their rigidity makes

radiation-less internal conversion very slow. PDI monomers thus typically exhibit fluorescence quantum yields near unity and have excellent photostability.[63] However, there are cases in which the triplet intermediate may be accessed. For example, in thionated PDI systems or those within a coordination complex.[64–66]

The highest occupied molecular orbital (HOMO) and the lowest unoccupied molecular orbital (LUMO) are localized to the perylene core as shown in **Figure 2C**. Functionalization of the perylene core is the primary method of altering the HOMO/LUMO energy levels of the PDI chromophore. Hypsochromic or bathochromic shifting and dramatic shifts to redox potential can be observed depending on the electron-withdrawing or donating ability of the added group. As a result, the colors of fully solvated PDIs in solution are strongly dependent on the choice of the functional group. The energy of the $S_0 \rightarrow S_1$ transition remains largely unchanged when functionalizing PDIs at the imide positions due to the transverse node in the core HOMO and LUMO orbitals of the perylene scaffold. As such, the imide groups are not electrically connected to the core.[45] More recent work has shown that thionation of the dicarboxylic acid imides can also dramatically decrease the LUMO energy, resulting in a red shift of the $S_0 \rightarrow S_1$ transition.[65,67,68]

PDI monomers are also capable of bearing stable radical anions ($\mathbf{R^{\bullet-}}$) and dianions ($\mathbf{D^{\bullet\bullet-}}$). The absorption spectra of a PDI chemically reduced with tetrakis(dimethylamino)ethylene (TDAE) to form $\mathbf{R^{\bullet-}}$, and reduced with cobaltacene (CoCp$_2$) to form $\mathbf{D^{\bullet\bullet-}}$ are shown in **Figure 2D** with $^0\mathbf{N}$ shown for reference.[69] $\mathbf{R^{\bullet-}}$ has six characteristic absorption peaks from ~680 to ~955 nm with the ~955 nm feature corresponding to the $D_0 \rightarrow D_1$ transition and is accompanied by a complex vibronic structure. The singlet transitions of $\mathbf{D^{\bullet\bullet-}}$ are blue-shifted from the doublet transitions of $\mathbf{R^{\bullet-}}$, and has five major peaks from ~530-720 nm. Gosztola et al. has shown the lifetimes of $^{2*}\mathbf{R^{\bullet-}}$ excited states are generally much shorter than $^{1*}\mathbf{N}$, which likely contributes to

the radical anion's exceptional photostability. The absorption spectra of $\mathbf{R^{\bullet-}}$ and $\mathbf{^{1}{}^*N}$ are very similar. This is due to the fact that both excitations occur at similar energies, and both involve the LUMO of $\mathbf{^{0}N}$. In the case of $\mathbf{R^{\bullet-}}$, an electrochemical reduction places an electron in the LUMO of $\mathbf{^{0}N}$, which can then be further excited to $D_0{\rightarrow}D_n$. In the case of $\mathbf{^{1}{}^*N}$, an electron from the HOMO of $\mathbf{^{0}N}$ is excited into the LUMO and can then be further excited to $S_1{\rightarrow}S_n$. The LUMO energy is not strongly affected when it is populated with one or two electrons.[70]
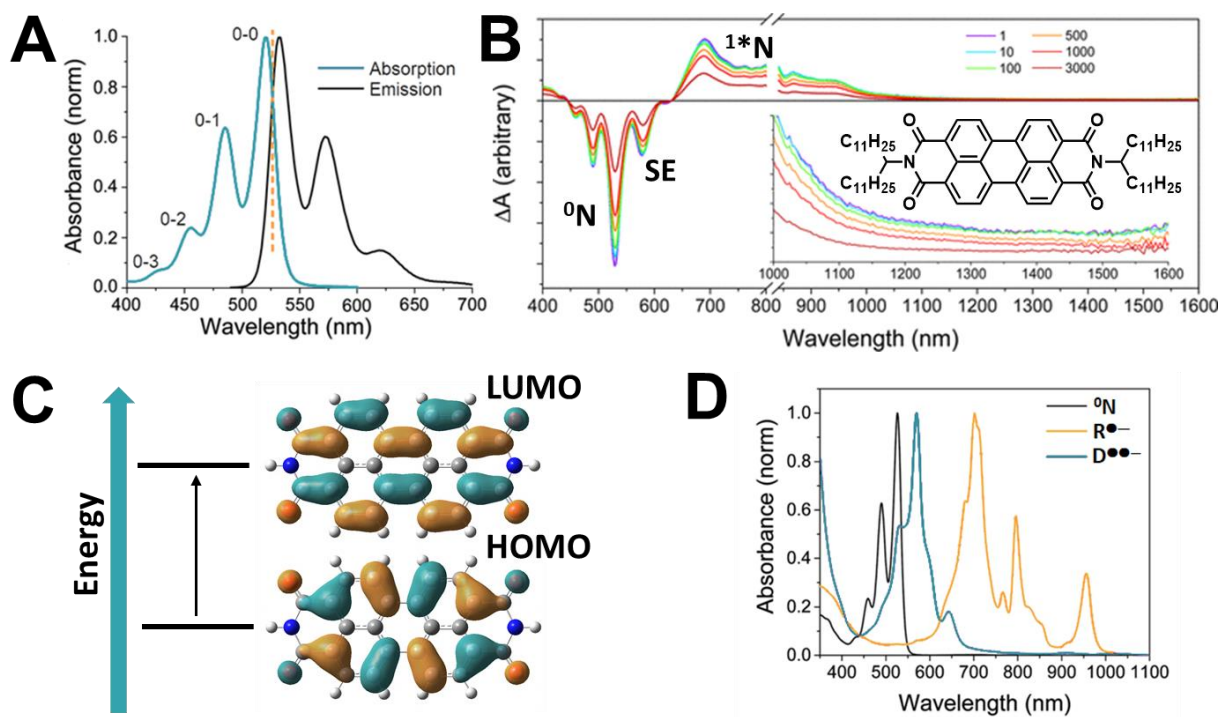

Figure 2. (A) Prototypical absorption/emission spectra of PDI monomers in solution. Adapted with permission from ref. 59. Copyright 2015 American Chemical Society. **(B)** Visible/NIR femtosecond transient absorption spectra of a PDI (structure in inset) excited at 525 nm and time delays reported in ps. Reprinted with permission from ref. 62. Copyright 2014 American Chemical Society. **(C)** Gaussian simulated molecular orbitals of PDI's HOMO and LUMO computed at the DFT level using the B3LYP functional and a 6-311G** basis set. **(D)** Characteristic absorption spectra of PDI monomer (black), PDI radical anion (orange), and

PDI diradical dianion (blue). Adapted from ref. 69. Copyright 2017 The Royal Society of Chemistry.

2.2 Aggregates

The absorption, photoluminescence, and excited state dynamics of PDIs are dramatically altered by their assembly into dimer aggregates and beyond.[71] PDI aggregates are held together by weak van der Waals forces. The ground and excited state energies of aggregates decrease in comparison to monomers because the electrically polarized $S_0 \rightarrow S_1$ exciton induces a strong Coulombic coupling between adjacent chromophores, leading to a decrease in the fluorescence quantum yield in aggregates. Additionally, as chromophores aggregate, the core HOMO and LUMO orbital wavefunctions begin to overlap. The electron-hole pairs are then able to delocalize over all of the chromophores in the dimer, which splits the energy of the $S_0 \rightarrow S_1$ transition into two Frenkel excitonic states. Changes in the absorption spectrum of aggregated chromophores are described by Kasha's exciton coupling theory which relates the relative geometries of adjacent chromophores to their transition dipole moments. In its most basic description, molecules with side-by-side transition dipoles form H-aggregates and their absorption spectra are shifted hypsochromically, while head-to-tail transition dipoles form J-aggregates and their absorption spectra are shifted bathochromically. Additionally, the fluorescence quantum yield decreases in both aggregate systems, while the radiative decay rate is decreased in H-aggregates and enhanced in J-aggregates.[72,73] In reality, the situation is more complex as the Kasha model does not take into account vibronic fine structure and is limited to Coulomb coupling between chromophores. Furthermore, Kazmaier et al. demonstrated that the electron and hole transfer integrals, which dictate the valence and conduction bandwidths, are not entirely described by the overlap between

wave functions on adjacent chromophores, but that they also depend on a quantum interference effect that is highly sensitive to slight transverse chromophore displacements. A schematic energy level diagram depicting the charge transfer between neighboring chromophores is shown in **Figure 3A**, where E_{CT} is the energy of the charge transfer exciton, t_e and t_h are the electron and hole transfer integrals, and J_{CT} is the superexchange interaction of short-range exciton coupling. The hypersensitivity of the electron and hole transfer integrals to chromophore displacements implies that the formation of charge transfer states originating from the perylene core are strongly dependent on stacking profiles. This effect causes aggregates with similar absorption spectra and dimer arrangements to exhibit a wide range of colors; a phenomenon known as crystallochromy.[74] This topic has been discussed elsewhere in detail.[45,75,76]

The degree of H-type aggregation can be measured by the ratio of the 0-0/0-1 vibronic peak intensities, which decreases in H-aggregates. Exemplary absorption spectra of PDI aggregate formation are shown in **Figure 3B**. As PDI concentration increases, the ratio of the 0-0/0-1 absorption peaks decreases due to the formation of H-aggregates (**Figure 3B inset**).[77] Fluorescence quenching in PDI aggregates is also explained by Kasha theory. Wavefunction overlap between core-localized HOMOs and LUMOs of adjacent chromophores facilitates the dissociation of the S_1 state into non-emissive charge transfer (CT) states, which are composed of a pair of charge carriers localized to adjacent chromophores. CT states are non-emissive, resulting in luminescence and phosphorescence quenching, and PDI fluorescence can be tuned by orthogonal solvent blending.[78,79] CT formation is possible because the binding energy of the lowest charge transfer state is high in comparison with the valence and conduction bandwidths.[80] However, a number of $S_1 \rightarrow S_0$ relaxation pathways are possible in PDI aggregates. For example, excimers form when the S_1 excited state creates an internal electric field that causes the spacing between the chromophores

to decrease, or for the dislocation of the chromophores to change such that the degree of wavefunction overlap increases between the neighboring species. The resulting state is lower in energy, causing the photoluminescence to dramatically red-shift, accompanied by an increase in the exciton lifetime. The transformation from the monomer emission at 545 nm to excimer emission at 685 nm is shown in **Figure 3C**. Here, Li et al. titrated a 0.1 μM solution of QA-I (**Figure 3C**) with 0.4 nM of 30 nm silver nanoparticles. The monomer emission is quenched by >90% with an excimer/monomer emission intensity ratio of ~11.[81] This and other relaxation pathways are thus exploitable in PDIs for sensing applications.
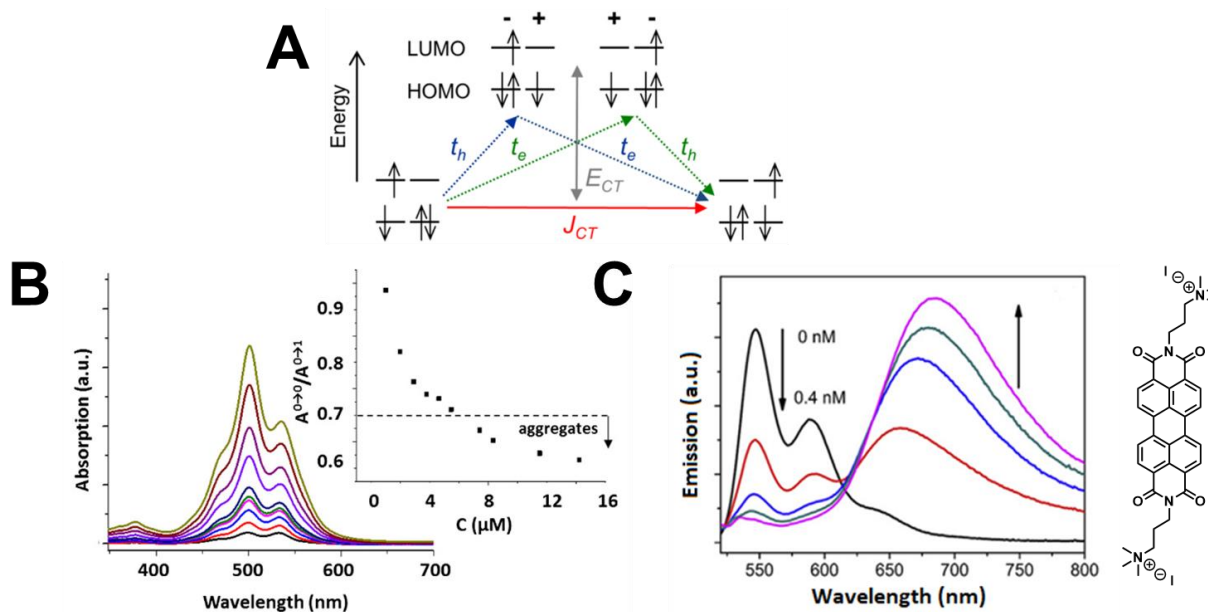

Figure 3. (A) Energy level diagram of charge-transfer coupled chromophores. Reprinted with permission from ref. 76. Copyright 2017 American Chemical Society. **(B)** Prototypical concentration-dependent (1-14 μM) absorption spectra of a PDI in water exhibiting H-type aggregate formation. Peak area ratios of the 0-0/0-1 vibronic peaks are shown in the inset. Reprinted with permission from ref. 77. Copyright 2017 Elsevier. **(C)** Emission spectra of QA-I

(right) titrated with 0-0.4 nM Ag nanoparticles. The nanoparticles induce PDI excimer formation at elevated concentration. Reprinted with permission from ref. 81. Copyright 2018 Elsevier.

3. AMINE/AMMONIUM FUNCTIONALIZED PDIs (N-PDIs)

3.1 Physical properties

The properties outlined in the previous section still hold true for N-PDIs, though with a new layer of added complexity. Electron rich amine and ammonium moieties are capable of doping the electron poor dicarboxylic acid imides of PDI, and has led to the material classification as self-n-doping.[82] However, many examples of N-PDIs in the literature have incorporated these moieties into the PDI scaffold to improve solubility in polar solvents.[83–87] The aggregation dynamics of N-PDIs appear to be highly sensitive to solvent polarity, and their solubility properties tend to vary with dopant architecture. This feature allows their fluorescence properties to be manipulated by solvent blending.[88] Their propensity for fluorescence quenching in polar solvents and blends make them excellent sensors for a wide breadth of analytes using various optical techniques.[89–101] Self-assembly of N-PDIs has also been studied extensively, with aggregation into supramolecular structures being controlled with temperature differences, pH adjustment, metallic directing groups, and structural modifications.[102–111] Many of these phenomena have been reviewed elsewhere.[112] Additionally, many N-PDIs are amphiphilic mesogens capable of forming lyotropic liquid crystal mesophases and have been investigated for use in optical applications.[113–122]

3.2 Self-n-doping mechanism

Due to the unfavorable energy level alignment between the amine/ammonium dopants and the LUMO of PDI, self-n-doping proceeds through a photoinduced electron transfer mechanism. A graphical depiction of the doping mechanism is outlined in **Figure 4A**. First, ground state PDI ^{0}**N** undergoes photoactivation to produce the excited singlet state ^{1}***N**. Here, ^{1}***N** can either relax back to the ground state or undergo reductive quenching by the amino donor to produce the radical anion (**R$^{\bullet-}$**).[123–125] Doping can also be thermally activated in the solid-state. Reilly et al. fabricated thin films of the trimethylammonium hydroxide doped PDI shown in **Figure 4B**. Upon heating to 120ºC for 20 minutes in air, the color of the films changed from a deep red to blue (**Figure 4B inset**) and the film conductivity increased by nearly five orders of magnitude. The absorption spectra of the films show the conversion of the neutral species (**4B$_1$**) to the radical anion (**4B$_2$**). After sitting in air for 10 minutes (**4B$_3$**) and ultimately one day (**4B$_4$**), the radical is gradually oxidized back to the neutral species. Note that the absorption spectrum of an electrochemically generated PDI radical anion is provided as a reference (**4B$_5$**). The researchers also noted that similar changes in the absorption spectrum were observed when leaving the film in a moisture-free desiccator, indicating oxygen is the primary oxidant of the radicals.[123,126,127] Films of these N-PDIs with hydroxide, iodide, and chloride counterions were all found to have higher electrical conductivities after thermal annealing. Work functions of the films were tested with Kelvin probe measurements, finding that the as-cast film has a work function of 4.70 eV. Given a conduction band edge of ~3.9 eV, they concluded that the as-cast films are weakly n-doped. After leaving them in a moisture-free environment for 12 hours the work function shifted to 4.20 eV, indicative of photoactivated doping from ambient light in the laboratory. Following thermal annealing, the work function shifted very near to the conduction band edge to 3.96 eV. Additionally,

thermogravimetric analysis revealed a ~5% mass loss when annealing from 0 ℃→150 ℃ which the authors attributed to water loss, implicating a possible solvent effect.[56]
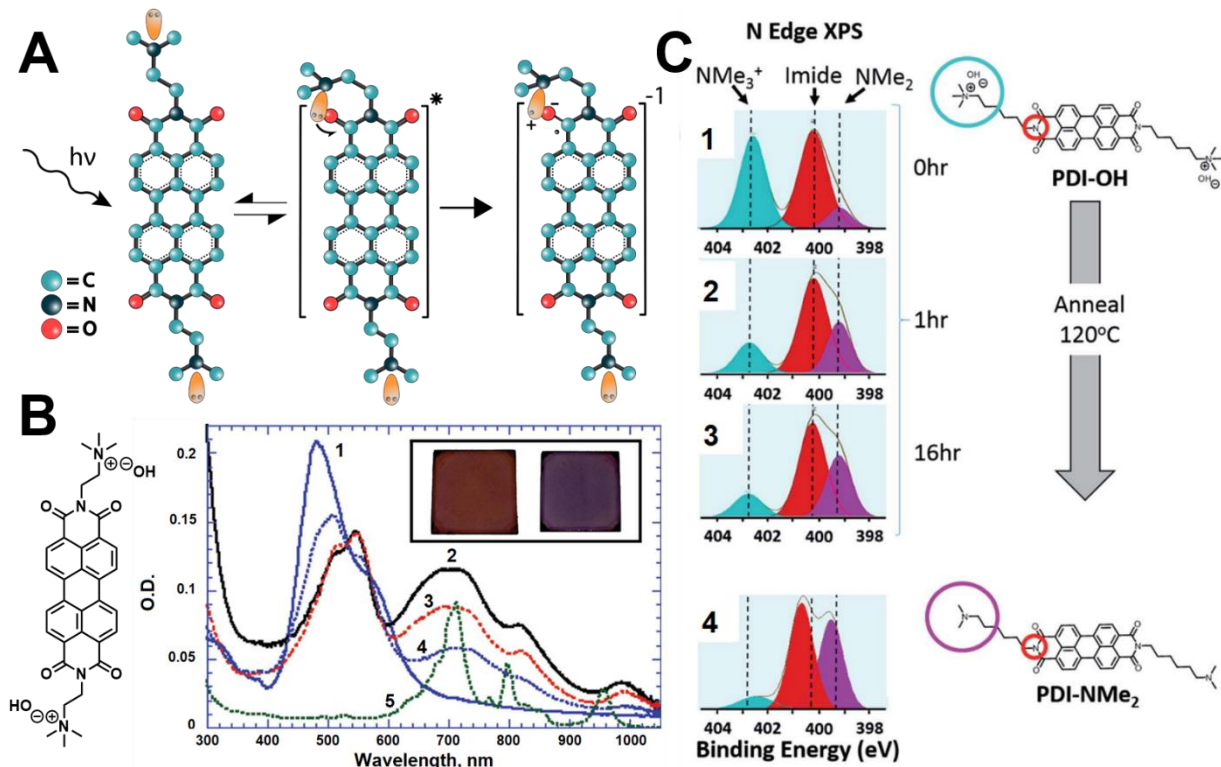

Figure 4. (A) A graphical representation of the self-n-doping mechanism. **(B)** Chemical structures of the compound analyzed in the accompanying absorption spectrum. The numbered spectra correspond to the absorption of the (1) as cast; (2) after heating at 120°C for 20 min in air; (3) 10 minutes after exposure to ~33% humidity air; (4) 1 day in ambient air; (5) electrochemically generated radical anion in THF. Inset: as-cast film (left) and heated film (right). Adapted with permission from ref 56. Copyright 2012 John Wiley & Sons Inc. **(C)** N 1s XPS spectra of an N-PDI (PDI-OH) before (1) and after heating at 120°C for 1hr (2) and 16hr (3), as well as the N 1s XPS spectrum of the (PDI-NMe₂) for reference (4). The relative peak ratios of NMe_3^+, imide, and NMe_2 are shown in blue, red, and purple, respectively. Adapted with permission from ref 128. Copyright 2012 John Wiley & Sons Inc.

It remains unclear exactly how a thermally activated doping mechanism would proceed. Russ et al. estimated the free energy change for charge transfer ΔG_{CT} from an amine donor to a neutral PDI acceptor to be ~+1.4 eV in the solid-state, which is a barrier that far exceeds the ~25-40 meV thermal excitation present when annealing samples, leading them to propose a doping mechanism involving sample decomposition. To support this, they monitored the stability of an ammonium salt with X-ray photoelectron spectroscopy (XPS) of the nitrogen 1s region, whose structure and spectra are shown in **Figure 4C**. Four peaks for the N 1s are observed for the as-cast film, assigned to the quaternary (blue) and tertiary (purple) nitrogen, as well as the imide (red) nitrogen. Upon heating to 120 ºC, the quaternary ammonium fraction diminishes as the tertiary amine fraction increases, while the internal control imide nitrogen fraction remains unchanged, implicating a decomposition process. Mass spectrometry revealed a loss of 15 mass units, consistent with the loss of a methyl group, and Fourier transform infrared spectroscopy revealed the loss of the broad OH stretching mode centered at ~3400 cm^{-1} consistent with water loss. At the same time, electron paramagnetic resonance (EPR) showed an increase in spin concentration with annealing, consistent with electronic doping. As such, they found that the quaternary ammonium deaminates to the tertiary amine with increasing annealing time. However, the authors noted this transformation was not observed for samples with other counterions, and appeared to be unique to the ammonium when paired with a hydroxide counterion.[128] In testing a series of N-PDIs, we have similarly identified numerous examples of dopants that both do and do not degrade yet still show a marked increase in electronic doping even when degradation is not present. Chemical structures for a selection of these compounds are shown in **Figure 5A**. Absorption spectra for these compounds collected before and after thermal annealing at 120 °C under and inert atmosphere are

shown in **Figure 5B**, which shows the conversion of the ground state species (415-570 nm) to the anion radical (570-1100 nm) following annealing. Doping occurs for all compounds in this series following thermal annealing is most pronounced in B6OH and D6OH. XPS spectra of the nitrogen edge collected before and after annealing are shown in **Figure 5C**. Both A6OH and B6OH show signs of amine degradation, but C6OH and D6OH are stable. Matsunaga et al. similarly found examples of structurally stable self-n-doping naphthalene diimides following photoactivation.[124] Degradation is thus an intrinsic property to the structural motif of the dopant in question, with certain structures being more prone to dealkylation. Instead, the increase in doping observed upon annealing is related to the residual presence of water. Absorption spectra of A2I measured in both DMF and water are shown in **Figure 5D**. In water, the PDIs form H-aggregates and all remain in their neutral state. In DMF, monomers are present and radical anions easily form, as evidenced by the characteristic radical peak at 700 nm. Wang et al. similarly observed solvent selection during thin film processing affected radical anion formation. Methanol residue completely suppressed radical anion formation, while methanol/water mixtures favored radical anion formation following annealing.[129] Additionally, thermal activation may reduce the energy gap between the HOMO and HOMO-1, shown in **Figure 5E** to promote photoinduced electron transfer. However, more work is needed to test this hypothesis.
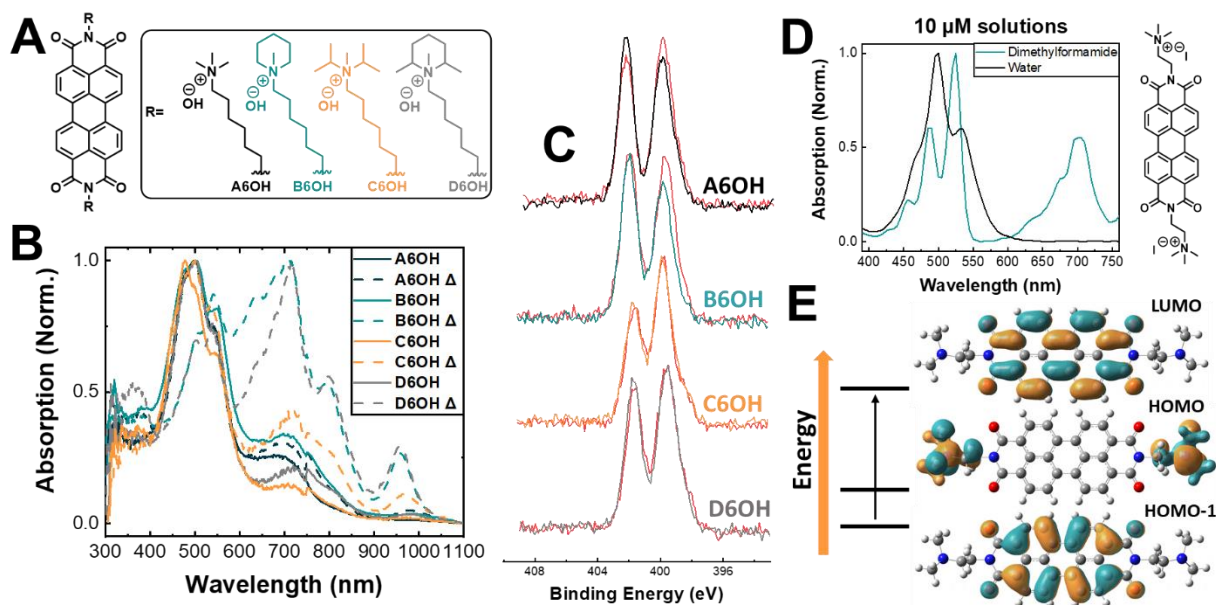
Figure 5. (A) Chemical structures of A6OH, B6OH, C6OH, and D6OH. **(B)** Absorption spectra of thin films of each compound presented in A before and after thermal annealing at 120°C for 1 hr in an inert atmosphere (annealed films are designated with a Δ symbol). **(C)** XPS spectra of the N 1s region of each compound before and after thermal annealing for 1 hr in an inert atmosphere. Annealed samples are shown in red. **(D)** Absorption spectra of 10 µM solutions of A2I (structure shown) in DMF and water. **(E)** HOMO and LUMO gaussian simulations of N,N'-Bis[2-(dimethylamino)ethyl]3,4,9,10-perylenetetracarboxylic diimide computed at the DFT level using the B3LYP functional and a 6-311G** basis set, and accompanying transition energy diagram.

3.2 Structure-function relationships

A number of structure-function relationships have been identified in N-PDIs. Perhaps the most dramatic effects come from the location of the dopants. Dopants can be bound directly to the PDI scaffold through covalent modification of two primary locations; namely the imides and the aromatic bay carbons. The choice of attachment mode affects the self-n-doping process in differing ways. This is because a transverse node along the HOMO and LUMO orbitals of the PDI core, as shown in Figure 2C, electrically isolates the dopants when they are attached to the imides. Here, the HOMO is localized to the dopant, and the HOMO-1→LUMO transition is equivalent to the HOMO→LUMO transition in un-doped PDIs. The arrangement of orbital energies shown here makes electron transfer ideal from the dopant to PDI following photoexcitation. The perylene core itself is an acceptor-donor-acceptor (A-D-A) system, and functionalization of the imides creates an electrically isolated D-A-D-A-D system. Doping, therefore, depends on the arrangements of the dopants relative to the core. Free rotation of the alkyl linkers is important for the donor to come into close proximity with the dicarboxylic acid imide acceptor and initiate electron transfer. Their electrical isolation also means the redox properties of the core are generally unaffected when dopants are attached to the imide nitrogens.

Photogenerated radical anions also form in N-PDIs functionalized at the core.[130–132] Zhao and Wasielewski investigated the redox properties of various core functionalized N-PDIs, as shown in **Figure 6A** accompanied by their relative redox potentials. The addition of dopants resulted in a relatively modest negative shift in reduction potential by 0.3 V, compared to a pronounced negative shift in the oxidation potential up to 1.2 V vs SCE. This dramatic shift in oxidation potential equates to a raised HOMO relative to vacuum and smaller bandgap, opening

an interesting avenue to energy level alignment tailoring for device applications.[133] This notion is further supported by computational work by Langhals and Blanke showing core functionalization dramatically raises the HOMO level relative to vacuum and subsequently lowers the barrier to self-doping.[134] The ability to modulate the HOMO is directly a result of the nodal pattern of the core which causes moieties attached to the bay positions to be in direct electrical contact with these orbitals in a manner similar to that of push-pull systems.[135]

Ahrens et al. studied the dramatic bathochromic shifting that he and others have observed in the optical spectra of core-substituted N-PDIs. Compounds B1 and B2 shown in **Figure 6B** are highly soluble in several solvents up to ~1 mM, thus monomer absorption spectra were measured. Absorption spectra of B1 and B2 are shown in **Figure 6C**, which are strongly red-shifted compared to imide substituted N-PDIs with a broad absorption band from 550-750 nm for B1 and 475-750 nm for B2. The fluorescence of B1 and B2 are also strongly quenched for both compounds due to the presence of radicals which were measured with EPR. Thus, the core functionalized PDIs also undergo an intramolecular doping mechanism, but one that does not depend on chain rotation. The electrical connection of the amino functional groups to the perylene core permits strong doping of PDI monomers. The group also performed electron nuclear double resonance (ENDOR) and EPR spectroscopies on B1 and B2 after treatment with oxidative $NOSbF_6$ to form the radical cation. This was done to probe the electron density distribution and nature of the electron donating species. Total spin density maps for these compounds are shown in **Figure 6D**. The largest hyperfine coupling constants that they measured were those of the amino protons and amino nitrogen atoms, demonstrating that the amine forms a cation radical during charge transfer to the perylene core. They also found that the radical cationic amines were remarkably stable, with 50-80% of the signal intensity decreasing after sitting in air for a week for B1 and B2, respectively.[136]
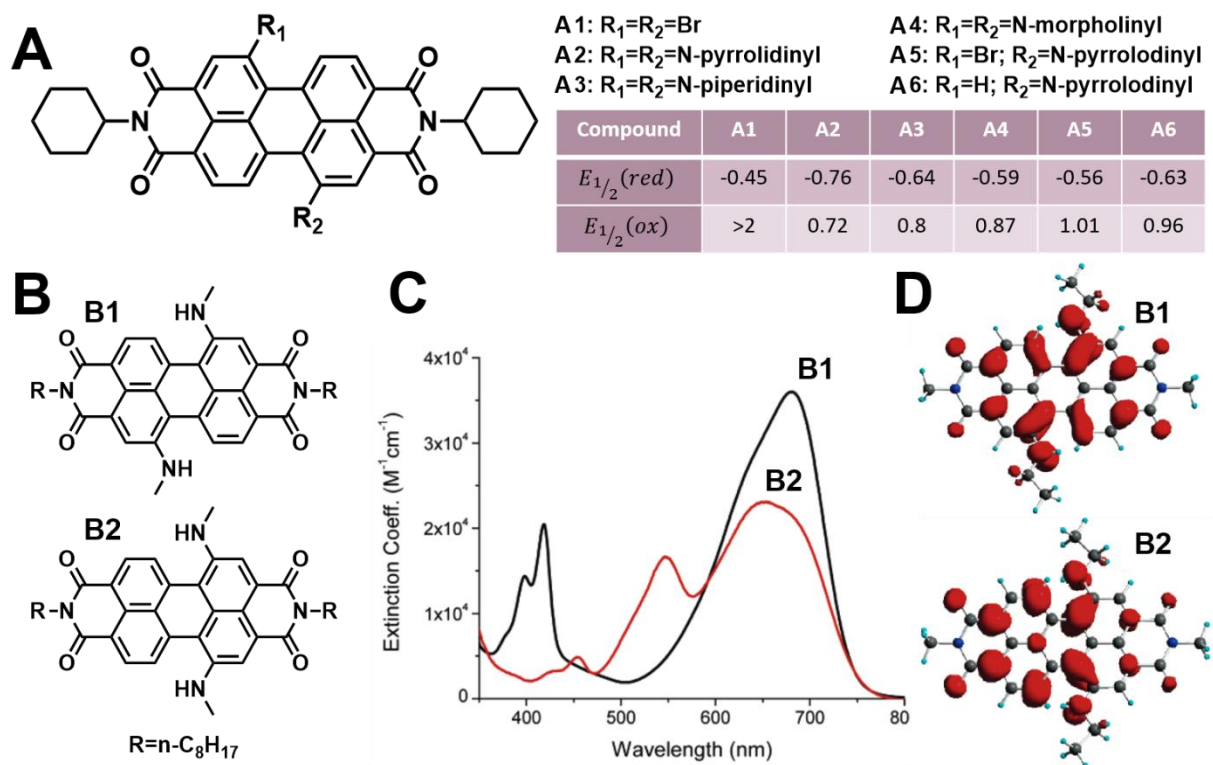
A1: $R_1 = R_2 = Br$
A2: $R_1 = R_2 = $ N-pyrrolidinyl
A3: $R_1 = R_2 = $ N-piperidinyl
A4: $R_1 = R_2 = $ N-morpholinyl
A5: $R_1 = Br$; $R_2 = $ N-pyrrolodinyl
A6: $R_1 = H$; $R_2 = $ N-pyrrolodinyl

Compound	A1	A2	A3	A4	A5	A6
$E_{1/2}(red)$	-0.45	-0.76	-0.64	-0.59	-0.56	-0.63
$E_{1/2}(ox)$	>2	0.72	0.8	0.87	1.01	0.96

$R = n\text{-}C_8H_{17}$

Figure 6. (A) Chemical structures of compounds A1-A6 and a table of redox potentials for each. **(B)** Structures of compounds B1 and B2. **(C)** Absorption spectra of B1 and B2. **(D)** Total spin density maps or geometry optimized B1 and B2. Reprinted with permission from ref. 136. Copyright 2006 American Chemical Society.

Direct comparisons between core and imide functionalization were performed by Wu et al. who compared the photoinduced electron transfer of two PDIs functionalized at the imide position with that of one functionalized at the core (**Figure 7**) using steady-state absorption and fluorescence spectroscopy in various polar organic solvents and two room-temperature ionic liquids (RTIL).[137] Absorption and emission properties are given in **Table 1**, where ε is the molar extinction coefficient, λ_a is the wavelength of the 0-0 absorption, λ_f is the wavelength of the 0-0

emission, and Φ_f is the fluorescence quantum yield. The absorption spectra of compounds C1 and C2 in all solvents exhibited absorption spectra characteristic of neutral monomers in solution. The absorption maximum of the 0-0 transition red-shifted up to 8 nm for C1 and 6 nm for C2 depending on the solvent environment. The absorption spectrum of compound C3 was similar to that of B1 and B2, with a broad absorption band from 550-750 nm and exhibited the largest red shift up to 27 nm in different solvent environments. The authors attributed the red shifting to solvent stabilization of the polarized charge transfer states, which would be greatest in systems forming stable radical anions. The fluorescence quantum yields varied substantially for C1 and C2 while C3 remained fairly low in all solvents, ranging from 0.40% in RTIL A to 2.56% in toluene. The fluorescence was strongly quenched in the organic solvents, with C1 and C2 respectively exhibiting quantum yields of 1.60-5.90% and 1.97-5.36%. Surprisingly, the respective quantum yields for C1 in RTIL A/B were 98.35% and 46.47% and for C2 84.42% and 42.76%. The strong fluorescence quenching that Wu and coworkers observed is due to the presence of radicals, and demonstrates that solvent polarity can play a strong role in the self-doping process for PDIs. Additionally, since the structures of C1 and C2 only differ by a single CH_2 tether between the donor and acceptor, the differences in quantum yields between these two species can be attributed to improved spatial conformation between the longer donor tertiary amine and acceptor core, which is consistent with similar intramolecular donor-acceptor systems.[87,138,139] This concept is further supported by fluorescence spectroscopy studies of PDIs substituted at both the core and imide positions with tertiary amines. The fluorescence quantum yields decrease much more dramatically with core substitution than imide substitution due to the non-emissive nature of CT states.[140,141]
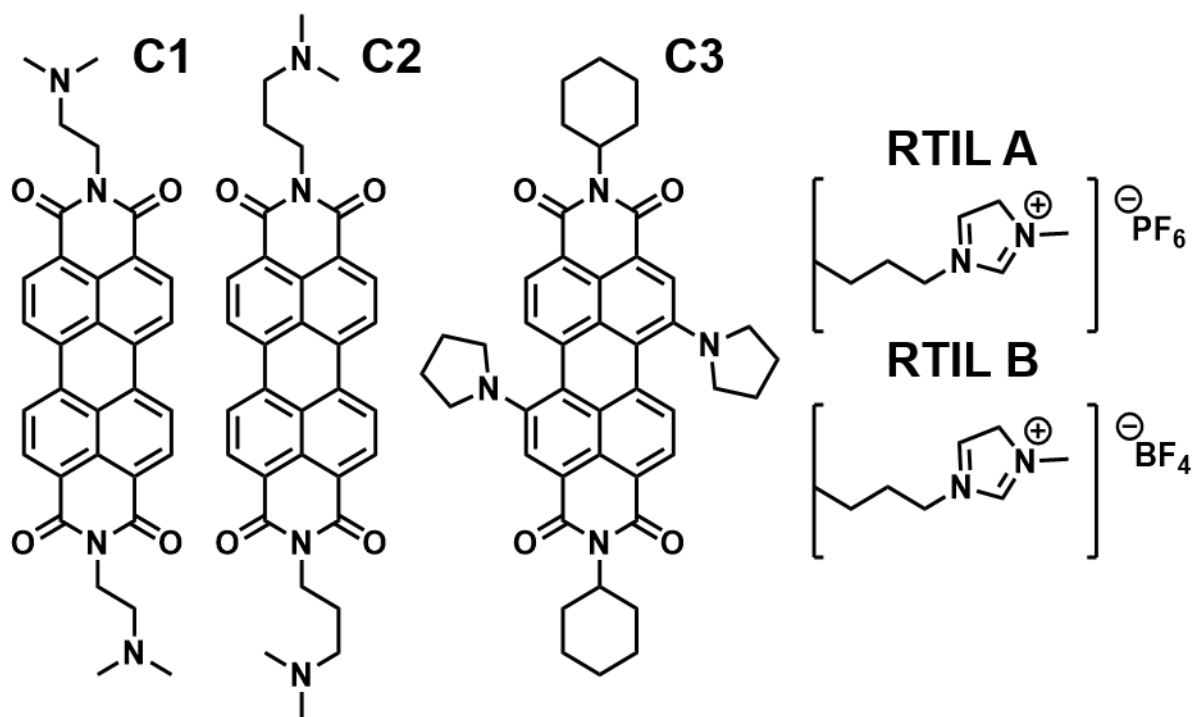
Figure 7. Chemical structures of C1-C3 as well as the structures of room temperature ionic liquids (RTIL) A and B.

Table 1. Absorption and emission spectral parameters of C1-C3 in various solvents.

Compounds		RTIL A	RTIL B	DMF	THF	CH$_2$Cl$_2$	toluene
C1	$\varepsilon \times 10^4 \ (mol^{-1}L\ cm^{-1})$	8.77	8.73	8.74	8.20	8.70	8.33
	$\lambda_a(nm)$	524	527	524	518	520	526
	$\lambda_f(nm)$	539	543	539	534	536	541
	$\Phi_f(\%)$	98.35	46.47	1.60	2.15	2.26	5.90
C2	$\varepsilon \times 10^4 \ (mol^{-1}L\ cm^{-1})$	8.46	8.26	8.62	8.65	8.54	8.66
	$\lambda_a(nm)$	524	526	524	520	523	526
	$\lambda_f(nm)$	540	542	540	533	537	540
	$\Phi_f(\%)$	84.42	42.76	1.97	2.54	3.16	5.36
C3	$\varepsilon \times 10^4 \ (mol^{-1}L\ cm^{-1})$	4.64	4.70	4.49	4.73	5.02	4.80
	$\lambda_a(nm)$	712	713	701	685	699	686
	$\lambda_f(nm)$	754	756	748	723	734	717
	$\Phi_f(\%)$	0.40	0.33	0.62	1.63	1.60	2.56

Wang et al. compared differences between tertiary amine and quaternary ammonium self-dopants both with and without functionalization of the PDI core with electron withdrawing and donating substituents. The structures for these compounds are shown in **Figure 8A**. The general naming scheme is based on substituents added to the PDI core (R) and the substituents added to the imide positions (X) in the manner of P'R'F-'X'. For the range of core substituents in this study, R=H for hydrogen, R=C for chlorine, and R=O for o-methoxy-phenyl. In the case of the imide substituents, X=N for the tertiary amine, X=Cl for the ammonium chloride, X=OH for the

ammonium hydroxide, X=BIm$_4$ for the ammonium tetrakis(1-imidazolyl)borate, and X=F for the ammonium fluoride functional group. The addition of electron-withdrawing chloro substituents changes the HOMO and LUMO energies in a manner opposite to that of the electron donating o-methoxy-phenyl groups as shown in **Figure 8B**, and were confirmed by cyclic voltammetry to have a ~0.2 eV gradient. The authors compared the impact of these structural and phase-dependent changes on the self-doping process via absorption spectroscopy studies. The absorption spectra of the samples in methanol are shown in **Figure 9A-C**. The set of neutral S_0-S_1 peaks is slightly red-shifted between the PHF-X, PCF-X, and POF-X samples due to small changes in the HOMO energy by core substituent addition. Interestingly, all of the chloro-substituted samples show electronic doping in the ~600-1100 nm region with the exception of PCF-Cl. As thin films, the PHF-X samples exhibit relatively low doping density, while doping is not observed at all in the POF-X samples (**Figure 9D-F**), and is greatest in the PCF-X samples. Thermal annealing also enhances doping density in these samples, and was necessary for the PHF-X samples to show an appreciable degree of doping (**Figure 9G-I**). The samples most sensitive to annealing were PCF-F and PCF-BIm$_4$ upon thermal annealing, though the absorption intensities increased for all PCF-X samples. These findings implicate interesting ways of modifying self-dopant efficiency through core functionalization, as well as the ability of counterions to affect the formation of radical anions.[129]
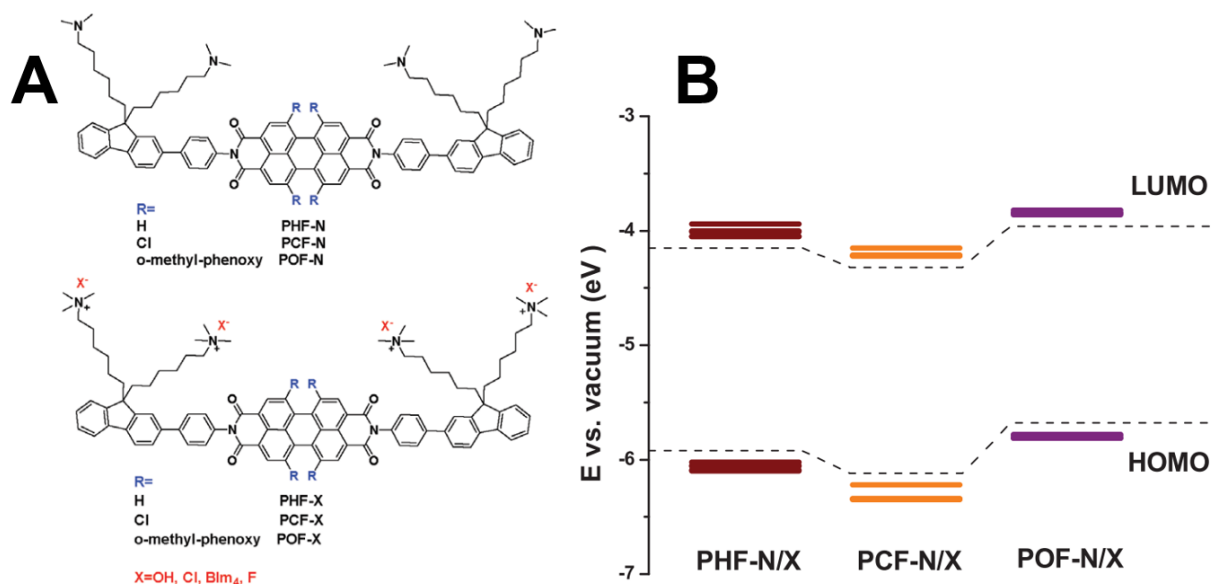
Figure 8. (A) Chemical structures of P'R'F-'X' derivatives, where R corresponds to bay functionalization with hydrogen, chlorine, or o-methyl-phenoxy, and X corresponds to the anionic counterion in quaternary ammonium structures, where OH is hydroxyl, Cl chloride, BIm_4 is tetrakis(1-imidazolyl)borate, and F is fluoride. **(B)** Relative changes to the HOMO/LUMO levels when the PDI core is functionalized with hydrogen, chlorine, or o-methyl-phenoxy in PHF-X, PCF-X, and POF-X, respectively. Reprinted with permission from ref 129. Copyright 2017 John Wiley & Sons Inc.
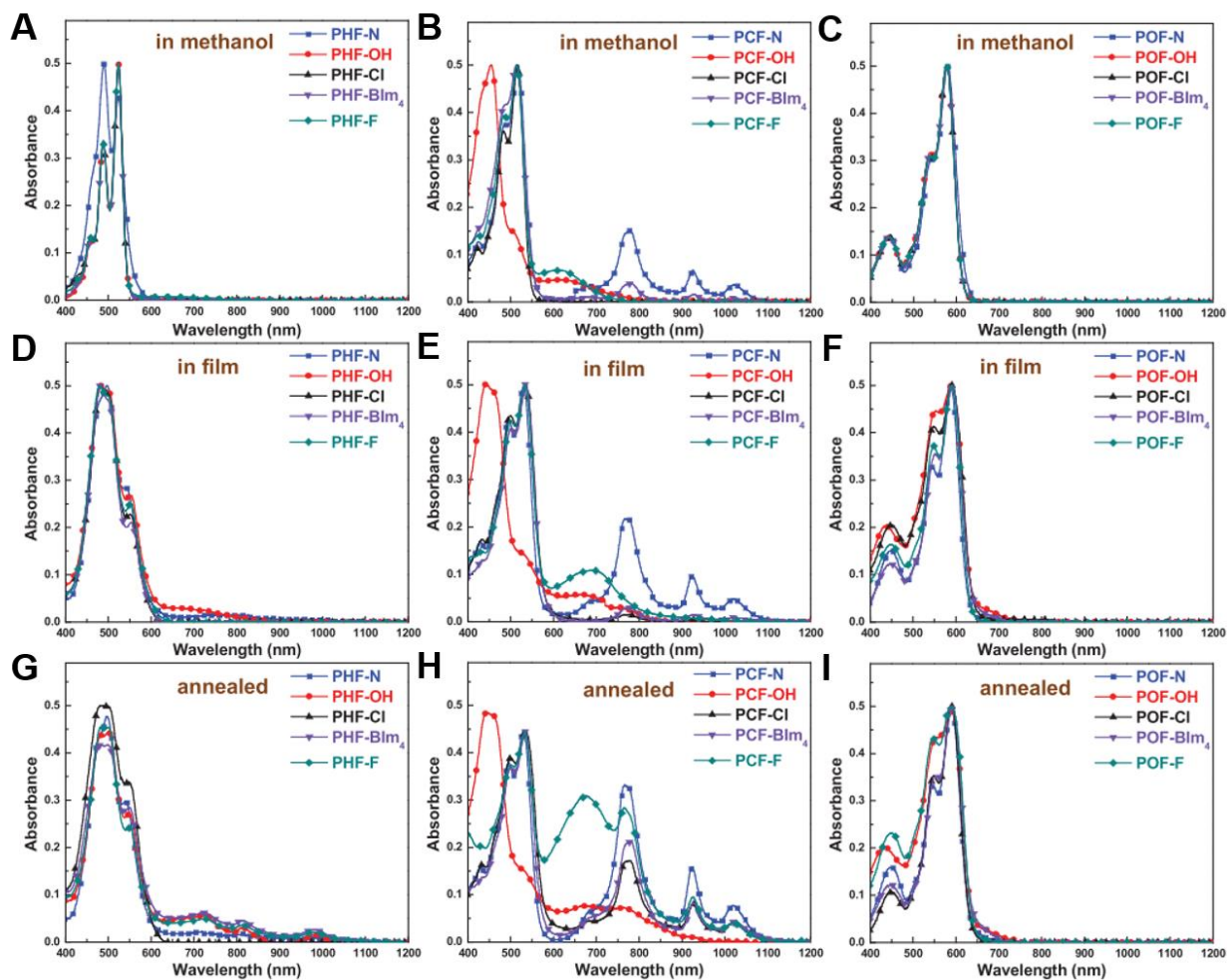
Figure 9. Absorption spectra of P'R'F-'X' derivatives **(A-C)** in methanol, **(D-F)** as cast in thin films, and **(G-I)** after annealing at 85°C for 20 min. Reprinted with permission from ref 129. Copyright 2017 John Wiley & Sons Inc.

Our own work has attempted to address dopant design principles in N-PDIs, which had been previously lacking.[142] We investigated the effect of steric encumbrance on the performance of tertiary amino dopants whose structures are shown in **Figure 10**. Here, the dopants were attached to PDI at the imides with a two-carbon tether. Quantitative EPR measurements of these

samples showed that more steric encumbrance decreases the efficiency of dopants in tertiary amines due to the obstruction of the lone pair donating ability centered on the nitrogen, as shown in **Figure 10A**. Interestingly, the more encumbered dopants also show greater air stability, which we hypothesize is a result of protection of the carriers from oxygen by the bulky groups. The opposite trend was observed in samples doped with quaternary ammonium moieties, whose structures are shown in **Figure 10B**. Here, the structures vary by tether length (two and six-carbon tethers), counterion (iodide and hydroxide), and steric profile. Quantitative EPR of these samples reveals that steric encumbrance increases doping efficiency, as shown in **Figure 10B**. We rationalize this opposing trend by noting that the inclusion of steric bulk weakens the interaction of the anion with cationic nitrogen, which leads to an overall increase in Lewis basicity of the anion thereby improving doping efficiency.
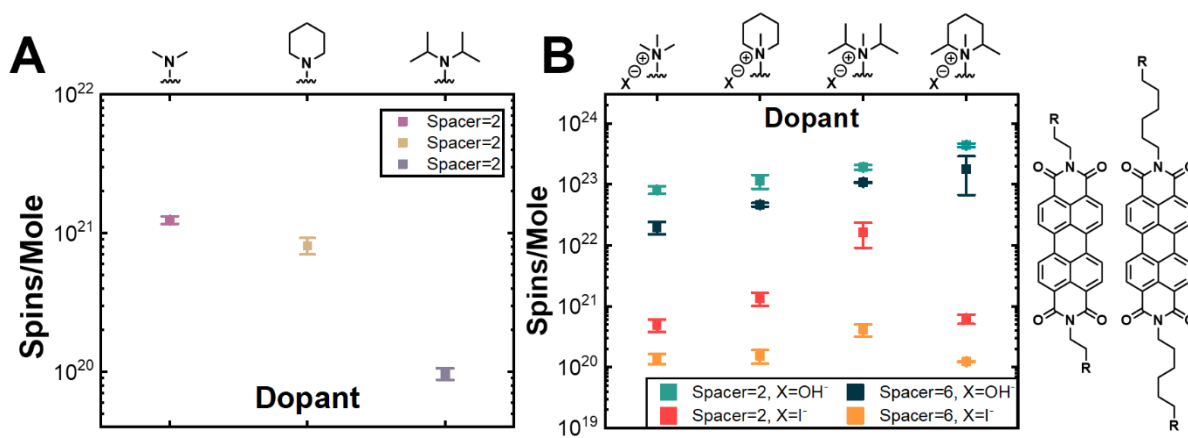

Figure 10. (A) Quantitative EPR measurements of spin concentration in tertiary amino doped N-PDIs with increasing steric encumbrance. **(B)** Quantitative EPR of sterically encumbered ammonium doped N-PDIs. The groups vary by steric encumbrance, tether length, and counterion.

Steric encumbrance also plays an important role in solution. N-PDIs with two carbon tethers were diluted to 10-60 µM in dimethyl formamide in the dark, sealed in anaerobic cuvettes under an inert atmosphere, and their absorption spectra were measured. Absorption spectra for the two N-PDIs with the least steric encumbrance and an iodide counterion are shown in **Figure 11A** and hydroxide counterion in **Figure 11B**. In the iodide sample, all PDIs are in the neutral state, whereas the hydroxide sample exhibit a high degree of electronic doping, to the point that all of the neutral species has been converted to either the radical anion (~600-1000 nm) or the dianion (~500-600 nm). Thus, the hydroxide is a much stronger dopant than iodide, which generally follows Lewis basicity trends. Samples were then irradiated with a 405 nm lamp for 90 minutes and measured once again. **Figure 11C-D** show the increase in radical anion concentration upon photoirradiation. The percentage difference between the integrated intensity of the neutral and radical anion spectra for the iodide samples measured in the dark and after irradiation were calculated and plotted in **Figure 11E**. It can be seen from this plot that radical anion formation is most efficient in the low concentration regime. As the concentration increases, the dopants are less free to tumble in solution, and chain rotation is inhibited, leading to a decrease in radical formation. Interestingly, the opposite trend was found for dianion formation. As shown in **Figure 11F**, dianions form much more readily in the high concentration regime than at lower concentrations. Additionally, dianions do not form at all in systems with more sterically encumbered dopants. The dopant with the lowest degree of steric encumbrance had the highest concentration of dianions. We hypothesize that dianions favor these conditions due to Coulombic stabilization of the charge between adjacent chromophores in a manner similar to that of exciton stabilization in PDI aggregates. In this case, dianions would favor higher concentrations. Additionally, bulky dopants would inhibit interactions between neighboring chromophores and impair charge delocalization.
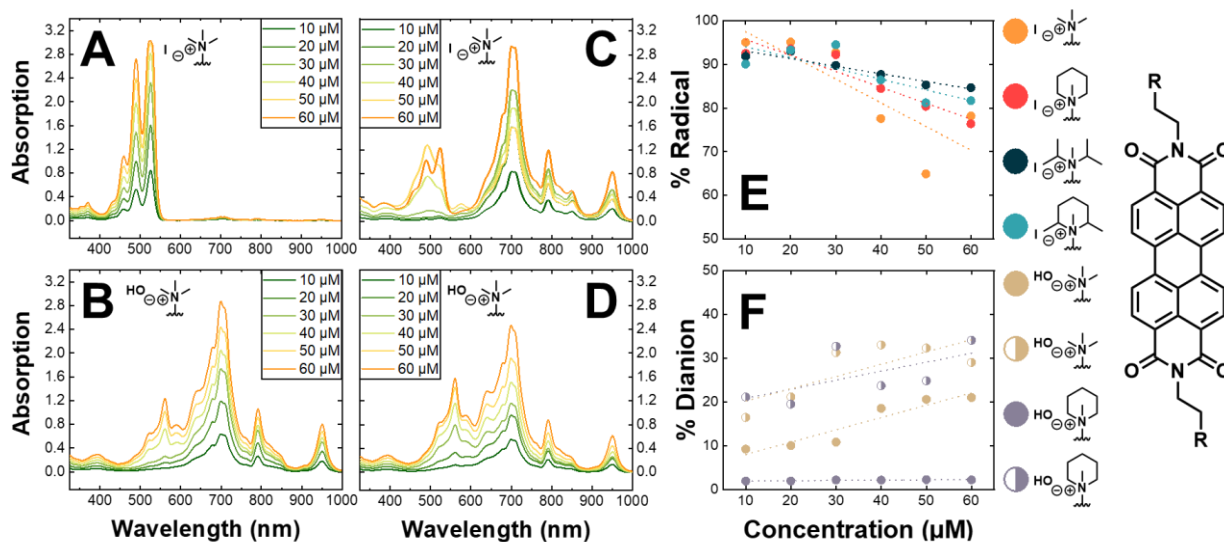
Figure 11. (A-B) Absorption spectra of N-PDIs (structures in insets) measured in the dark at 10-60 µM in sealed anaerobic cuvettes. **(C-D)** The same samples in A-B after 90 minutes of irradiation with a 405 nm lamp. Samples remained sealed in the cuvettes throughout the experiment. **(E)** Percentage radical anion formation for 4 samples (structures to the right) before and after irradiation at 10-60 µM concentrations. **(F)** Percentage dianion formation before (filled) and after (half-filled) photoirradiation of two N-PDIs (structures to the right).

In view of these principles, one must take into careful consideration a number of parameters. First, the mode of attachment will strongly impact doping efficiency with core attachment being generally favored. However, it remains to be investigated how attachment distance affects doping efficiency in core doped N-PDIs. Additionally, the choice of dopant between amine and ammonium dopant will affect efficiency. In our own systems, we found that ammonium dopants are more effective than amines, but only when paired with strongly Lewis basic counterions. We also observed shorter tethers to be more effective at doping due to the closer

proximity of the dopant to the acceptor, though it should be noted that there are instances of N-PDIs with longer tethers with much higher electrical conductivities.[82] This phenomenon may be morphologically driven, though, and therefore specific to these structures in particular rather than a general working design principle. Finally, the inclusion of steric encumbrance will depend on whether one uses tertiary amines or quaternary ammonium substituents, and whether one is working in solution or the solid-state, as there are trade-offs in each regime.

4. APPLICATIONS

4.1 Biochemistry

Perhaps the most widely investigated application of N-PDIs has been in biological environments. Ionic PDIs are naturally suited to biological applications due to their solubility in aqueous environments. The inclusion of water-soluble ammonium salts, coupled with PDI's innate photophysical properties and controllable self-assembly, has led to a number of interesting uses. Perhaps surprisingly, PDIs functionalized with amines have also been reported in a number of these roles, dispelling the notion that a PDIs must contain an ammonium salt to serve any functional role in these environments.[143–147] N-PDIs are even amenable to the homochiral nature of biological environments. It has been shown that N-PDIs are capable of chiral self-assembly to form various structures such as supramolecular helices, and can further be used as biologically-based chiral sensors.[148–153] For example, the photoluminescence and electroluminescence properties of N-PDI can be tuned in both turn-on and turn-off sensing of various analytes such as nucleic acids, tumor markers, proteins, and drugs.[154–160]

The relationship between N-PDIs and DNA has been the subject of the most widespread investigation due to its role in disease and the emerging interest in using DNA as a molecular wire,

data storage, and other electronics applications.[161–167] Manipulations of the DNA scaffold have long been a core component within the biochemistry field, leading to an exciting crossover between biological and semiconductor sciences. For example, work by T. Takada et al. has demonstrated that PDI coordinates within hydrophobic abasic cavities created within DNA strands, as shown in **Figure 12A-B**.[48] When base pairs are removed from DNA strands containing a deoxyribose (dS_n) spacer, a corresponding number of cPDI chromophores (P[n]) coordinate in the formed pocket through hydrophobic interactions. By spacing apart the hydrophobic pockets (**Figure 12C**), the authors were able to observe evidence of excitonic coupling between the chromophores using absorption spectroscopy. **Figure 12D** shows the changes between the 0-0 and 0-1 peak ratios when the hydrophobic pocket sizes were increased (dS_n 1→5), as well as when the spacing between dS_2 hydrophobic pockets was increased. H-type co-facial stacking was observed as more PDI chromophores aggregated within the increasingly larger dS_n cavities, while excitonic coupling between chromophore dimers sandwiched in dS_2 pockets resulted in a decrease of the absorbance intensity ratio A_{0-0}/A_{0-1}.[168]
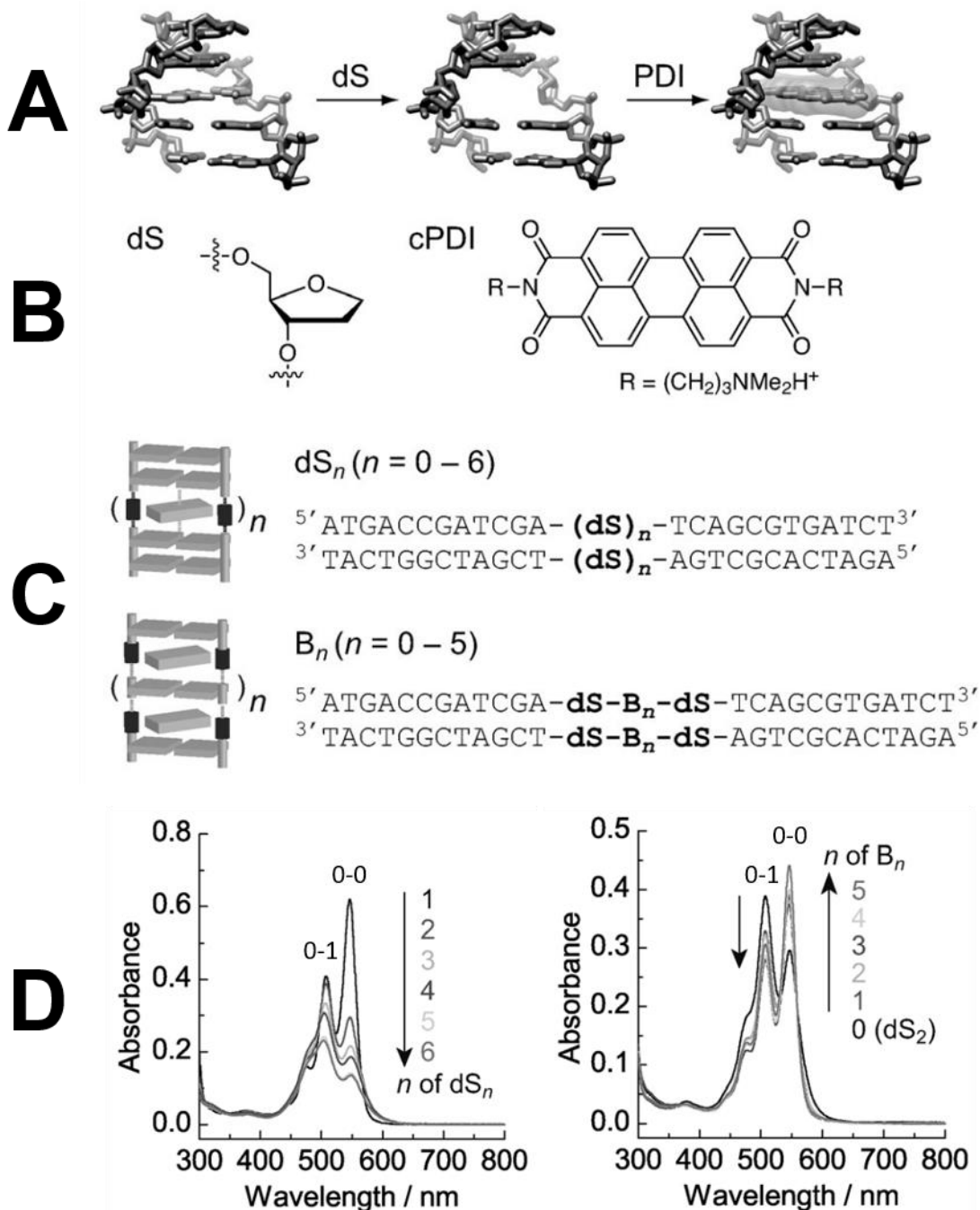
Figure 12. (A) Representation of PDI coordinating to a hydrophobic pocket created within a DNA strand by replacing nucleosides with abasic analogues. **(B)** Structure of the abasic deoxyribose spacer (dS) and cPDI. **(C)** DNA sequences with different binding cavity configurations; the first with dS_n abasic sites and the second with B_n cavity spacers composed of alternating A-T pairs

between two dS sites. **(D)** Absorption spectra of dS_n and B_n DNA configurations. Reprinted with permission from ref 168. Copyright 2012 John Wiley & Sons Inc.

Takada and coworkers have also investigated the photoconductivity of both sets of one-dimensional P(n) nanoarrays. The interested reader is directed to an investigation of the photoconductivity and charge separation dynamics of the dS_2 systems.[169] As shown in **Figure 13A**, PDI—DNA arrays are anchored to gold electrodes and their photoconductivity responses are measured with a 540 nm excitation source. All complexes exhibit sharp on-off photocurrent responses (**Figure 13B**) that increase by 4x (P2) and 8x (P3) upon subsequent addition of a single chromophore into the array; this despite virtually equivalent oscillator strengths of the 540 nm excitation for P1, P2, and P3. **Figure 13C** displays the photocurrent action spectrum overlaid on the absorption spectrum of each complex. The photocurrent response at each excitation wavelength follows the absorption spectral features of the chromophores, indicating that the photocurrent response originates as a direct result of the PDI aggregate conformations. To explain the underlying mechanism, femtosecond time-resolved transient absorption measurements were carried out on the complex series. Ground state bleaching in **Figure 14A-C** is observed for all complexes at around 540 nm and the formation of a charge separated PDI radical anion at ~720 nm is produced in P1 by charge transfer from the adjacent adenine base to excited PDI, which results in a slight red-shift in the absorption feature. P2 and P3 both exhibit a broadening of this absorption feature ranging from ~575-775 nm, which the authors attribute to delocalization of charge along the PDI chromophores. The decay profiles of the 720 nm excitation in **Figure 14D** have similar constants of 0.8 ns but with broadened biexponential tailing features related to the

greater transient absorption intensities at 720 nm for the series, consistent with the formation of longer-lived charge delocalized states in PDI aggregates.[170]
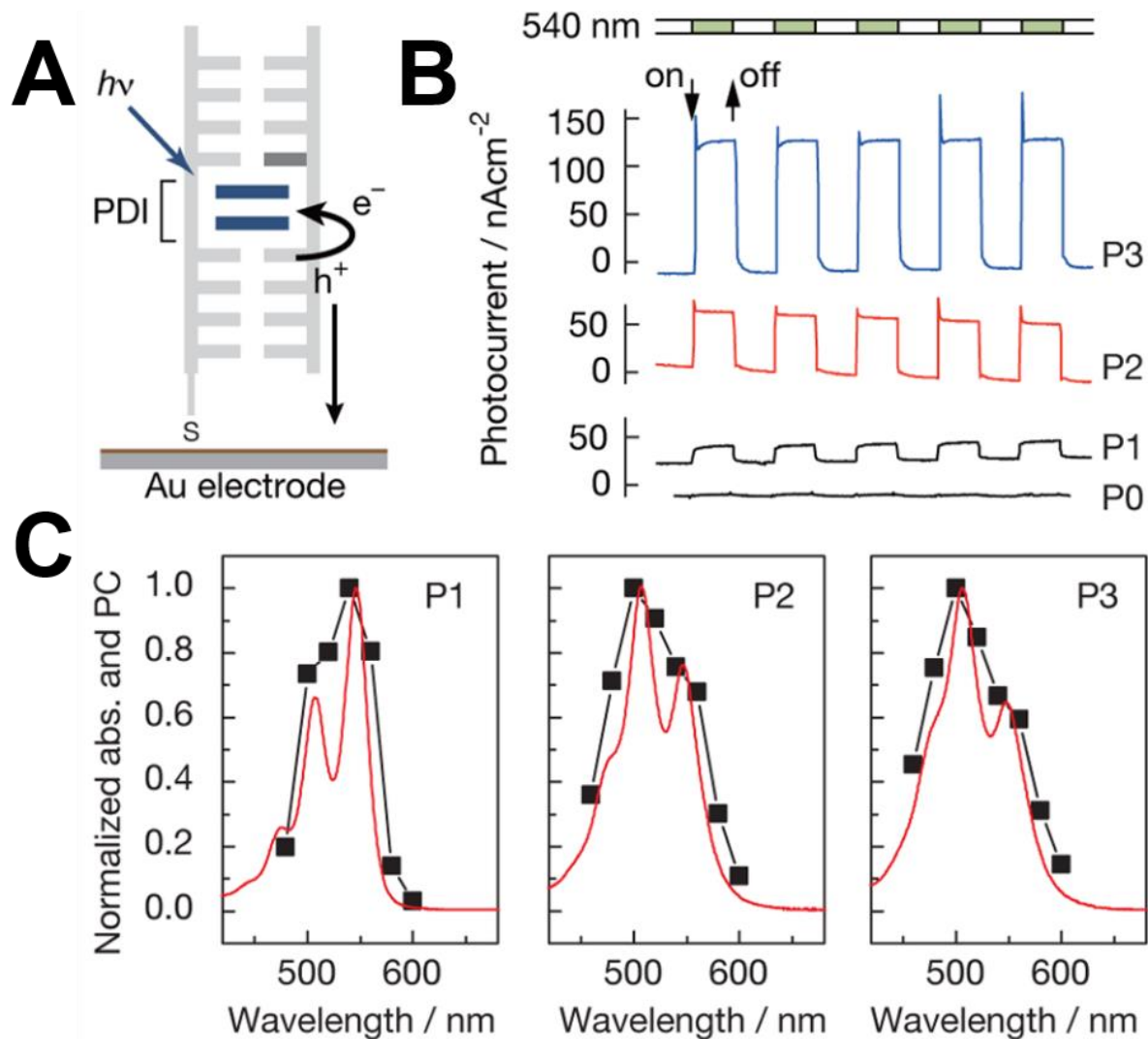

Figure 13. (A) Schematic representation of photocurrent generation in a P2 complex (two cPDI units coordinated in a dS_2 pocket) bound to a gold electrode. **(B)** Photocurrent response to irradiation with a 540 nm excitation source with a 10 s repetition time in P_n complexes. **(C)** Action spectra of P_n complexes, displaying the normalized absorption spectra (red) and photocurrent (black). Reprinted with permission from ref. 170. Copyright 2014 American Chemical Society.
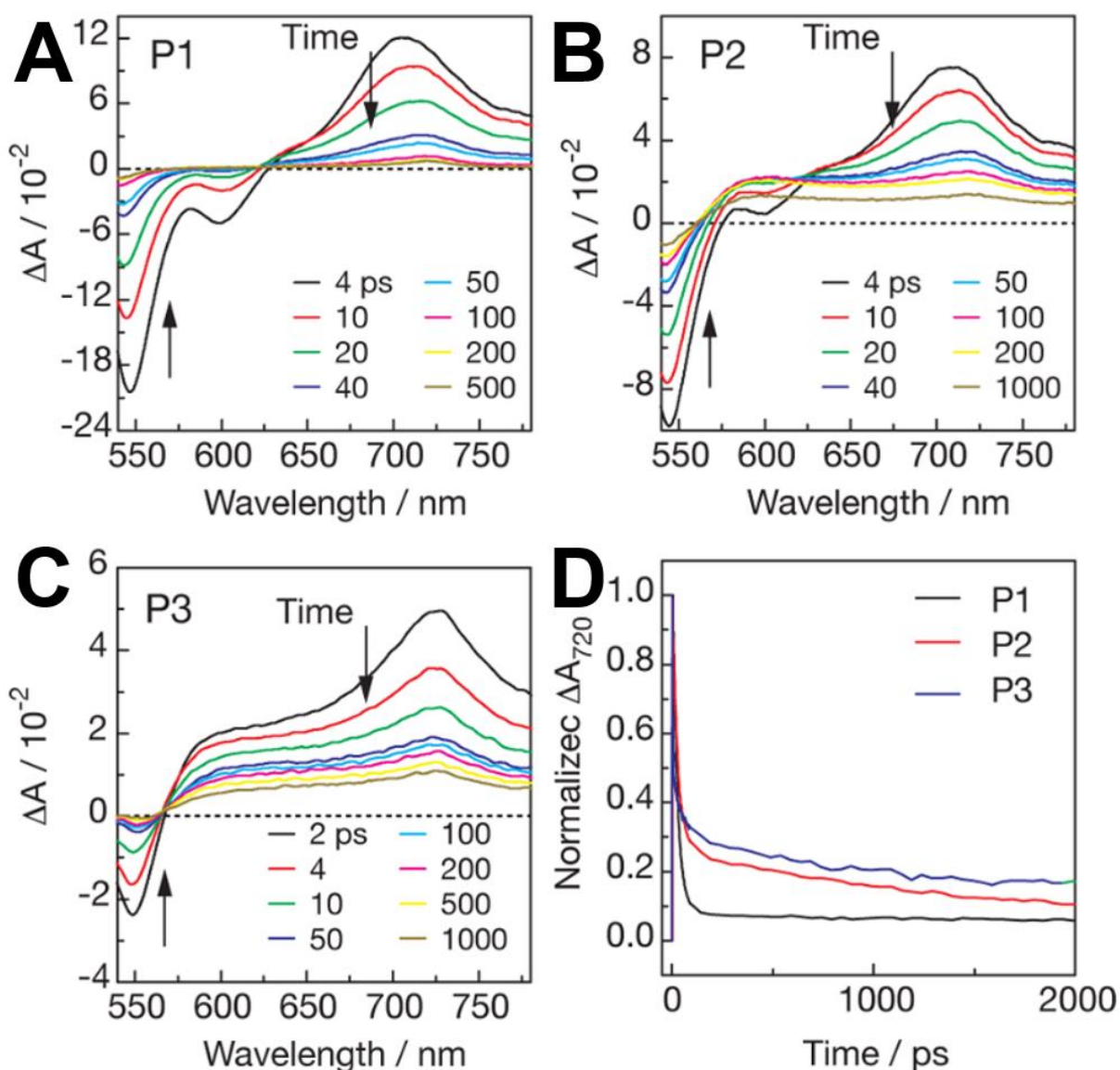
Figure 14. Transient absorption spectra of **(A)** P1, **(B)** P2, and **(C)** P3 in a 20 mM pH=7 sodium buffered solution using a 150 fs 540 nm excitation source. **(D)** Decay time of P_n complexes monitored at 720 nm. Reprinted with permission from ref. 170. Copyright 2014 American Chemical Society.

The role of DNA is central to life and thus plays a critical role in the progression of many diseases, such as cancer. N-PDIs have demonstrated anti-cancer activity through selective

inhibition of telomerase, the protein responsible for the seeming agelessness of cancer cells by lengthening telomere sequences. Indeed, ammonium substituted PDIs have been shown to have excellent cellular uptake.[171] A number of amine and ammonium functionalized PDI derivatives have been found to bind G-quadruplexes, supramolecular structures that form within telomeric and other oncogenic promoter sequences of DNA.[172–174] The binding has also been found to be pH dependent, with monomeric species binding in low pH environments to both DNA duplexes and G-quadruplexes, and selective binding of G-quadruplexes with higher order aggregation at higher pH.[175] Amino/ionic PDIs have been found to act as potent competitive binders to these DNA regions over telomerase, and are highly selective to them over other double or single stranded DNA sequences.[146] Interestingly, some of the most potent PDI inhibitors are those which include multiple dimethylaminoethyl groups added to both the imides and core, such as DAPER4C(1,7), whose structure and binding to a monomeric G-quadruplex obtained by simulated annealing are given in **Figure 15A-B**.[49] Similar work has been extended to other perylene and coronene derivatives.[176] Beyond in vitro telomerase inhibition, Xu et al. observe cytotoxic PDIs substituted with trimethylammonium functional groups inhibit the growth of HeLa and HCT116 cancer cell lines. Their family of PDIs specifically bioaccumulate within animal cell nuclei by intercalation and preferential interaction with DNA. They compared substitutions of up to six ammonium ion species with ionic strength, finding greater DNA intercalation in smaller, more strongly ionic species.[177,178]
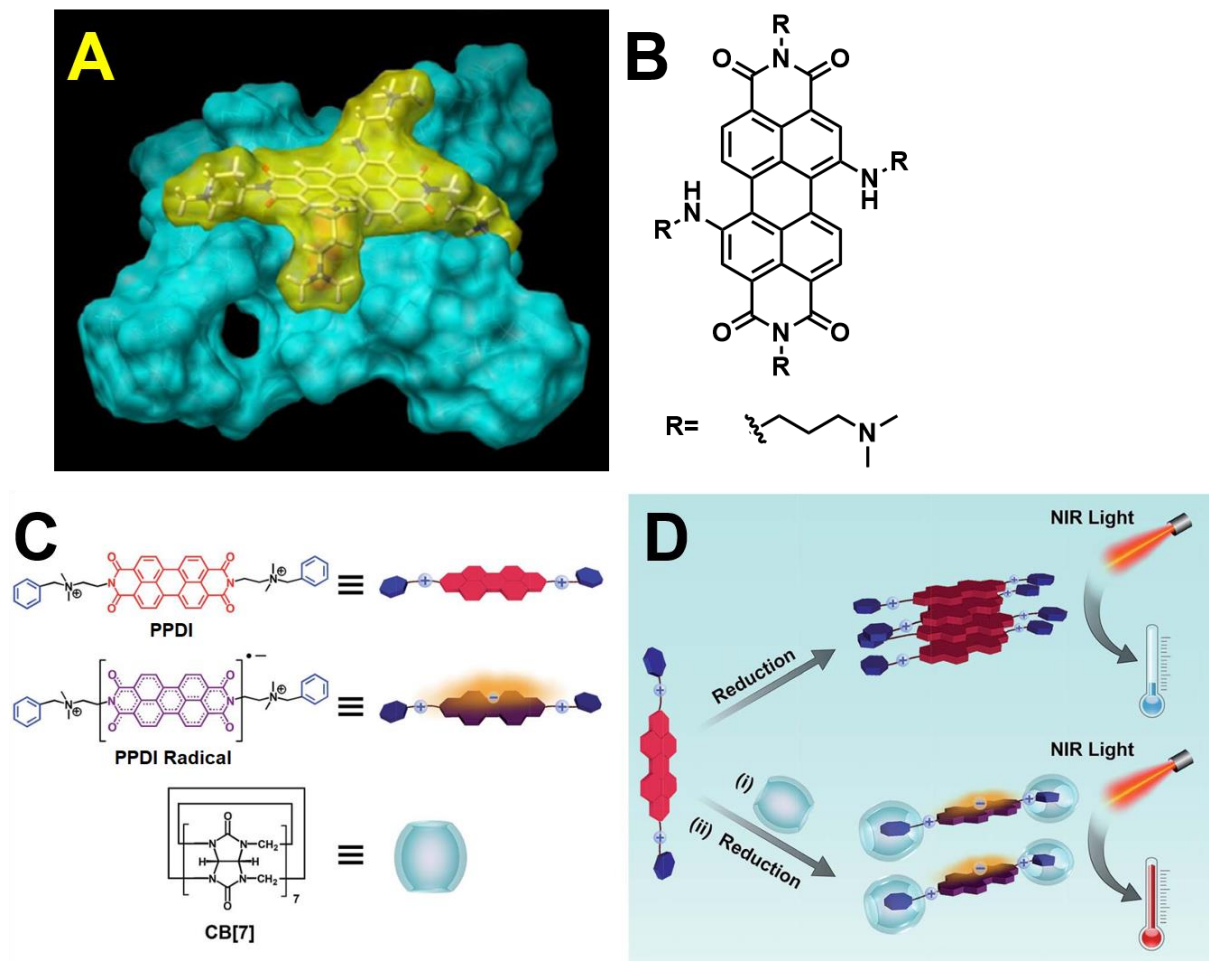
Figure 15. (A) Molecular modeling simulation of DAPER4C(1,7), shown in **(B)** and depicted in yellow, bound to a monomeric G-quadruplex shown in blue. Adapted with permission from ref. 49. Copyright 2007 Elsevier. **(C)** Structures and schematic depictions of PPDI, PPDI radical anion, and CB[7]. **(D)** BPDI radical anions generated by reduction with sodium dithionate yielding low NIR photothermal conversion efficiency (top); formation of a BPDI/(CB[7])$_2$ supramolecular complex between, which was reduced with sodium dithionate yielding improved NIR photothermal conversion efficiency (bottom). Reprinted with permission from ref 179. Copyright 2015 John Wiley & Sons Inc.

DNA is central to cellular proliferation in bacterial infection. In compelling work, Jiao et al. found selective antibacterial action of a supramolecular N-PDI related complex. Shown in **Figure 15C**, PPDI is complexed with two equivalents of the cucurbit[7]uril macrocycle (CB[7]) which encapsulate the phenyl end-groups creating barbell-like structures with a binding constant of 2.9 x 10^{12} M^{-2}, which is attributed to the interaction of CB[7] with both the phenyl and ammonium groups of the side chains. The complex effectively decreases aggregation of PPDI, as indicated by the oscillator strength of the 0-0 transition in the absorption during the titration of PPDI with CB[7]. The authors chemically reduced 0.3 mM solutions of both PPDI and PPDI/CB[7] complexes in water with $Na_2S_2O_4$ and found that PPDI/CB[7] is capable of bearing twice as many radicals as PPDI, as depicted in **Figure 15D**. Quantitative EPR reveals the concentration of these radicals in solution to be 0.016 mM and 0.03 mM, equating to ~5% and 10% doping, respectively. Interestingly, the radical yields for both PPDI and PPDI/CB[7] are concentration dependent, with more radicals populating the PDI scaffolds at higher concentrations. However, the rate of maximum radical anion yield increased more rapidly in PPDI/CB[7] complexes. Since the complexation depresses the formation of aggregates in solution, the authors concluded this to be the cause of higher radical yield in radical anion formation. The authors then performed photothermal conversion experiments, observing that irradiation with an 808 nm light with 1 W cm^{-2} power resulted in a much higher rate of water temperature increase, as well as higher overall water temperature, for the complexes in the comparison with PPDI and the water control (**Figure 16A-B**), and yielded roughly 2x the efficiency of conversion than that of PPDI.[179] Perylene diimides that form stable radical anions often exhibit enhanced performance as photothermal conversion materials,[180] and as such N-PDIs show great promise in cancer phototherapy applications.[181–183]

In subsequent work, various bacterial strain's ability to reduce PPDI/CB[7] complexes in lieu of added chemical reductant was tested. Radical anion formation is observed after incubation of PPDI/CB[7] with E. Coli for 10 hr. Interestingly, this effect is not observed for other bacterial strains, such as *B. Subtilis* and *P. Aeruginosa*. Additionally, other strains produce the effect, including E. Faecalis, and S. aureus each with varying degrees of radical anion being generated. Photothermal conversion treatment in aqueous media was performed on *E. Coli* and *B. Subtilis* strains for their respective strong and non-existent radical formation. **Figure 16C-E** displays thermal imaging of the irradiated samples using the same procedure as in the previous study. While the *B. Subtilis* samples do not show a temperature change, *E. Coli* samples rose to 65ºC in 30 minutes. Other cell lines were also tested, and their radical formation response was measured with electron paramagnetic resonance shown in **Figure 16F**. The authors hypothesize that the presence of bacterial hydrogenases are responsible for radical formation, and thus the therapy could be used for bacterial strains possessing strong reductive capabilities. Bioaccumulation of PPDI/CB[7] in both *E. Coli* and *B. Subtilis* was verified with confocal laser scanning microscopy to ensure that the effect was not a product of accumulation. In terms of cytotoxicity, the authors found PPDI inhibited the growth of both *B. Subtilis* and *E. Coli* bacteria while PPDI/CB[7] permitted their growth, and also showed no clear cytotoxicity toward the nonmalignant HaCaT epithelial cell lines, indicating that these materials could be used in selective photoconversion therapies.[184] The interested reader is also directed to a study where these complexes are used in analyte sensing.[185]
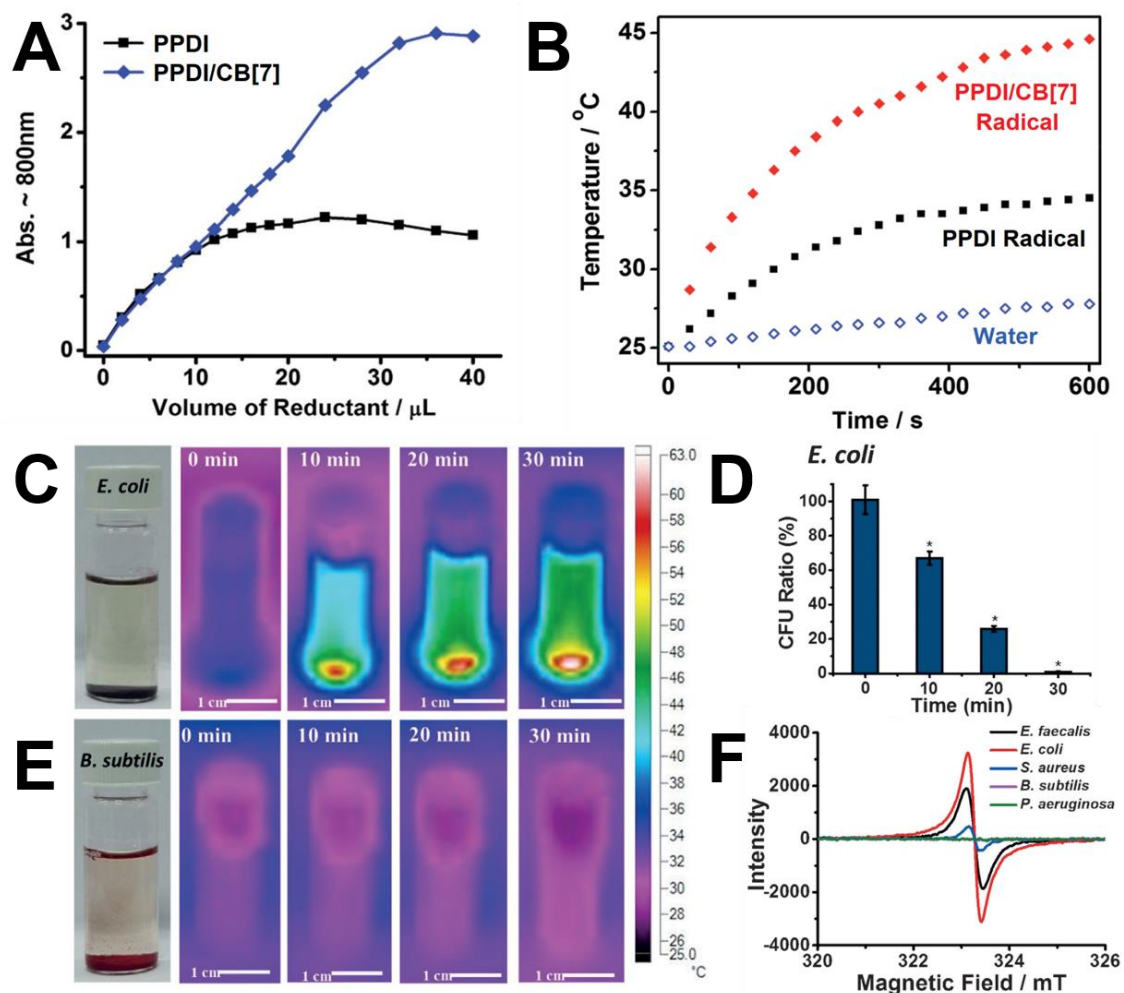
Figure 16. (A) Radical anion concentration (determined by the intensity of the absorption peak at 800 nm) as a function of sodium dithionate reducing agent addition in PPDI and the PPDI/CB[7] supramolecular complex. **(B)** Photothermal conversion data of PPDI and PPDI/CB[7] radicals as a function of irradiation time with an 808 nm laser. **(C)** Thermal images depicting the temperature changes in aqueous PPDI/CB[7] solutions in the presence of *E. Coli* under 808 nm irradiation accompanied by **(D)** the associated colony-forming unit (CFU) ratio. **(E)** Thermal images depicting temperature changes in aqueous PPDI/CB[7] solutions in the presence of *B. subtilis* under 808 nm irradiation. **(F)** Electron paramagnetic resonance data of PPDI/CB[7] solutions in

the presence of various bacteria: *E. faecalis, E. coli, S. aureus, B. subtilis, P. aeruginosa*. Reprinted with permission from ref 184. Copyright 2017 John Wiley & Sons Inc.

4.2 Solar energy

Energy consumption across the globe is expected to increase by ~50% by 2050, and currently the vast majority of energy comes from fossil fuels. Renewables are also the fastest growing energy utility in the US, and solar is projected to surpass wind energy in becoming the dominant source of renewable electricity generation in the U.S. by 2040; the generating capacity of solar across all sectors is expected to grow by more than 5x its current capacity by 2050. Additionally, major production of solar materials has driven down costs by more than 100 times the cost per watt in the 1960s.[186,187] Bulk heterojunction organic photovoltaics (BHJ-OPVs) are low-cost, solution processable, and synthetically modular making them highly attractive as next-generation solar cell devices.[188] Electron transporting layers (ETL) and cathode interlayers are important in BHJ photovoltaics because they help minimize energy losses at the layer interfaces. A diverse range of self-n-doped materials have been reported as efficient ETLs and cathode interlayers in solar cells, some with benchmark performances.[22–24,31,189–194] Numerous examples were recently reviewed elsewhere in excellent detail.[195] N-PDIs have been shown to increase the broadband absorption of active layers, improve ETL homogeneity, and enhance solvent orthogonality for improved processability of BHJs.[196,197] In BHJ-OPV devices, N-PDIs also act as effective ETLs due to their energy level alignment and self-doping character.[198,199] For example, the power conversion efficiency of an (ITO)/PEDOT:PSS/PTB7-Th:PC71BM/ETL/Ag solar cell device that incorporates an N-PDI as an ETL increases from 5.61% (no ETL) up to 10.06%.[129] Various structures may be imagined for N-PDIs as ETLs. Zwitterionic structures show improved

solar cell performance in fully organic BHJ devices, achieving power conversion efficiency values up to 11.23%. Additionally, when compared directly with tertiary amines, the zwitterionic N-PDIs outperforms other structures through improved surface wettability during fabrication.[200–204]

Hybrid perovskite solar cell research has flourished in the last decade and garnered widespread attention from the materials community. N-PDIs have demonstrated superior performance in hybrid perovskite solar cells over some common ETL alternatives. Min et al. compared ZnO and PDINO ETLs in mixed halide p-i-n device stacks shown in **Figure 17A**. Without an ETL, the maximum power conversion efficiency (PCE) is 10%. Incorporation of ZnO improves the PCE by 11.3%, while devices utilizing PDINO as the ETL reach a maximum PCE of 14.0%. The fill factors of the devices linearly increase from the control, to ZnO and PDINO devices by 67.6, 47.5, and 78.5%, respectively due to the favorable contact between PCBM and PDINO, whereas changes in the J_{sc} are attributed to spectral losses in the IR region. External quantum efficiency action spectra of the different devices reveal PDINO devices achieve values ~10-20% greater than ZnO or the control in the ~575-775 nm region. Moreover, different sweep delay times do not induce hysteresis in PDINO devices, and differences in ETL layer thickness (5-24 nm) do not significantly hinder device performance; a phenomenon commonly observed in materials >10 nm thick. The devices are also remarkably stable, retaining 90% efficiency over 300 h in air.[205] N-PDI ETLs also demonstrate excellent performance in perovskite solar cells, achieving 17.66% and 14.32% PCE in rigid and flexible cells respectively.[52]

Wang et al. recently reported the novel QAPDI which features a bay-substituted tertiary amine and quaternary ammonium salt in a hybrid perovskite solar cell as shown in **Figure 17B**. The absorption spectrum of QAPDI shows a broad absorption band from 500-700 nm both in solution and in thin films consistent with N-PDIs substituted at the bay position, and possesses electron

mobility values very close to that of PCBM in electron-only devices (1.05×10^{-3} and 1.21×10^{-3} cm^2 V^{-1} s^{-1}, respectively). The authors compare the performance of QAPDI and the commonly used 4,7-diphenyl-1,10-phenanthroline (Bphen) as ETLs in methylammonium lead iodide (MAPbI$_3$) perovskite solar cell devices (**Figure 17B**). Devices with Bphen exhibit a maximum PCE of 18.6% while QAPDI devices reach a maximum power conversion efficiency of 20.55%, which is one of the highest PCE values for PDI-inclusive devices to date. Additionally, QAPDI films exhibit a lower hysteresis index than control devices, suggesting that these layers are also able to suppress hysteresis in hybrid perovskite solar cell devices. The improved device parameters are attributable to high mobility values, improved electron injectability, reduced recombination, and improved interfacial contact in QAPDI films.[206]
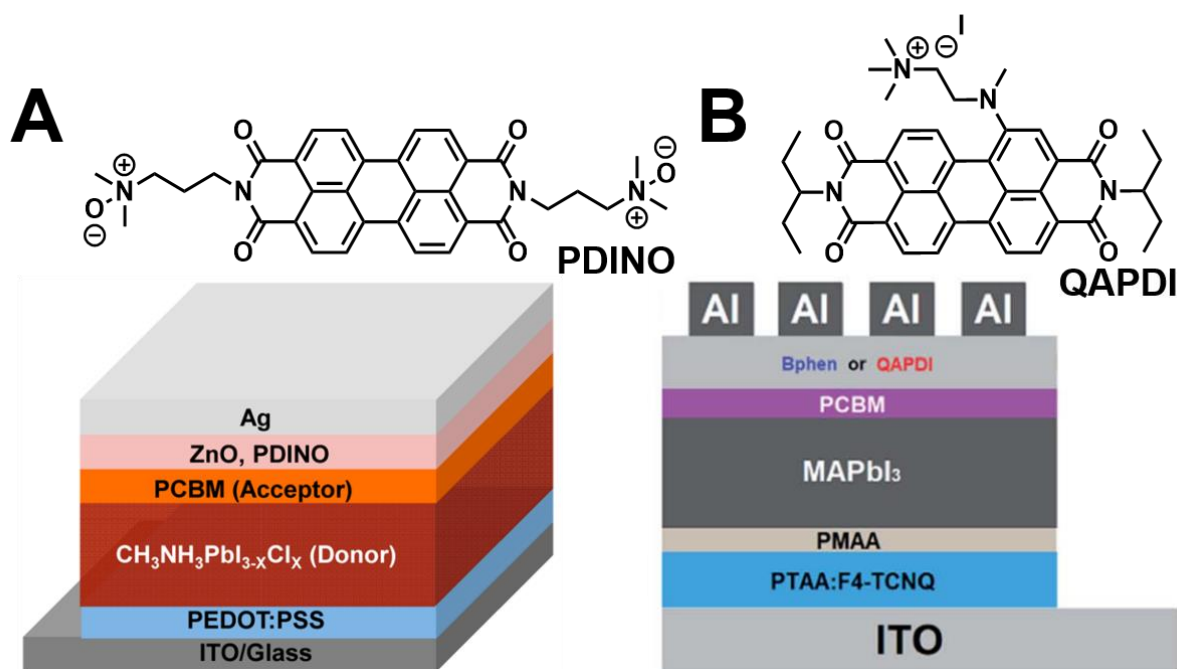

Figure 17. **(A)** Chemical structure of PDINO and the relevant corresponding device stack. Reprinted with permission from ref. 205. Copyright 2015 American Chemical Society. **(B)** Structure of QAPDI and the relevant corresponding device stack. Reproduced from ref. 206. Copyright 2020 The Royal Society of Chemistry.

4.3 Thermoelectricity

In aggregate, roughly 55-65% of the energy produced in the US is rejected as waste heat, with 80% being released as heated gases from 100-300 ℃.[207–209] The development thermoelectric modules efficient at lower temperatures has received considerable attention as a means of recapturing some of this wasted heat and turning it into useful energy. The development of flexible and inexpensive organic semiconductors to meet this end is an area of rapidly growing research.[210–212] Small molecules in particular are attractive as they possess intrinsically low thermal conductivities, are monodisperse, and are amenable to solution processing.[213–218] There are readily discernable advantages of self-doped over extrinsically doped n-type thermoelectric systems. Thermoelectric systems are highly sensitive to the width of the density of states near the Fermi energy.[39] Following charge transfer, these states distort in ways that are very difficult to predict.[219] The incorporation of self-dopants axiomatically narrows the density of state width due to film matrix homogeneity. Additionally, the thermoelectric figure of merit is maximized for a specific carrier concentration within a material that possesses a given material quality factor.[220,221] Sequential doping even at modest concentrations can alter the morphology of thin films and change the material quality factor, thus rendering carrier concentration tuning problematic in these systems. Self-doped systems, on the other hand, have a single quality factor. Because the spin density can be thermally and photoactivated, self-doping offers a promising method of optimizing the figure of merit in a manner that has yet to be explored in depth. Russ et al. examined the thermoelectric properties of PDIs self-doped with quaternary trimethylammonium hydroxides with varying $-(CH_2)_n$ tether length between the core and the dopant. Changing the tether length from n=2 to 4 and 6 has little effect on the Seebeck coefficient (~-200 μV/K), but dramatically

increases the electrical conductivity of thin films by over two orders of magnitude from ~0.001 to ~0.4 S/cm. The power factor is more commonly reported in organic thermoelectric materials and is directly proportional to the thermoelectric figure of merit. The n=6 N-PDI has a power factor of 1.4 μW/mK^2, which is one of the highest power factors reported in n-type small molecule organic thermoelectric materials.[82]

N-PDIs can also be incorporated into composite materials. Work by Wu et al. has shown promising results in this regard. A composite thermoelectric material composed of high-conductivity single-walled carbon nanotubes (SCWNT) and PDINE (**Figure 18A**) combines the excellent properties of these two materials. The Seebeck coefficient of pristine SCWNT films (p-type), and SCWNT composite materials (n-type) with various electron dopants is shown in **Figure 18B** (including a self-doped naphthalene diimide NDINE). Compared to other reducing agents, PDINE and NDINE composites have considerably larger Seebeck coefficients. The films exhibit excellent air stability for n-type semiconductors with 83.5% conductivity remaining after 100 hr of air exposure. The conductivity, Seebeck coefficient, and resulting power factor are plotted as a function of SCWNT/PDINE mass ratio in **Figure 18C**. The power factor of the composite is maximized at a 10:5 mass ratio to 112 ± 8 μW/mK^2 under a 50 ºC temperature gradient, which is one of the highest power factors for n-type organic and organic/inorganic composite materials.[54]
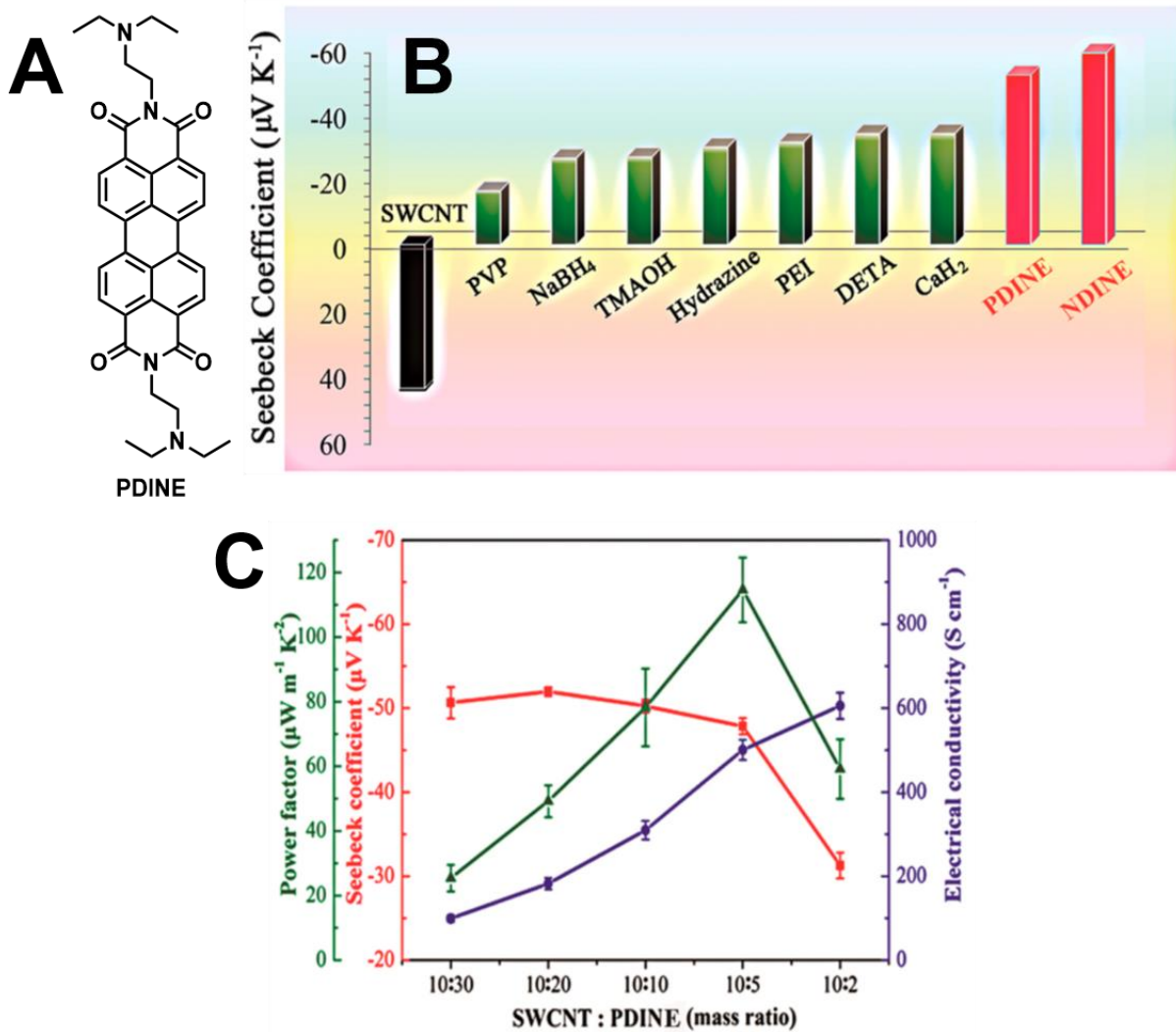
Figure 18. (A) P/N Seebeck coefficient switching of SWCNT following modification with several n-type dopants, most notably with (B) PDINE and NDINE. (C) Electrical conductivity (blue), Seebeck coefficient (red), and power factor (green) of SWCNT : PDINE composites at various mass ratios. (Note: polyvinylpyrrolidone [PVP], trimethylammonium hydroxide [TMAOH], poly(ether imide) [PEI], diethylenetriamine [DETA]). Reprinted with permission from ref. 54. Copyright 2017 American Chemical Society.

4.4 Energy Storage

In recent decades there has been unprecedented growth in battery operated devices from cellular phones and laptops to the internet of things, wearable devices for personal and medical use, and radio-frequency identification technology. Redox-active organic molecules are very attractive in battery applications because they are often capable of multi-electron transfer and could be used to create high energy density systems. Additionally, their low carbon footprint and solution processability make them likely candidates. N-type materials have shown great promise for their redox activity, and recent emphasis has been placed on increasing their intrinsic electronic conductivity to improve power density and increase mass loading to improve energy density for long-term performance improvements.[222] Additionally, many state-of-the-art organic materials are plagued by low specific capacity, or are unstable to multiple cycling events.[223] An organic compounds' theoretical capacity is determined by its electron affinity, while cyclability depends on the chemical reversibility of this process. It has been demonstrated that strong n-type doping of organic compounds can improve Coulombic efficiency and specific capacity.[224,225] The intrinsic n-type doping of N-PDIs, coupled with their good electron conductivity and mobility make them attractive in battery applications.

Supur et al. combined an N-PDI with a two-carbon tether and ammonium iodide named TAIPDI with reduced graphene oxide (RGO) to form TAIPDI/RGO composites. TAIPDI is able to then self-assemble onto the surface of the graphene, as previously reported.[226]. Thermogravimetric analysis of the individual components and the TAIPDI/RGO composite show that TAIPDI decomposes at a higher temperature in the composites, demonstrating electrostatic interaction between the respective species. Scanning electron micrographs of TAIPDI/RGO show even dispersion of TAIPDI on the surface of graphene, which could potentially be increased by

self-assembly tailoring. Cathode films incorporated into lithium-ion batteries were constructed with 80 wt% composite, 15 wt% carbon, and 5 wt% polyvinylidene fluoride binder. The devices exhibit a specific capacity of 81.5 mA h g^{-1} at a current density of 25 mA g^{-1} and retain 73% of the initial reversible capacity after 500 cycles. The Coulombic efficiency of the half-cell remains at ~99% for the duration of the 500 cycles at 25 mA g^{-1} implying long life cycles for the composites.[227] Graphene/N-PDI composites have also been used as sodium battery cathode materials, and the interested reader is directed here.[55]

The lack of an efficient and scalable large-scale energy storage solution that can stabilize the intermittency of renewable electricity sources is rapidly becoming a pressing issue. Redox flow batteries (RFBs) have garnered attention in recent years as they are seen as one of the most attractive targets for stationary energy storage with high capacity for industrial scaling.[228,229] However, widespread adoption is restricted due to high cost, and use of low abundance or hazardous materials. Organic RFBs are thus attractive but have lagged behind due to instability of the charged electrolytes.[230] Recent work by Milton et al. yielded fully organic nonaqueous flow batteries comprised of a [PDI][TFSI]$_2$ anolyte coupled to a tetraferrocene [Fc$_4$] catholyte separated by a dialysis membrane (**Figure 19A-B**). The RFBs were tested at both low and high concentrations. The low concentration stirred H-cell composed of 1.17 mM [Fc$_4$] and 1.8 mM [PDI][TFSI]$_2$ can sustain >230 cycles at 1C while maintaining an average Coulombic efficiency of 99.955% (**Figure 19C**). The cell exhibits excellent stability, with the charge and discharge capacity settling after 40 cycles and retaining it for over 200 with very little fade. Additionally, the cell can be left in its charged state for 11 days without any capacity loss due to the stability of the radicals that form during operation. The high concentration cell tested in **Figure 19D** is comprised of 0.1 M [Fc$_4$] and 0.2 M [PDI][TFSI]$_2$, equivalent to 0.4 mol electron/liter which rivals that of

benchmark organic media RFBs. The high concentration cell exhibits steady performance over >450 cycles with an average Coulombic efficiency of 99.868% and 68% energy efficiency.[231] It should be noted that PDIs generally suffer from a low energy density due to their undesirable redox potential (-0.7 V vs Ag/Ag$^+$). Future work in this area to widen the potential window and PDI solubility will likely lead to the realization of practical RFBs incorporating N-PDIs.
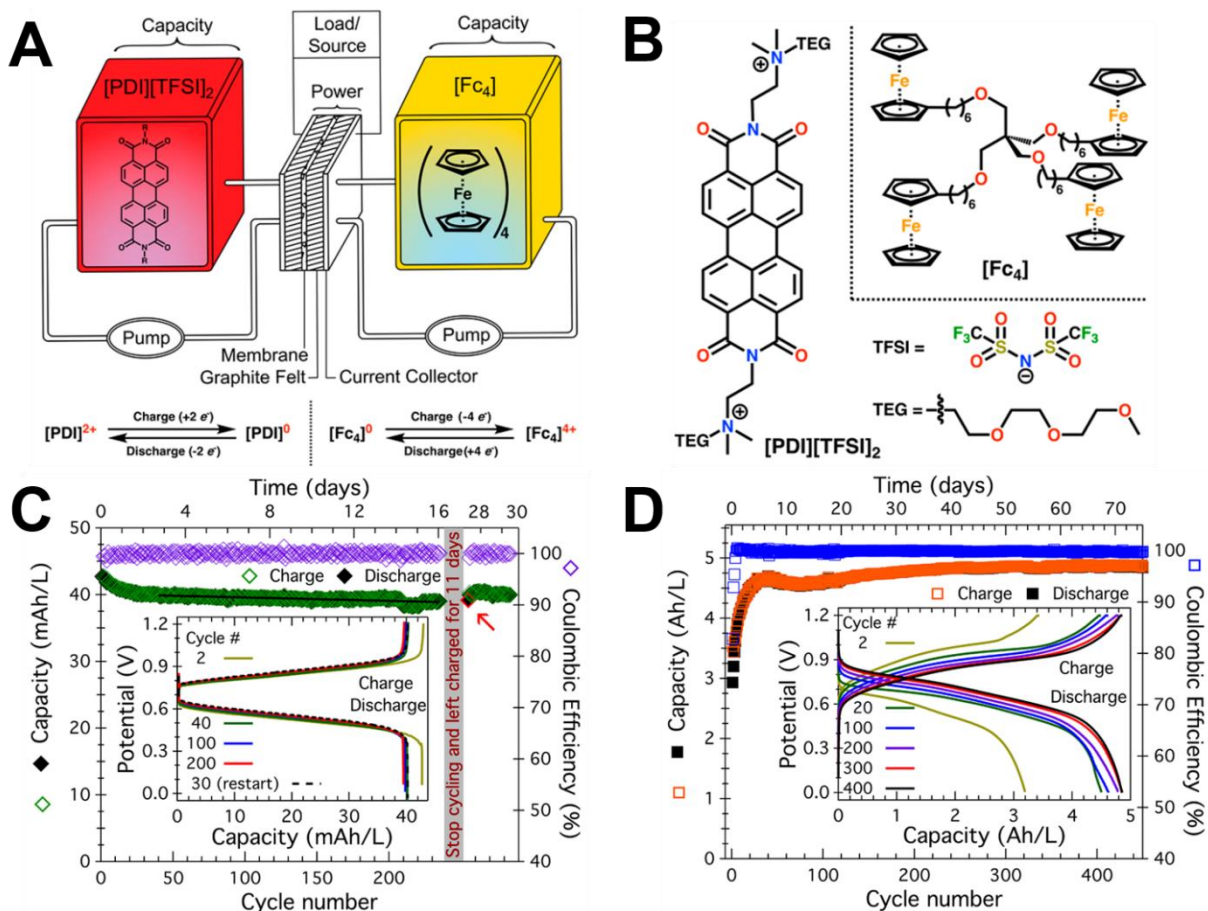
Figure 19. (A) Schematic diagram of the redox flow battery and the corresponding redox reactions of [PDI][TFSI]$_2$ and [Fc$_4$], whose structures are given in **(B)**. **(C)** Output performance of a low concentration cell comprised of 1.17 mM [Fc$_4$] and 1.8 mM [PDI][TFSI]$_2$. The Coulombic efficiency (purple diamonds) has an average of 99.955%. Repeated charge (green diamonds)/discharge (black diamonds) cycling at 1C over >230 cycles in a stirred H-cell

configuration. The first discharge (red diamond) and selected charge/discharge profiles for the cell (inset) are also displayed. **(D)** Output performance of a high concentration cell comprised of 100 mM [Fc$_4$] and 200 mM [PDI][TFSI]$_2$. The Coulombic efficiency (blue squares) has an average of 99.868% above cycle 5. Repeated charge (orange square)/discharge (black square) capacities over >450 cycles corresponding to >74 days of operation, along with selected charge/discharge profiles for the cell (inset) are shown. Li[TFSI] was used as supporting electrolyte in both cells **C** and **D**, and the voltage was limited from 0 to 1.2 V. Reprinted with permission from ref. 231. Copyright 2017 American Chemical Society.

4.5 Photocatalysis

Photosynthesis is the primary source of atmospheric oxygen, and its importance in evolutionary history cannot be overstated. Artificial photosynthesis with molecular catalysts aims to produce carbon neutral fuel feedstocks through a variety of reactions, such as water splitting or hydrogen reduction.[232,233] Compounds that form long-lived photoinduced charge transfer states are commonly used in artificial photosynthesis.[234] Photoelectrochemical methods of converting solar energy into electrical energy have attracted considerable attention in recent years due to its cost efficiency over photovoltaic/electrolyzer systems, but require materials able to withstand harsh photo-corrosive environments.[235] The excellent photostability, large molar extinction coefficient, strong π-stacking, and amphiphilic structure of PDIs make them excellent candidates for photoelectrochemical catalytic systems. For solar water splitting, the most demanding portion of the reaction is the 4-electron reduction of water, and powerfully oxidizing holes are required to drive the reaction forward.[236] While the use of oxidative metal oxide photoanodes was known, Ronconi et al. developed a strategy of sensitizing WO$_3$ and SnO$_2$ by soaking the oxides in

acetonitrile solutions containing PDI$^+$PF$_6^-$ (**Figure 20A**) for improved photoanodic current. The coordination of PDI$^+$PF$_6^-$ to porous WO$_3$, TiO$_2$, and SnO$_2$ results in blue-shifted H-aggregate absorption features of PDI$^+$PF$_6^-$ on the metal oxide surfaces and strongly positive holes as verified by cyclic voltammetry (E$_{ox}$ ~1.7 V vs SCE). In the presence of an acetonitrile/0.1 M LiI sacrificial reductant, the photoanodic current increases upon photoirradiation, consistent with electron injection from PDI$^+$PF$_6^-$ to the metal oxide and hole transfer from the reductant to PDI$^+$PF$_6^-$ as shown in **Figure 20B**. The largest photocurrent of 0.5 mA/cm^2 is that of PDI$^+$PF$_6^-$ /WO$_3$ under a 0.35 V bias vs SCE. The injection rates are estimated with time-correlated single photon counting to be k$_{inj}$(WO$_3$)=0.4x10^9 s^{-1}, k$_{inj}$(SnO$_2$)=0.1x10^9 s^{-1}, and k$_{inj}$(TiO$_2$)=0.05x10^9 s^{-1}. The performance of the composite photoanodes is thus attributed to electron injectability. PDI$^+$PF$_6^-$/WO$_3$ photoanodes were functionalized with IrO$_2$ nanoparticles under various processing conditions as an example water oxidation catalyst (**Figure 20C**). Under 1.5 G illumination in 0.1 M NaClO$_4$ and pH = 3 (no sacrificial reductant), the co-deposited electrodes exhibit photocurrent close to 70 µA/cm^2 at 0.5 V vs SCE. The presence of IrO$_2$ increases the photocurrent density ~6-fold in comparison with PDI$^+$PF$_6^-$/WO$_3$ electrodes alone due to the efficient hole transfer from photogenerated PDI$^+$PF$_6^-$ to IrO$_2$.[59] Sensitized PDI$^+$PF$_6^-$/SnO$_2$ photoanodes have also been studied for HBr splitting as an alternative H$_2$ solar fuel production method, and the interested reader is directed here.[237,238] Tertiary amine nanofibers have also been used as TiO$_2$ photoanode sensitizers for the photo-electrocatalytic generation of hydrogen gas. In aqueous 0.2 M HCl electrolyte and triethylamine as a sacrificial hole trap, a maximum photocurrent of ~40 µA/cm^2 at 0.6 V vs Ag/AgCl is obtained to generate 4-8 µmol h^{-1}g^{-1}, which is also an excellent benchmark in comparison to similar systems.[239] Similar work has been done on phosphonate substituted PDIs

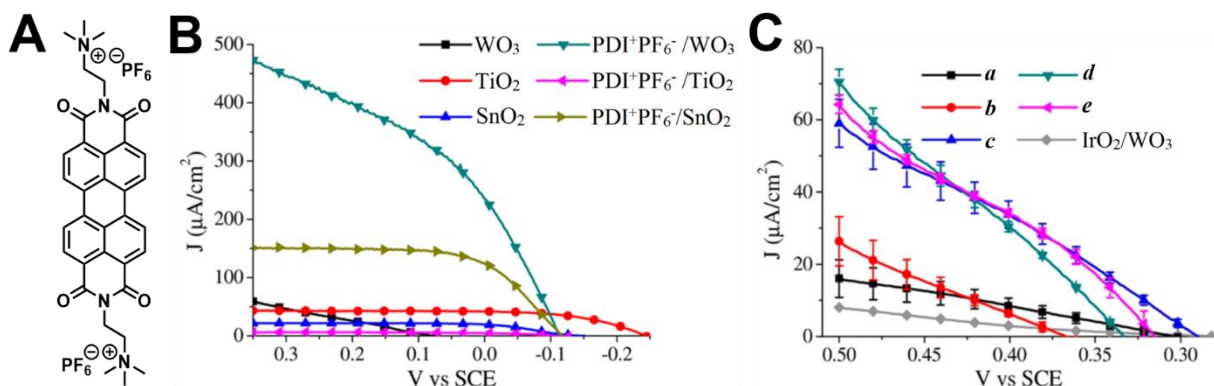by Kirner et al., offering an interesting strategy of altering N-PDIs by exchanging nitrogen with heavier pnictogens.[240]

Figure 20. (A) Chemical structure of $PDI^+PF_6^-$. **(B)** *J—V* curves of electrodes with and without the application of the $PDI^+PF_6^-$ sensitizer in the presence of acetonitrile/0.1 M LiI. The current densities shown are obtained by subtracting their respective dark currents. **(C)** *J—V* curves of different batches of $PDI^+PF_6^-/WO_3$ photoelectrodes with (***b-e***) and without (***a***) and IrO_2 modifier. Reprinted with permission from ref. 59. Copyright 2015 American Chemical Society.

Beyond sensitizing photoanodes, N-PDIs can also directly sensitize the catalyst. Dicationic N,N′ -bis(2-(trimethylammonium)ethylene)perylene-3,4,9,10- tetracarboxylic acid Diimide can be directly coordinated to the polyoxometalate $[Ru_4(\mu\text{-}O)_4(\mu\text{-}OH)_2(H_2O)_4(\gamma\text{-}SiW_{10}O_{36})_2]^{10-}$ (Ru_4POM) deca-anion as a biomimetic quantasome photosystem II water oxidation catalyst. Ru_4POM has a low overpotential of 300-350 mV, wide operational pH range of 1-7, and ultrafast photoinduced electron transfer making it an attractive target for PDI functionalization.[241] PDI readily coordinates to the Ru_4POM catalyst in water, with 5 PDIs units to each Ru_4POM to form $[PDI]_5Ru_4POM$ as core-shell cylindrical amphiphiles (**Figure 21A**). Small and wide-angle X-ray

scattering reveal that these cylinders pack closely together with a mosaicity of 10-15º in a paracrystalline phase which then stack into 2D lamellar superstructures. [PDI]$_5$Ru$_4$POM can then be templated onto nanostructured WO$_3$ photoanodes to create a regenerative photoelectrochemical cell. Photoelectrochemical cell measurements of NanoWO$_3$|{[PDI]$_5$Ru$_4$POM}$_n$ were done in aqueous 1 mM HClO$_4$/0.1 M NaClO$_4$ at pH = 3 in the 0.51-0.91 V vs RHE potential window at 20 mV s^{-1} under 1.5 G illumination (λ > 450 nm). The onset potential of the photoelectrochemical cell under illumination is near the saturation plateau of > 40 µA cm^{-2} at <0.6 V and 0.91 V revealing fast hole scavenging and catalysis, as shown in **Figure 21B**. The incident photon-to-current efficiency action spectrum aligns with the absorption spectrum of {[PDI]$_5$Ru$_4$POM}$_n$ with the peak 0.5% efficiency in the same range as the absorption maximum (**Figure 21C**). The absorbed photon-to-current efficiency of the photoelectrochemical cell is found to be ~1.3% in the 470-540 nm range.[50] This considerably outperformed other state-of-the-art Ru$_4$POM sensitized photoanodes.[59,242,243] N-PDIs thus act as efficient sensitizers of both photoanodes and catalysts in photoelectrochemical cells.
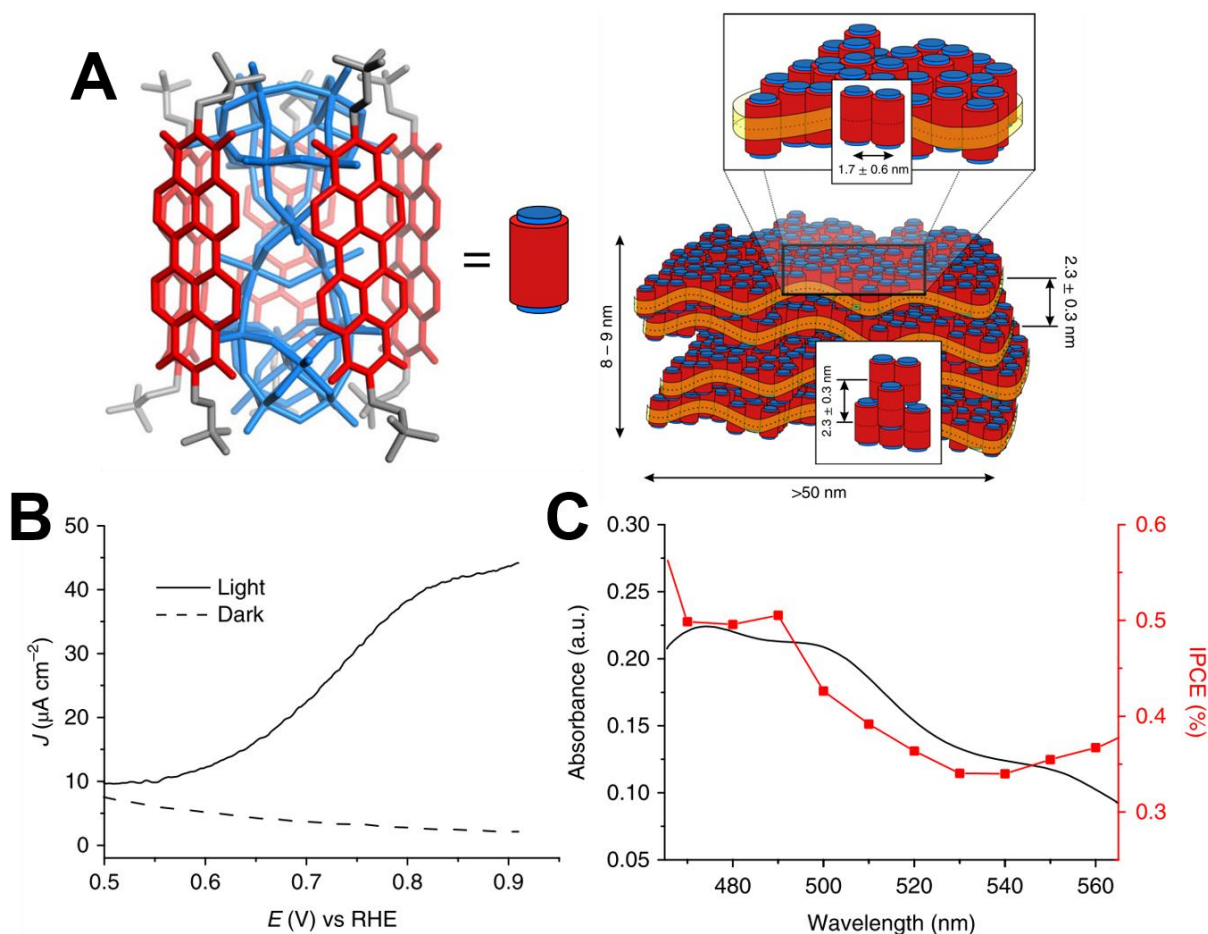
Figure 21. **(A)** Representation of the [PDI]$_5$Ru$_4$POM coordination complex as a cylindrical amphiphile with the Ru$_4$POM building block shown in blue, the aromatic PDI in red, and the alkylammonium tails in grey. Additionally, the hierarchical ordering of these complexes into nanolamellae and their mean separation distances are shown. **(B)** Photocurrent density (solid) compared to dark current density (dashed) of a NanoWO$_3$|{[PDI]$_5$Ru$_4$POM}$_n$ as a function of applied potential under simulated solar irradiation in aqueous HClO4 pH 3, 0.1 M NaClO4. **(C)** Action spectrum of a NanoWO$_3$|{[PDI]$_5$Ru$_4$POM}$_n$ photoanode showing the absorption spectrum (black) overlaid with the internal power conversion efficiency (red) as a function of irradiation wavelength. Reprinted with permission from ref. 50. Copyright 2018 Springer Nature.

5. CONCLUSION AND OUTLOOK

We have reviewed the intrinsic properties of PDIs, and how these are altered by the incorporation of electron rich moieties. PDIs are one of the most extensively utilized organic scaffolds in semiconductor research due to their excellent photostability, tunability, and photophysical properties. Many structural modifications to the PDI scaffold do not significantly alter the physicochemical properties of the chromophore. However, the incorporation of tertiary amines or quaternary ammonium substituents at the bay or imide positions create self-n-doped N-PDIs capable of radical anion and dianion formation. The self-n-doping character of N-PDIs, coupled with their amphiphilic nature separates this class from other structural derivatives, and they have demonstrated remarkable promise across a wide breadth of fields including biochemistry, energy harvesting, and energy storage. We have discussed how doping efficiency in N-PDIs depends on the dopant architecture, attachment distance, and attachment mode to the PDI core.

In recent years, an increasingly diverse range of self-n-doped materials have appeared in the literature; many exhibiting benchmark performances in numerous applications. However, little attention has been paid to establishing self-dopant design principles. Dopant structure-function relationships are in their infancy. It is not clearly understood why certain architectures undergo structural degradation, nor how degradation affects device performance. Many new approaches may be taken to modify the dopant architecture, such as aromatization, structural rigidity, or substitution of heavier pnictogens. These modifications can also be paired with modifications to the host. Thionation of the carbonyls and addition of electron withdrawing groups to the PDI core have not been paired and explicitly investigated for self-n-doping properties. As with other n-type materials, one of the major challenges to be addressed is improving air stability, which could be

enhanced by modifying the PDI scaffold. A thorough understanding of these features would likely enable further performance enhancements beyond those that have been already been realized. Additionally, a deeper understanding of the relationship between dopant architecture and its influence on self-assembly is lacking. The literature regarding self-n-doping materials is often fragmented by intended application, leading some researchers to neglect amine/ammonium doping or even wrongly attribute doping to other species present in their systems. It is our hope that this work will inform and encourage others to study the many unique and often surprising behaviors of self-n-doped materials.

ACKNOWLEDGEMENTS

REFERENCES

(1)   Salzmann, I.; Heimel, G.; Oehzelt, M.; Winkler, S.; Koch, N. Molecular Electrical Doping of Organic Semiconductors: Fundamental Mechanisms and Emerging Dopant Design Rules. *Accounts of Chemical Research* **2016**, *49* (3), 370–378. https://doi.org/10.1021/acs.accounts.5b00438.

(2)   Salzmann, I.; Heimel, G.; Duhm, S.; Oehzelt, M.; Pingel, P.; George, B. M.; Schnegg, A.; Lips, K.; Blum, R. P.; Vollmer, A.; Koch, N. Intermolecular Hybridization Governs Molecular Electrical Doping. *Physical Review Letters* **2012**, *108* (3), 1–5. https://doi.org/10.1103/PhysRevLett.108.035502.

(3)   Kolesov, V. A.; Fuentes-Hernandez, C.; Chou, W.-F.; Aizawa, N.; Larrain, F. A.; Wang, M.; Perrotta, A.; Choi, S.; Graham, S.; Bazan, G. C.; Nguyen, T.-Q.; Marder, S. R.; Kippelen, B. Solution-Based Electrical Doping of Semiconducting Polymer Films over a Limited Depth. *Nature Materials* **2016**, *1*, 1–8. https://doi.org/10.1038/nmat4818.

(4)   Salzmann, I.; Heimel, G. Toward a Comprehensive Understanding of Molecular Doping Organic Semiconductors (Review). *Journal of Electron Spectroscopy and Related Phenomena* **2015**, *204*, 208–222. https://doi.org/10.1016/j.elspec.2015.05.001.

(5)   Schlitz, R. A.; Brunetti, F. G.; Glaudell, A. M.; Miller, P. L.; Brady, M. A.; Takacs, C. J.; Hawker, C. J.; Chabinyc, M. L. Solubility-Limited Extrinsic n-Type Doping of a High Electron Mobility Polymer for Thermoelectric Applications. *Advanced Materials* **2014**, *26* (18), 2825–2830. https://doi.org/10.1002/adma.201304866.

(6)   Liu, J.; Qiu, L.; Portale, G.; Koopmans, M.; ten Brink, G.; Hummelen, J. C.; Koster, L. J. A. N-Type Organic Thermoelectrics: Improved Power Factor by Tailoring Host–Dopant Miscibility. *Advanced Materials* **2017**, *29* (36), 1–8. https://doi.org/10.1002/adma.201701641.

(7)   Qiu, L.; Liu, J.; Alessandri, R.; Qiu, X.; Koopmans, M.; Havenith, R. W. A.; Marrink, S. J.; Chiechi, R. C.; Anton Koster, L. J.; Hummelen, J. C. Enhancing Doping Efficiency by Improving Host-Dopant Miscibility for Fullerene-Based n-Type Thermoelectrics. *Journal of Materials Chemistry A* **2017**, *5* (40), 21234–21241. https://doi.org/10.1039/c7ta06609k.

(8)   Tietze, M. L.; Benduhn, J.; Pahner, P.; Nell, B.; Schwarze, M.; Kleemann, H.; Krammer, M.; Zojer, K.; Vandewal, K.; Leo, K. Elementary Steps in Electrical Doping of Organic Semiconductors. *Nature Communications* **2018**, *9* (1), 1–9. https://doi.org/10.1038/s41467-018-03302-z.

(9)   Ikenoue, Y.; Chiang, J.; Patil, A. O.; Wudl, F.; Heeger, A. J. Verification of the "Cation Popping" Doping Mechanism of Self-Doped Polymers. *Journal of the American Chemical Society* **1988**, *110*, 2983–2985. https://doi.org/10.1021/ja00217a055.

(10)   Mai, C. K.; Schlitz, R. A.; Su, G. M.; Spitzer, D.; Wang, X.; Fronk, S. L.; Cahill, D. G.; Chabinyc, M. L.; Bazan, G. C. Side-Chain Effects on the Conductivity, Morphology, and Thermoelectric Properties of Self-Doped Narrow-Band-Gap Conjugated Polyelectrolytes. *Journal of the American Chemical Society* **2014**, *136* (39), 13478–13481. https://doi.org/10.1021/ja504284r.

(11)   Kondratiev, V. v.; Holze, R. Intrinsically Conducting Polymers and Their Combinations with Redox-Active Molecules for Rechargeable Battery Electrodes: An Update. *Chemical Papers*. Springer

Science and Business Media Deutschland GmbH October 1, 2021, pp 4981–5007. https://doi.org/10.1007/s11696-021-01529-7.

(12)   Brimage, D. R. G.; Davidson, R. S. Effect of Intramolecular Exciplex Formation upon the Photoreactivity of Naphthylalkylamines and Anthrylalkylamines. *Journal of the Chemical Society D: Chemical Communications* **1971**, 1385–1386. https://doi.org/10.1039/C29710001385.

(13)   Okada, T.; Migita, M.; Mataga, N.; Sakata, Y.; Misumi, S. Picosecond Laser Spectroscopy of Intramolecular Heteroexcimer Systems. Time-Resolved Absorption Studies of p-(CH3)2NC6H4(CH2)n(1-Pyrenyl) and -(9-Anthryl) Systems. *Journal of the American Chemical Society* **1981**, *103*, 4715–4720. https://doi.org/10.1021/ja00406a009.

(14)   Schnurpfeil, G.; Stark, J.; Whörle, D. Syntheses of Uncharged, Positively and Negatively Charged 3,4,9,10-Perylene-Bis(Dicarboximides). *Dyes and Pigments* **1995**, *27* (4), 339–350. https://doi.org/10.1016/0143-7208(94)00075-D.

(15)   Riichiro Ide, B.; Sakata, Y.; Misumi, S.; Okada, T.; Mataga, N.; Chandross, A.; Thomas, H. T. Intramolecular Exciplex Formation in Some Compounds Containing Condensed Aromatic Hydrocarbon and NN-Dimethylaniline Moieties. *Chem. Phys. Letters* **1972**, *9*, 1385. https://doi.org/10.1039/C39720001009.

(16)   Andrews, L. J. Aromatic Molecular Complexes of the Electron Donor-Acceptor Type. *Chemical Reviews* **1954**, *54* (5), 713–776. https://doi.org/10.1021/cr60171a001.

(17)   Miller, J. S.; Calabrese, J. C. Formation of a Zwitterionic Donor-Acceptor Compound Based on N,N,N',N'-Tetramethyl-Pphenylenediamine and 7,7,8,8-Tetracyanoperfluoro-Pquinodimethane. *Journal of the Chemical Society, Chemical Communications* **1988**, 63–64. https://doi.org/10.1039/C39880000063.

(18)   Amerling, E.; Zhai, Y.; Larson, B. W.; Yao, Y.; Fluegel, B.; Owczarczyk, Z.; Lu, H.; Whittaker-Brooks, L.; Blum, V.; Blackburn, J. L. Charge Transfer States and Carrier Generation in 1D Organolead Iodide Semiconductors. *Journal of Materials Chemistry A* **2021**, *9* (26), 14977–14990. https://doi.org/10.1039/d1ta03325e.

(19)   Liu, J. J.; Guan, Y. F.; Jiao, C.; Lin, M. J.; Huang, C. C.; Dai, W. X. A Panchromatic Hybrid Crystal of Iodoplumbate Nanowires and J-Aggregated Naphthalene Diimides with Long-Lived Charge-Separated States. *Dalton Transactions* **2015**, *44* (13), 5957–5960. https://doi.org/10.1039/c4dt03785e.

(20)   Proppe, A. H.; Tremblay, M. H.; Zhang, Y.; Yang, Z.; Quintero-Bermudez, R.; Kelley, S. O.; Barlow, S.; Marder, S. R.; Sargent, E. H. Naphthalenediimide Cations Inhibit 2D Perovskite Formation and Facilitate Subpicosecond Electron Transfer. *Journal of Physical Chemistry C* **2020**, *124* (44), 24379–24390. https://doi.org/10.1021/acs.jpcc.0c05521.

(21)   Tremblay, M. H.; Zeidell, A. M.; Rigin, S.; Tyznik, C.; Bacsa, J.; Bacsa, J.; Zhang, Y.; al Kurdi, K.; Jurchescu, O. D.; Timofeeva, T. v.; Barlow, S.; Marder, S. R. Structural Diversity in 2,2'-[Naphthalene-1,8:4,5-Bis(Dicarboximide)- N,N'-Diyl]-Bis(Ethylammonium) Iodoplumbates. *Inorganic Chemistry* **2020**, *59* (12), 8070–8080. https://doi.org/10.1021/acs.inorgchem.0c00165.

(22) Jia, J.; Fan, B.; Xiao, M.; Jia, T.; Jin, Y.; Li, Y.; Huang, F.; Cao, Y. N-Type Self-Doped Water/Alcohol-Soluble Conjugated Polymers with Tailored Energy Levels for High-Performance Polymer Solar Cells. *Macromolecules* **2018**, *51* (6), 2195–2202. https://doi.org/10.1021/acs.macromol.8b00126.

(23) Wang, S.; Li, Z.; Xu, X.; Zhang, M.; Zhang, G.; Li, Y.; Peng, Q. Self-Doping Small Molecular Conjugated Electrolytes Enabled by n-Type Side Chains for Highly Efficient Non-Fullerene Polymer Solar Cells. *Journal of Materials Chemistry A* **2018**, *6* (45), 22503–22507. https://doi.org/10.1039/c8ta08948e.

(24) Lee, B. H.; Jung, I. H.; Woo, H. Y.; Shim, H. K.; Kim, G.; Lee, K. Multi-Charged Conjugated Polyelectrolytes as a Versatile Work Function Modifier for Organic Electronic Devices. *Advanced Functional Materials* **2014**, *24* (8), 1100–1108. https://doi.org/10.1002/adfm.201301810.

(25) Gao, C.; Liu, Y.; Gao, Y.; Zhou, Y.; Zhou, X.; Yin, X.; Pan, C.; Yang, C.; Wang, H.; Chen, G.; Wang, L. High-Performance n-Type Thermoelectric Composites of Acridones with Tethered Tertiary Amines and Carbon Nanotubes. *Journal of Materials Chemistry A* **2018**, *6* (41), 20161–20169. https://doi.org/10.1039/c8ta08045c.

(26) Keshri, S. K.; Mandal, K.; Kumar, Y.; Yadav, D.; Mukhopadhyay, P. Naphthalenediimides with High Fluorescence Quantum Yield: Bright-Red, Stable, and Responsive Fluorescent Dyes. *Chemistry - A European Journal* **2021**, *27* (23), 6954–6962. https://doi.org/10.1002/chem.202100020.

(27) Tang, H.; Liu, Z.; Tang, Y.; Du, Z.; Liang, Y.; Hu, Z.; Zhang, K.; Huang, F.; Cao, Y. Organic Diradicals Enabled N-Type Self-Doped Conjugated Polyelectrolyte with High Transparency and Enhanced Conductivity. *Giant* **2021**, *6*. https://doi.org/10.1016/j.giant.2021.100053.

(28) Li, C. Z.; Chueh, C. C.; Yip, H. L.; Ding, F.; Li, X.; Jen, A. K. Y. Solution-Processible Highly Conducting Fullerenes. *Advanced Materials* **2013**, *25* (17), 2457–2461. https://doi.org/10.1002/adma.201204543.

(29) Zhao, C.; Tang, C. G.; Seah, Z. L.; Koh, Q. M.; Chua, L. L.; Png, R. Q.; Ho, P. K. H. Improving Organic Photovoltaic Cells by Forcing Electrode Work Function Well beyond Onset of Ohmic Transition. *Nature Communications* **2021**, *12* (1). https://doi.org/10.1038/s41467-021-22358-y.

(30) Tang, C. G.; Ang, M. C. Y.; Choo, K. K.; Keerthi, V.; Tan, J. K.; Syafiqah, M. N.; Kugler, T.; Burroughes, J. H.; Png, R. Q.; Chua, L. L.; Ho, P. K. H. Doped Polymer Semiconductors with Ultrahigh and Ultralow Work Functions for Ohmic Contacts. *Nature* **2016**, *539* (7630), 536–540. https://doi.org/10.1038/nature20133.

(31) O'Malley, K. M.; Li, C. Z.; Yip, H. L.; Jen, A. K. Y. Enhanced Open-Circuit Voltage in High Performance Polymer/Fullerene Bulk-Heterojunction Solar Cells by Cathode Modification with a C 60 Surfactant. *Advanced Energy Materials* **2012**, *2* (1), 82–86. https://doi.org/10.1002/aenm.201100522.

(32) Sun, X.; Chen, W.; Liang, L.; Hu, W.; Wang, H.; Pang, Z.; Ye, Y.; Hu, X.; Wang, Q.; Kong, X.; Jin, Y.; Lei, M. Construction of Electron Transfer Network by Self-Assembly of Self-n-Doped Fullerene Ammonium Iodide. *Chemistry of Materials* **2016**, *28* (23), 8726–8731. https://doi.org/10.1021/acs.chemmater.6b04056.

(33)   Bradley, C.; Lonergan, M. C. Limits on Anion Reduction in an Ionically Functionalized Fullerene by Cyclic Voltammetry with: In Situ Conductivity and Absorbance Spectroscopy. *Journal of Materials Chemistry A* **2016**, *4* (22), 8777–8783. https://doi.org/10.1039/c6ta01479h.

(34)   Chen, W.; Jiao, W.; Li, D.; Sun, X.; Guo, X.; Lei, M.; Wang, Q.; Li, Y. Cross Self-n-Doping and Electron Transfer Model in a Stable and Highly Conductive Fullerene Ammonium Iodide: A Promising Cathode Interlayer in Organic Solar Cells. *Chemistry of Materials* **2016**, *28* (4), 1227–1235. https://doi.org/10.1021/acs.chemmater.6b00214.

(35)   Jiao, W.; Ma, D.; Lv, M.; Chen, W.; Wang, H.; Zhu, J.; Lei, M.; Chen, X. Self N-Doped [6,6]-Phenyl-C61-Butyric Acid 2-((2-(Trimethylammonium)Ethyl)- (Dimethyl)Ammonium) Ethyl Ester Diiodides as a Cathode Interlayer for Inverted Polymer Solar Cells. *Journal of Materials Chemistry A* **2014**, *2* (35), 14720–14728. https://doi.org/10.1039/c4ta02682a.

(36)   Tang, C. G.; Syafiqah, M. N.; Koh, Q. M.; Zhao, C.; Zaini, J.; Seah, Q. J.; Cass, M. J.; Humphries, M. J.; Grizzi, I.; Burroughes, J. H.; Png, R. Q.; Chua, L. L.; Ho, P. K. H. Multivalent Anions as Universal Latent Electron Donors. *Nature* **2019**, *573* (7775), 519–525. https://doi.org/10.1038/s41586-019-1575-7.

(37)   Faulkner, E. B.; Schwartz, R. J. *High Performance Pigments*, 2nd edition.; Wiley, 2009.

(38)   Mishra, A.; Bäuerle, P. Small Molecule Organic Semiconductors on the Move: Promises for Future Solar Energy Technology. *Angewandte Chemie - International Edition* **2012**, *51* (9), 2020–2067. https://doi.org/10.1002/anie.201102326.

(39)   Russ, B.; Glaudell, A.; Urban, J. J.; Chabinyc, M. L.; Segalman, R. A. Organic Thermoelectric Materials for Energy Harvesting and Temperature Control. *Nature Reviews Materials* **2016**, *1* (10). https://doi.org/10.1038/natrevmats.2016.50.

(40)   Zhan, X.; Facchetti, A.; Barlow, S.; Marks, T. J.; Ratner, M. A.; Wasielewski, M. R.; Marder, S. R. Rylene and Related Diimides for Organic Electronics. *Advanced Materials* **2011**, *23* (2), 268–284. https://doi.org/10.1002/adma.201001402.

(41)   Würthner, F. Bay-Substituted Perylene Bisimides: Twisted Fluorophores for Supramolecular Chemistry. *Pure and Applied Chemistry* **2006**, *78* (12), 2341–2349. https://doi.org/10.1351/pac200678122341.

(42)   Weil, T.; Vosch, T.; Hofkens, J.; Peneva, K.; Müllen, K. The Rylene Colorant Family-Tailored Nanoemitters for Photonics Research and Applications. *Angewandte Chemie - International Edition* **2010**, *49* (48), 9068–9093. https://doi.org/10.1002/anie.200902532.

(43)   Wang, Q.; Li, Z.; Tao, D. D.; Zhang, Q.; Zhang, P.; Guo, D. P.; Jiang, Y. B. Supramolecular Aggregates as Sensory Ensembles. *Chemical Communications* **2016**, *52* (88), 12929–12939. https://doi.org/10.1039/c6cc06075g.

(44)   Zhan, X.; Facchetti, A.; Barlow, S.; Marks, T. J.; Ratner, M. A.; Wasielewski, M. R.; Marder, S. R. Rylene and Related Diimides for Organic Electronics. *Advanced Materials* **2011**, *23* (2), 268–284. https://doi.org/10.1002/adma.201001402.

(45)   Würthner, F.; Saha-möller, C. R.; Fimmel, B.; Ogi, S.; Leowanawat, P.; Schmidt, D. Perylene
         Bisimide Dye Assemblies as Archetype Functional Supramolecular Materials. *Chemical Reviews*
         2016, *116* (3), 962–1052. https://doi.org/10.1021/acs.chemrev.5b00188.

(46)   Weißenstein, A.; Saha-mçller, C. R.; Frank, W. Optical Sensing of Aromatic Amino Acids and
         Dipeptides by a Crown-Ether-Functionalized Perylene Bisimide Fluorophore. **2018**, 8009–8016.
         https://doi.org/10.1002/chem.201800870.

(47)   Ji, W.; Zhang, X.; Zhao, J.; Gao, Y.; Song, W.; Ozaki, Y. In Situ Formation of SERS Hot Spots by a Bis-
         Quaternized Perylene Dye : A Simple Strategy for Highly Sensitive Detection of Heparin over a
         Wide. *Analyst* **2018**, *143*, 1899–1905. https://doi.org/10.1039/c8an00015h.

(48)   Takada, T.; Ashida, A.; Nakamura, M.; Yamana, K. Cationic Perylenediimide as a Specific
         Fluorescent Binder to Mismatch Containing DNA. *Bioorganic & Medicinal Chemistry* **2013**, *21*
         (19), 6011–6014. https://doi.org/10.1016/j.bmc.2013.07.040.

(49)   Franceschin, M.; Pascucci, E.; Alvino, A.; Ambrosio, D. D.; Bianco, A.; Savino, M.; Sapienza, L.;
         Moro, P. A.; Chimica, D. New Highly Hydrosoluble and Not Self-Aggregated Perylene Derivatives
         with Three and Four Polar Side-Chains as G-Quadruplex Telomere Targeting Agents and
         Telomerase Inhibitors. *Bioorganic & Medicinal Chemistry Letters* **2007**, *17*, 2515–2522.
         https://doi.org/10.1016/j.bmcl.2007.02.021.

(50)   Bonchio, M.; Syrgiannis, Z.; Burian, M.; Marino, N.; Pizzolato, E.; Dirian, K.; Rigodanza, F.; Volpato,
         G. A.; la Ganga, G.; Demitri, N.; Berardi, S.; Amenitsch, H.; Guldi, D. M.; Caramori, S.; Bignozzi, C.
         A.; Sartorel, A.; Prato, M. Hierarchical Organization of Perylene Bisimides and Polyoxometalates
         for Photo-Assisted Water Oxidation. *Nature Chemistry* **2019**, *11* (2), 146–153.
         https://doi.org/10.1038/s41557-018-0172-y.

(51)   Echue, G.; Lloyd-jones, G. C.; Faul, C. F. J. Chiral Perylene Diimides: Building Blocks for Ionic Self-
         Assembly. *Chemistry A European Journal* **2015**, *21* (13), 5118–5128.
         https://doi.org/10.1002/chem.201406094.

(52)   Zhang, H.; Xue, L.; Han, J.; Fu, Y. Q.; Shen, Y.; Zhang, Z.; Li, Y.; Wang, M. New Generation
         Perovskite Solar Cells with Solution-Processed Amino-Substituted Perylene Diimide Derivative as
         Electron-Transport Layer. *Journal of Materials Chemistry A* **2016**, *4* (22), 8724–8733.
         https://doi.org/10.1039/c6ta03119f.

(53)   Hu, Z.; Xu, R.; Dong, S.; Lin, K.; Liu, J.; Huang, F.; Cao, Y. Quaternisation-Polymerized N-Type
         Polyelectrolytes: Synthesis, Characterisation and Application in High-Performance Polymer Solar
         Cells. *Materials Horizons* **2017**, *4* (1), 88–97. https://doi.org/10.1039/c6mh00434b.

(54)   Wu, G.; Zhang, Z.; Li, Y.; Gao, C.; Wang, X.; Chen, G. Exploring High-Performance N-Type
         Thermoelectric Composites Using Amino- Substituted Rylene Dimides and Carbon Nanotubes.
         ACS Nano **2017**, *11* (6), 5746–5752. https://doi.org/10.1021/acsnano.7b01279.

(55)   Huang, T.; Lu, D.; Ma, L.; Xi, X.; Liu, R.; Wu, D. A Hit-and-Run Strategy towards Perylene
         Diimide/Reduced Graphene Oxide as High Performance Sodium Ion Battery Cathode. *Chemical
         Engineering Journal* **2018**, *349*, 66–71. https://doi.org/10.1016/j.cej.2018.05.078.

(56)   Reilly, T. H.; Hains, A. W.; Chen, H. Y.; Gregg, B. A. A Self-Doping, O 2-Stable, n-Type Interfacial Layer for Organic Electronics. *Advanced Energy Materials* **2012**, *2* (4), 455–460. https://doi.org/10.1002/aenm.201100446.

(57)   Fink, R. F.; Seibt, J.; Engel, V.; Renz, M.; Kaupp, M.; Lochbrunner, S.; Zhao, H. M.; Pfister, J.; Würthner, F.; Engels, B. Exciton Trapping in π-Conjugated Materials: A Quantum-Chemistry-Based Protocol Applied to Perylene Bisimide Dye Aggregates. *Journal of the American Chemical Society* **2008**, *130* (39), 12858–12859. https://doi.org/10.1021/ja804331b.

(58)   Ford, W. E.; Kamat, P. v. Photochemistry of 3,4,9,10-Perylenetetracarboxylic Dianhydride Dyes. 3. Singlet and Triplet Excited-State Properties of the Bis(2,5-Di-Tert-Butylphenyl)Imide Derivative. *Journal of Physical Chemistry* **1987**, *91*, 67–56. https://doi.org/https://doi.org/10.1021/j100309a012.

(59)   Ronconi, F.; Syrgiannis, Z.; Bonasera, A.; Prato, M.; Argazzi, R.; Caramori, S.; Cristino, V.; Bignozzi, C. A. Modification of Nanocrystalline WO3 with a Dicationic Perylene Bisimide: Applications to Molecular Level Solar Water Splitting. *Journal of the American Chemical Society* **2015**, *137* (14), 4630–4633. https://doi.org/10.1021/jacs.5b01519.

(60)   Würthner, F. Perylene Bisimide Dyes as Versatile Building Blocks for Functional Supramolecular Architectures. *Chemical Communications* **2004**, 1564–1579. https://doi.org/https://doi.org/10.1039/B401630K.

(61)   Mizuguchi, J.; Tojo, K. Electronic Structure of Perylene Pigments as Viewed from the Crystal Structure and Excitonic Interactions. *Journal of Physical Chemistry B* **2002**, *106* (4), 767–772. https://doi.org/10.1021/jp012909p.

(62)   Brown, K. E.; Salamant, W. A.; Shoer, L. E.; Young, R. M.; Wasielewski, M. R. Direct Observation of Ultrafast Excimer Formation in Covalent Perylenediimide Dimers Using Near-Infrared Transient Absorption Spectroscopy. *Journal of Physical Chemistry Letters* **2014**, *5* (15), 2588–2593. https://doi.org/10.1021/jz5011797.

(63)   Langhals, H. Cyclic Carboxylic Imide Structures as Structure Elements of High Stability. Novel Developments in Perylene Dye Chemistry. *Hetercycles* **1995**, *40* (1), 477.

(64)   Supur, M.; Fukuzumi, S. Tuning the Photodriven Electron Transport within the Columnar Perylenediimide Stacks by Changing the π-Extent of the Electron Donors. *Physical Chemistry Chemical Physics* **2013**, *15* (7), 2539–2546. https://doi.org/10.1039/c2cp44106c.

(65)   Tilley, A. J.; Pensack, R. D.; Lee, T. S.; Djukic, B.; Scholes, G. D.; Seferos, D. S. Ultrafast Triplet Formation in Thionated Perylene Diimides. *Journal of Physical Chemistry C* **2014**, *118* (19), 9996–10004. https://doi.org/10.1021/jp503708d.

(66)   Ryan, T. J.; Young, R. M.; Henkelis, J. J.; Hafezi, N.; Vermeulen, N. A.; Hennig, A.; Dale, E. J.; Wu, Y.; Krzyaniak, M. D.; Fox, A.; Nau, W. M.; Wasielewski, M. R.; Stoddart, J. F.; Scherman, O. A. Energy and Electron Transfer Dynamics within a Series of Perylene Diimide/Cyclophane Systems. *Journal of the American Chemical Society* **2015**, *137* (48), 15299–15307. https://doi.org/10.1021/jacs.5b10329.

(67)   Nguyen, V.; Qi, S.; Kim, S.; Kwon, N.; Kim, G.; Yim, Y.; Park, S.; Yoon, J. An Emerging Molecular Design Approach to Heavy-Atom-Free Photosensitizers for Enhanced Photodynamic Therapy under Hypoxia. *Journal of the American Chemical Society* **2019**, *141*, 16243–16248. https://doi.org/10.1021/jacs.9b09220.

(68)   Tilley, A. J.; Guo, C.; Miltenburg, M. B.; Schon, T. B.; Yan, H.; Li, Y.; Seferos, D. S. Thionation Enhances the Electron Mobility of Perylene Diimide for High Performance N-Channel Organic Field Effect Transistors. *Advanced Functional Materials* **2015**, *25* (22), 3321–3329. https://doi.org/10.1002/adfm.201500837.

(69)   la Porte, N. T.; Martinez, J. F.; Hedström, S.; Rudshteyn, B.; Phelan, B. T.; Mauck, C. M.; Young, R. M.; Batista, V. S.; Wasielewski, M. R. Photoinduced Electron Transfer from Rylenediimide Radical Anions and Dianions to Re(Bpy)(CO)3 Using Red and near-Infrared Light. *Chemical Science* **2017**, *8* (5), 3821–3831. https://doi.org/10.1039/c6sc05103k.

(70)   Gosztola, D.; Niemczyk, M. P.; Svec, W.; Lukas, A. S.; Wasielewski, M. R. Excited Doublet States of Electrochemically Generated Aromatic Imide and Diimide Radical Anions. *Journal of Physical Chemistry A* **2000**, *104* (28), 6545–6551. https://doi.org/10.1021/jp000706f.

(71)   Segalina, A.; Assfeld, X.; Monari, A.; Pastore, M. Computational Modeling of Exciton Localization in Self-Assembled Perylene Helices: Effects of Thermal Motion and Aggregate Size. *Journal of Physical Chemistry C* **2019**, *123* (11), 6427–6437. https://doi.org/10.1021/acs.jpcc.9b00494.

(72)   Kasha, M. Energy Transfer Mechanisms and the Molecular Exciton Model for Molecular Aggregates. *Radiation Research* **1963**, *20* (1), 55–70. https://doi.org/https://doi.org/10.2307/3571331.

(73)   Kasha, M. Relation between Exciton Bands and Conduction Bands in Molecular Lamellar Systems. *Reviews of Modern Physics* **1959**, *31*, 162–169. https://doi.org/10.1103/RevModPhys.31.162.

(74)   Kazmaier, P. M.; Hoffmann, R. A Theoretical Study of Crystallochromy. Quantum Interference Effects in the Spectra of Perylene Pigments. *Journal of the American Chemical Society* **1994**, *116* (21), 9684–9691. https://doi.org/10.1021/ja00100a038.

(75)   Hestand, N. J.; Spano, F. C. Expanded Theory of H- and J - Molecular Aggregates: The Effects of Vibronic Coupling and Intermolecular Charge Transfer. *Chemical Reviews* **2018**, *118* (15), 7069–7163. https://doi.org/10.1021/acs.chemrev.7b00581.

(76)   Hestand, N. J.; Spano, F. C. Molecular Aggregate Photophysics beyond the Kasha Model: Novel Design Principles for Organic Materials. *Accounts of Chemical Research* **2017**, *50* (2), 341–350. https://doi.org/10.1021/acs.accounts.6b00576.

(77)   Burian, M.; Rigodanza, F.; Amenitsch, H.; Almásy, L.; Khalakhan, I.; Syrgiannis, Z.; Prato, M. Structural and Optical Properties of a Perylene Bisimide in Aqueous Media. *Chemical Physics Letters* **2017**, *683*, 454–458. https://doi.org/10.1016/j.cplett.2017.03.056.

(78)   Bag, K.; Halder, R.; Jana, B.; Malik, S. Solvent-Assisted Enhanced Emission of Cationic Perylene Diimide Supramolecular Assembly in Water: A Perspective from Experiment and Simulation.

Journal of Physical Chemistry C **2019**, *123* (10), 6241–6249.
https://doi.org/10.1021/acs.jpcc.8b11054.

(79)   Lasitha, P.; Prasad, E. Host – Guest Chemistry between Perylene Diimide (PDI) Derivatives and 18-
Crown-6: Enhancement in Luminescence Quantum Yield and Electrical Conductivity. *Chemistry A
European Journal* **2016**, *22*, 10558–10564. https://doi.org/10.1002/chem.201600709.

(80)   Hoffmann, M.; Schmidt, K.; Fritz, T.; Hasche, T.; Agranovich, V. M.; Leo, K. The Lowest Energy
Frenkel and Charge-Transfer Excitons in Quasi-One-Dimensional Structures: Application to
MePTCDI and PTCDA Crystals. *Chemical Physics* **2000**, *258*, 73–96.
https://doi.org/10.1016/S0301-0104(00)00157-9.

(81)   Li, J.; Zhou, H.; Zhang, Y.; Shahzad, S. A.; Yang, M.; Hu, Z.; Yu, C. Tuning of the Perylene Probe
Excimer Emission with Silver Nanoparticles. *Analytica Chimica Acta* **2018**, *1016*, 40–48.
https://doi.org/10.1016/j.aca.2018.02.014.

(82)   Russ, B.; Robb, M. J.; Brunetti, F. G.; Miller, P. L.; Perry, E. E.; Patel, S. N.; Ho, V.; Chang, W. B.;
Urban, J. J.; Chabinyc, M. L.; Hawker, C. J.; Segalman, R. A. Power Factor Enhancement in
Solution-Processed Organic n-Type Thermoelectrics through Molecular Design. *Advanced
Materials* **2014**, *26* (21), 3473–3477. https://doi.org/10.1002/adma.201306116.

(83)   Gregg, B. A.; Chen, S. G.; Cormier, R. A. Coulomb Forces and Doping in Organic Semiconductors.
Chemistry of Materials **2004**, *16* (23), 4586–4599. https://doi.org/10.1021/cm049625c.

(84)   Chen, S. G.; Branz, H. M.; Eaton, S. S.; Taylor, P. C.; Cormier, R. A.; Gregg, B. A. Substitutional N-
Type Doping of an Organic Semiconductor Investigated by Electron Paramagnetic Resonance
Spectroscopy. *Journal of Physical Chemistry B* **2004**, *108* (45), 17329–17336.
https://doi.org/10.1021/jp049628c.

(85)   Gregg, B. A.; Chen, S. G.; Branz, H. M. On the Superlinear Increase in Conductivity with Dopant
Concentration in Excitonic Semiconductors. *Applied Physics Letters* **2004**, *84* (10), 1707–1709.
https://doi.org/10.1063/1.1668326.

(86)   Gregg, B. A.; Cormier, R. A. Doping Molecular Semiconductors: N-Type Doping of a Liquid Crystal
Perylene Diimide. *Journal of the American Chemical Society* **2001**, *123* (32), 7959–7960.
https://doi.org/10.1021/ja016410k.

(87)   Supur, M.; Sung, Y. M.; Kim, D.; Fukuzumi, S. Enhancement of Photodriven Charge Separation by
Conformational and Intermolecular Adaptations of an Anthracene−Perylenediimide−Anthracene
Triad to an Aqueous Environment. *Journal of Physical Chemistry C* **2013**, *117*, 12438–12445.
https://doi.org/10.1021/jp403285k.

(88)   El-Refaey, A.; Shaban, S. Y.; El-Kemary, M.; El-Khouly, M. E. Spectroscopic and Thermodynamic
Studies of Light Harvesting Perylenediimide Derivative - Zinc Porphyrin Complex in Aqueous
Media. *Spectrochimica Acta - Part A: Molecular and Biomolecular Spectroscopy* **2017**, *186*, 132–
139. https://doi.org/10.1016/j.saa.2017.06.016.

(89)   Weißenstein, A.; Saha-Möller, C. R.; Würthner, F. Optical Sensing of Aromatic Amino Acids and Dipeptides by a Crown-Ether-Functionalized Perylene Bisimide Fluorophore. *Chemistry - A European Journal* **2018**, *24* (31), 8009–8016. https://doi.org/10.1002/chem.201800870.

(90)   Che, Y.; Yang, X.; Liu, G.; Yu, C.; Ji, H.; Zuo, J.; Zhao, J.; Zang, L. Ultrathin N-Type Organic Nanoribbons with High Photoconductivity and Application in Optoelectronic Vapor Sensing of Explosives. *Journal of the American Chemical Society* **2010**, *132* (16), 5743–5750. https://doi.org/10.1021/ja909797q.

(91)   Hariharan, P. S.; Pitchaimani, J.; Madhu, V.; Anthony, S. P. Perylene Diimide Based Fluorescent Dyes for Selective Sensing of Nitroaromatic Compounds: Selective Sensing in Aqueous Medium Across Wide PH Range. *Journal of Fluorescence* **2016**, *26* (2), 395–401. https://doi.org/10.1007/s10895-015-1725-8.

(92)   Yongwei, H.; Baogang, Q.; Zhixiang, W.; Guangtong, L.; Lianfeng, S. Self-Assembled Organic Functional Nanotubes and Nanorods and Their Sensory Properties. *Journal of Physical Chemistry C* **2009**, *113* (10), 3929–3933. https://doi.org/10.1021/jp8078452.

(93)   Tenori, E.; Colusso, A.; Syrgiannis, Z.; Bonasera, A.; Osella, S.; Ostric, A.; Lazzaroni, R.; Meneghetti, M.; Prato, M. Perylene Derivatives As Useful SERRS Reporters, Including Multiplexing Analysis. *ACS Applied Materials and Interfaces* **2015**, *7* (51), 28042–28048. https://doi.org/10.1021/acsami.5b03586.

(94)   Huang, Y.; Liu, X.; Wang, Q.; Fu, J.; Zhao, L.; Liu, Z.; Jin, D. Highly Responsive Ethylenediamine Vapor Sensor Based on a Perylenediimide-Camphorsulfonic Acid Complex: Via Ionic Self-Assembly. *Journal of Materials Chemistry C* **2017**, *5* (30), 7644–7651. https://doi.org/10.1039/c7tc02580g.

(95)   Pramanik, B.; Mondal, J. H.; Singha, N.; Ahmed, S.; Mohanty, J.; Das, D. A Viologen–Perylenediimide Conjugate as an Efficient Base Sensor with Solvatochromic Property. *ChemPhysChem* **2017**, *18* (2), 245–252. https://doi.org/10.1002/cphc.201601053.

(96)   Roy, B.; Noguchi, T.; Yoshihara, D.; Yamamoto, T.; Sakamoto, J.; Shinkai, S. Amplified Fluorescence Emission of Bolaamphiphilic Perylene-Azacrown Ether Derivatives Directed towards Molecular Recognition Events. *Physical Chemistry Chemical Physics* **2016**, *18* (19), 13239–13245. https://doi.org/10.1039/c6cp01545j.

(97)   Ma, L.; Gao, W.; Han, X.; Qu, F.; Xia, L.; Kong, R. M. A Label-Free and Fluorescence Turn-on Assay for Sensitive Detection of Hyaluronidase Based on Hyaluronan-Induced Perylene Self-Assembly. *New Journal of Chemistry* **2019**, *43* (8), 3383–3389. https://doi.org/10.1039/C8NJ06343E.

(98)   Wang, B.; Zhu, Q.; Liao, D.; Yu, C. Perylene Probe Induced Gold Nanoparticle Aggregation. *Journal of Materials Chemistry* **2011**, *21* (13), 4821–4826. https://doi.org/10.1039/c0jm04527f.

(99)   Zang, L.; Liu, R.; Holman, M. W.; Nguyen, K. T.; Adams, D. M. A Single-Molecule Probe Based on Intramolecular Electron Transfer. *Journal of the American Chemical Society* **2002**, *124* (36), 10640–10641. https://doi.org/10.1021/ja0268074.

(100) Mohr, G. J.; Spichiger, U. E.; Jona, W.; Langhals, H. Using N-Aminoperylene-3,4:9,10-Tetracarboxylbisimide as a Fluorogenic Reactand in the Optical Sensing of Aqueous Propionaldehyde. *Analytical Chemistry* **2000**, *72* (5), 1084–1087. https://doi.org/10.1021/ac991171t.

(101) Wu, N.; Wang, C.; Bunes, B. R.; Zhang, Y.; Slattum, P. M.; Yang, X.; Zang, L. Chemical Self-Doping of Organic Nanoribbons for High Conductivity and Potential Application as Chemiresistive Sensor. *ACS Applied Materials and Interfaces* **2016**, *8* (19), 12360–12368. https://doi.org/10.1021/acsami.6b03151.

(102) Rodríguez-Abreu, C.; Aubery-Torres, C.; Solans, C.; López-Quintela, A.; Tiddy, G. J. T. Characterization of Perylene Diimide Dye Self-Assemblies and Their Use as Templates for the Synthesis of Hybrid and Supermicroporous Nanotubules. *ACS Applied Materials and Interfaces* **2011**, *3* (10), 4133–4141. https://doi.org/10.1021/am201016m.

(103) Panzarasa, G.; Torzynski, A. L.; Sai, T.; Smith-Mannschott, K.; Dufresne, E. R. Transient Supramolecular Assembly of a Functional Perylene Diimide Controlled by a Programmable PH Cycle. *Soft Matter* **2020**, *16* (3), 591–594. https://doi.org/10.1039/c9sm02026h.

(104) Rodríguez-Abreu, C.; Aubery-Torres, C.; Solans, C.; López-Quintela, A.; Tiddy, G. J. T. Characterization of Perylene Diimide Dye Self-Assemblies and Their Use as Templates for the Synthesis of Hybrid and Supermicroporous Nanotubules. *ACS Applied Materials and Interfaces* **2011**, *3* (10), 4133–4141. https://doi.org/10.1021/am201016m.

(105) Everett, T. A.; Higgins, D. A. Electrostatic Self-Assembly of Ordered Perylene-Diimide/Polyelectrolyte Nanofibers in Fluidic Devices: From Nematic Domains to Macroscopic Alignment. *Langmuir* **2009**, *25* (22), 13045–13051. https://doi.org/10.1021/la9019298.

(106) Supur, M.; Fukuzumi, S. Photodriven Electron Transport within the Columnar Perylenediimide Nanostructures Self-Assembled with Sulfonated Porphyrins in Water. *Journal of Physical Chemistry C* **2012**, *116* (44), 23274–23282. https://doi.org/10.1021/jp308549w.

(107) Weißenstein, A.; Würthner, F. Metal Ion Templated Self-Assembly of Crown Ether Functionalized Perylene Bisimide Dyes. *Chemical Communications* **2015**, *51* (16), 3415–3418. https://doi.org/10.1039/c4cc09443c.

(108) Guan, Y.; Yu, S. H.; Antonietti, M.; Böttcher, C.; Faul, C. F. J. Synthesis of Supramolecular Polymers by Ionic Self-Assembly of Oppositely Charged Dyes. *Chemistry - A European Journal* **2005**, *11* (4), 1305–1311. https://doi.org/10.1002/chem.200400778.

(109) Rodriguez-Abreu, C.; Vilanova, N.; Solans, C.; Ujihara, M.; Imae, T.; López-Quintela, A.; Motojima, S. A Combination of Hard and Soft Templating for the Fabrication of Silica Hollow Microcoils with Nanostructured Walls. *Nanoscale Research Letters* **2011**, *6* (1). https://doi.org/10.1186/1556-276X-6-330.

(110) Weitzel, C. R.; Everett, T. A.; Higgins, D. A. Aggregation and Its Influence on Macroscopic In-Plane Organization in Thin Films of Electrostatically Self-Assembled Perylene-Diimide/Polyelectrolyte Nanofibers. *Langmuir* **2009**, *25* (2), 1188–1195. https://doi.org/10.1021/la803177n.

(111) Tang, X.; Yang, Y.; Kang, Y.; Wu, H.; Xu, J. F.; Wang, Z. Efficient Fenton Degradation of Perylene Diimide Dye Promoted by a Catalytic Amount of Cucurbit[8]Uril. *Langmuir* **2020**, *36* (21), 5954–5959. https://doi.org/10.1021/acs.langmuir.0c00806.

(112) Görl, D.; Zhang, X.; Würthner, F. Molecular Assemblies of Perylene Bisimide Dyes in Water. *Angewandte Chemie* **2012**, *51* (26), 6328–6348. https://doi.org/10.1002/anie.201108690.

(113) Boiko, O. P.; Ya, B.; Yu, O.; Slominskiy, Y. L.; Tsybulia, S. A.; Nastishin, Y. A.; Nazarenko, V. G. Electronic Energy Levels in Lyotropic Chromonic Liquid Crystals Formed by Ionic Perylene Diimide Derivatives. *Synthetic Metals* **2019**, *257*, 116147. https://doi.org/10.1016/j.synthmet.2019.116147.

(114) Zakrevskyy, Y.; Faul, C. F. J.; Guan, Y.; Stumpe, J. Alignment of a Perylene-Based Ionic Self-Assembly Complex in Thermotropic and Lyotropic Liquid-Crystalline Phases. *Advanced Functional Materials* **2004**, *14* (9), 835–841. https://doi.org/10.1002/adfm.200305194.

(115) Iverson, I. K.; Casey, S. M.; Seo, W.; Tam-Chang, S. W.; Pindzola, B. A. Controlling Molecular Orientation in Solid Films via Self-Organization in the Liquid-Crystalline Phase. *Langmuir* **2002**, *18* (9), 3510–3516. https://doi.org/10.1021/la011499t.

(116) Laiho, A.; Smarsly, B. M.; Faul, C. F. J.; Ikkala, O. Macroscopically Aligned Ionic Self-Assembled Perylene-Surfactant Complexes within a Polymer Matrix. *Advanced Functional Materials* **2008**, *18* (13), 1890–1897. https://doi.org/10.1002/adfm.200701496.

(117) Tam-Chang, S. W.; Iverson, I. K.; Helbley, J. Study of the Chromonic Liquid-Crystalline Phases of Bis-(N,N-Diethylaminoethyl)Perylene-3,4,9,10-Tetracarboxylic Diimide Dihydrochloride by Polarized Optical Microscopy and 2H NMR Spectroscopy. *Langmuir* **2004**, *20* (2), 342–347. https://doi.org/10.1021/la030256t.

(118) Tam-Chang, S. W.; Helbley, J.; Iverson, I. K. A Study of the Structural Effects on the Liquid-Crystalline Properties of Ionic Perylenebis(Dicarboximide)s Using UV-Vis Spectroscopy, Polarized Light Microscopy, and NMR Spectroscopy. *Langmuir* **2008**, *24* (5), 2133–2139. https://doi.org/10.1021/la7027324.

(119) Shin, S.; Chang, E.; Lee, S.; Ku, J.; Jeong, K. Color-Tunable Anisotropic Optical Films Fabricated Using Perylene Diimide Mixed with Naphthalene Benzimidazole. *Thin Solid Films* **2011**, *520* (1), 486–490. https://doi.org/10.1016/j.tsf.2011.06.105.

(120) Guan, Y.; Zakrevskyy, Y.; Stumpe, J.; Faul, C. F. J. Perylenediimide-Surfactant Complexes: Thermotropic Liquid-Crystalline Materials via Ionic Self-Assembly. *Chemical Communications* **2003**, *1*, 894–895. https://doi.org/10.1039/B211753C.

(121) Soroka, P. v.; Vakhnin, A. Y.; Skryshevskiy, Y. A.; Boiko, O. P.; Anisimov, M. I.; Slominskiy, Y. L.; Nazarenko, V. G.; Genoe, J.; Kadashchuk, A. Charge Carrier Trapping in Highly-Ordered Lyotropic Chromonic Liquid Crystal Films Based on Ionic Perylene Diimide Derivatives. *EPJ Applied Physics* **2014**, *68* (3), 1–9. https://doi.org/10.1051/epjap/2014140272.

(122) Kim, H. J.; Jung, W.; Jeong, H. S.; Jung, H. Fabrication of a High-Performance Thin Film Polarizer Using Lyotropic Chromonic Liquid Crystals Using a High-Resolution Nanoscale Template. *Journal of Materials Chemistry C* **2017**, *5*, 12241–12248. https://doi.org/10.1039/c7tc03974c.

(123) Ghosh, I.; Ghosh, T.; Bardagi, J. I.; König, B. Reduction of Aryl Halides by Consecutive Visible Light-Induced Electron Transfer Process. *Science* **2014**, *346* (6210), 725–728. https://doi.org/10.1126/science.1258232.

(124) Matsunaga, Y.; Goto, K.; Kubono, K.; Sako, K.; Shinmyozu, T. Photoinduced Color Change and Photomechanical Effect of Naphthalene Diimides Bearing Alkylamine Moieties in the Solid State. *Chemistry - A European Journal* **2014**, *20* (24), 7309–7316. https://doi.org/10.1002/chem.201304849.

(125) Giaimo, J. M.; Gusev, A. v.; Wasielewski, M. R. Excited-State Symmetry Breaking in Cofacial and Linear Dimers of a Green Perylenediimide Chlorophyll Analogue Leading to Ultrafast Charge Separation. *Journal of the American Chemical Society* **2002**, *124* (29), 8530–8531. https://doi.org/10.1021/ja026422l.

(126) Anthopoulos, T. D.; Anyfantis, G. C.; Papavassiliou, G. C.; de Leeuw, D. M. Air-Stable Ambipolar Organic Transistors. *Applied Physics Letters* **2007**, *90* (12). https://doi.org/10.1063/1.2715028.

(127) Goodson, F. S.; Panda, D. K.; Ray, S.; Mitra, A.; Guha, S.; Saha, S. Tunable Electronic Interactions between Anions and Perylenediimide. *Organic and Biomolecular Chemistry* **2013**, *11* (29), 4797–4803. https://doi.org/10.1039/c3ob40703a.

(128) Russ, B.; Robb, M. J.; Popere, B. C.; Perry, E. E.; Mai, C.-K.; Fronk, S. L.; Patel, S. N.; Mates, T. E.; Bazan, G. C.; Urban, J. J.; Chabinyc, M. L.; Hawker, C. J.; Segalman, R. A. Tethered Tertiary Amines as Solid-State n-Type Dopants for Solution-Processable Organic Semiconductors. *Chemical Science* **2016**, *7* (3), 1914–1919. https://doi.org/10.1039/C5SC04217H.

(129) Wang, Z.; Zheng, N.; Zhang, W.; Yan, H.; Xie, Z.; Ma, Y.; Huang, F.; Cao, Y. Self-Doped, n-Type Perylene Diimide Derivatives as Electron Transporting Layers for High-Efficiency Polymer Solar Cells. *Advanced Energy Materials* **2017**, *7* (15), 1–7. https://doi.org/10.1002/aenm.201700232.

(130) Lukas, A. S.; Zhao, Y.; Miller, S. E.; Wasielewski, M. R. Biomimetic Electron Transfer Using Low Energy Excited States: A Green Perylene-Based Analogue of Chlorophyll a. *Journal of Physical Chemistry B* **2002**, *106* (6), 1299–1306. https://doi.org/10.1021/jp014073w.

(131) Liu, H.; Yin, G.; Li, Q.; Liu, G.; Pu, S.; Zhang, H. Visible-Light-Triggered Generation of Persistent Radical Anions from Perylenediimides: A Substituent Effect and Potential Application in Photocatalytic Reduction of Ag +. *Dyes and Pigments* **2019**, *165*, 319–326. https://doi.org/10.1016/j.dyepig.2019.02.033.

(132) Rybtchinski, B.; Sinks, L. E.; Wasielewski, M. R. Photoinduced Electron Transfer in Self-Assembled Dimers of 3-Fold Symmetric Donor-Acceptor Molecules Based on Perylene-3,4:9,10-Bis(Dicarboximide). *Journal of Physcial Chemistry A* **2004**, 7497–7505. https://doi.org/10.1021/jp048883u.

(133) Zhao, Y.; Wasielewski, M. R. 3,4:9,10-Perylenebis(Dicarboximide) Chromophores That Function as Both Electron Donors and Acceptors. *Tetrahedron Letters* **1999**, *40* (39), 7047–7050. https://doi.org/10.1016/S0040-4039(99)01468-9.

(134) Langhals, H.; Blanke, P. An Approach to Novel NIR Dyes Utilising α-Effect Donor Groups. *Dyes and Pigments* **2003**, *59* (2), 109–116. https://doi.org/10.1016/S0143-7208(03)00083-4.

(135) Bureš, F. Fundamental Aspects of Property Tuning in Push-Pull Molecules. *RSC Advances* **2014**, *4* (102), 58826–58851. https://doi.org/10.1039/c4ra11264d.

(136) Ahrens, M. J.; Tauber, M. J.; Wasielewski, M. R. Bis(n-Octylamino)Perylene-3,4:9,10-Bis(Dicarboximide)s and Their Radical Cations: Synthesis, Electrochemistry, and ENDOR Spectroscopy. *Journal of Organic Chemistry* **2006**, *71* (5), 2107–2114. https://doi.org/10.1021/jo052394o.

(137) Wu, H.; Wang, H.; Xue, L.; Shi, Y.; Li, X. Hindered Intramolecular Electron Transfer in Room-Temperature Ionic Liquid. *J. Phys. Chem. B.* **2010**, 14420–14425. https://doi.org/10.1021/jp101240a.

(138) van Haver, P.; Helsen, N.; Depaemelaere, S.; van der Auweraer, M.; de Schryver, F. C. The Influence of Solvent Polarity on the Nonradiative Decay of Exciplexes. *Journal of the American Chemical Society* **1991**, *113*, 6849–6857. https://doi.org/10.1021/ja00018a021.

(139) Swinnen, A. M.; van der Auweraer, M.; de Schryver, F. C.; Nakatani, K.; Okada, T.; Malaga, N. Photophysics of the Intramolecular Exciplex Formation in ω-(1-Pyrenyl)-α-N,N-Dimethylaminoalkanes. *Journal of the American Chemical Society* **1987**, *109*, 321–330. https://doi.org/10.1021/ja00236a005.

(140) Hussain, E.; Zhou, H.; Yang, N.; Anjum, S.; Yu, C. Dyes and Pigments Synthesis of Regioisomerically Pure Piperidine Substituted Perylenebisimide NIR Dyes : A Comparative Study of Spectroscopic , Electrochemical and Crystalline Properties. *Dyes and Pigments* **2017**, *147*, 211–224. https://doi.org/10.1016/j.dyepig.2017.08.002.

(141) Ozser, M. E.; Sarkodie, S. A.; Mohiuddin, O.; Ozesme, G. Novel Derivatives of Regioisomerically Pure 1,7-Disubstituted Perylene Diimide Dyes Bearing Phenoxy and Pyrrolidinyl Substituents : Synthesis, Photophysical, Thermal, and Structural Properties. *Journal of Luminescence* **2017**, *192*, 414–423. https://doi.org/10.1016/j.jlumin.2017.07.019.

(142) Scaccabarozzi, A. D.; Basu, A.; Aniés, F.; Liu, J.; Zapata-Arteaga, O.; Warren, R.; Firdaus, Y.; Nugraha, M. I.; Lin, Y.; Campoy-Quiles, M.; Koch, N.; Müller, C.; Tsetseris, L.; Heeney, M.; Anthopoulos, T. D. Doping Approaches for Organic Semiconductors. *Chemical Reviews* **2021**, acs.chemrev.1c00581. https://doi.org/10.1021/acs.chemrev.1c00581.

(143) Song, Y.; Zhang, W.; He, S.; Shang, L.; Ma, R.; Jia, L.; Wang, H. Perylene Diimide and Luminol as Potential-Resolved Electrochemiluminescence Nanoprobes for Dual Targets Immunoassay at Low Potential. *ACS Applied Materials and Interfaces* **2019**, *11* (37), 33676–33683. https://doi.org/10.1021/acsami.9b11416.

(144) Online, V. A.; Zhan, L.; Liang, L. J.; Zhen, S. J.; Li, C. M.; Huang, C. Z. Aptamer-Based Spectro Fl Uorometry for Cellular Prion. **2013**, 825–830. https://doi.org/10.1039/c2an36322d.

(145) Maltas, E.; Malkondu, S.; Uyar, P.; Ozmen, M. Fluorescent Labelling of DNA on Superparamagnetic Nanoparticles by a Perylene Bisimide Derivative for Cell Imaging. *Materials Science & Engineering C* **2015**, *48*, 86–93. https://doi.org/10.1016/j.msec.2014.11.057.

(146) D'Ambrosio, D.; Reichenbach, P.; Micheli, E.; Alvino, A.; Franceschin, M.; Savino, M.; Lingner, J. Specific Binding of Telomeric G-Quadruplexes by Hydrosoluble Perylene Derivatives Inhibits Repeat Addition Processivity of Human Telomerase. *Biochimie* **2012**, *94* (3), 854–863. https://doi.org/10.1016/j.biochi.2011.12.004.

(147) Alvino, A.; Franceschin, M.; Cefaro, C.; Borioni, S.; Biomolecolare, C. Synthesis and Spectroscopic Properties of Highly Water-Soluble Perylene Derivatives. *Tetrahedron* **2007**, *63*, 7858–7865. https://doi.org/10.1016/j.tet.2007.05.096.

(148) Liu, Y.; Gao, X.; Lu, F.; Hu, M.; Shi, L.; Zheng, L. Reversible Helical Chirality of Perylene Bisimide Aggregates: Amino Acid-Directed Chiral Transfer and Chiral Inversion. *Soft Matter* **2017**, *13*, 3072–3075. https://doi.org/10.1039/c7sm00414a.

(149) Zhao, H.; Hussain, S.; Liu, X.; Li, S.; Lv, F.; Liu, L. Design of an Amphiphilic Perylene Diimide for Optical Recognition of Anticancer Drug through a Chirality-Induced Helical Structure. *Chemistry A European Journal* **2019**, *100049*, 9834–9839. https://doi.org/10.1002/chem.201901948.

(150) Echue, G.; Hamley, I.; Jones, G. C. L.; Faul, C. F. J. Chiral Perylene Materials by Ionic Self-Assembly. *Langmuir* **2016**, *32* (35), 9023–9032. https://doi.org/10.1021/acs.langmuir.6b02201.

(151) Gershberg, J.; Radić Stojković, M.; Škugor, M.; Tomić, S.; Rehm, T. H.; Rehm, S.; Saha-Möller, C. R.; Piantanida, I.; Würthner, F. Sensing of Double-Stranded DNA/RNA Secondary Structures by Water Soluble Homochiral Perylene Bisimide Dyes. *Chemistry - A European Journal* **2015**, *21* (21), 7886–7895. https://doi.org/10.1002/chem.201500184.

(152) Han, D.; Han, J.; Huo, S.; Qu, Z.; Jiao, T.; Liu, M.; Duan, P. Proton Triggered Circularly Polarized Luminescence in Orthogonal- and Co-Assemblies of Chiral Gelators with Achiral Perylene Bisimide. *Chemical Communications* **2018**, *54* (44), 5630–5633. https://doi.org/10.1039/c8cc02777c.

(153) Huang, Y.; Yan, Y.; Smarsly, B. M.; Wei, Z.; Faul, C. F. J. Helical Supramolecular Aggregates, Mesoscopic Organisation and Nanofibers of a Perylenebisimide-Chiral Surfactant Complex via Ionic Self-Assembly. *Journal of Materials Chemistry* **2009**, *19* (16), 2356–2362. https://doi.org/10.1039/b817838k.

(154) Lv, Z.; Liu, J.; Bai, W.; Yang, S.; Chen, A. Biosensors and Bioelectronics Short Communication A Simple and Sensitive Label-Free Fl Uorescent Approach for Protein Detection Based on a Perylene Probe and Aptamer. *Biosensors and Bioelectronic* **2015**, *64*, 530–534. https://doi.org/10.1016/j.bios.2014.09.095.

(155) Wang, B.; Yu, C. Fluorescence Turn-On Detection of a Protein through the Reduced Aggregation of a Perylene Probe. *Angewandte Chemie International Edition* **2010**, *49*, 1485–1488. https://doi.org/10.1002/anie.200905237.

(156) Wang, B.; Jiao, H.; Li, W.; Liao, D. Superquencher Formation Vianucleic Acid Induced Noncovalent Perylene Probe Self-Assembly. *Chemical Communications* **2011**, *47*, 10269–10271. https://doi.org/10.1039/c1cc13606b.

(157) Liao, D.; Li, W.; Chen, J.; Jiao, H.; Zhou, H. Analytica Chimica Acta Sensing of a Nucleic Acid Binding Protein via a Label-Free Perylene Probe Fluorescence Recovery Assay. *Analytica Chimica Acta* **2013**, *797*, 89–94. https://doi.org/10.1016/j.aca.2013.08.022.

(158) Hu, R.; Liu, T.; Zhang, X.; Huan, S.; Wu, C.; Fu, T.; Tan, W. Multicolor Fluorescent Biosensor for Multiplexed Detection of DNA. *Analytical Chemistry* **2014**, *86* (10), 5009–5016. https://doi.org/10.1021/ac500618v.

(159) Bettini, S.; Syrgiannis, Z.; Pagano, R.; Luka, D.; Salvatore, L.; Prato, M.; Giancane, G.; Valli, L. Perylene Bisimide Aggregates as Probes for Subnanomolar Discrimination of Aromatic Biogenic Amines. *ACS Applied Materials and Interfaces* **2019**, *11* (18), 17079–17089. https://doi.org/10.1021/acsami.9b04101.

(160) Wu, X.; Chen, X.; Song, B.; Huang, Y.; Li, Z.; Chen, Z. Induced Helical Chirality of Perylenebisimide Aggregates Allows for Enantiopurity Determination and Differentiation of a -Hydroxy Carboxylates by Using Circular Dichroism. **2014**, 11793–11799. https://doi.org/10.1002/chem.201402627.

(161) Dai, X.; Li, Q.; Aldalbahi, A.; Wang, L.; Fan, C.; Liu, X. DNA-Based Fabrication for Nanoelectronics. *Nano Letters* **2020**, *20* (8), 5604–5615. https://doi.org/10.1021/acs.nanolett.0c02511.

(162) Liang, L.; Fu, Y.; Wang, D.; Wei, Y.; Kobayashi, N.; Minari, T. DNA as Functional Material in Organic-Based Electronics. *Applied Sciences (Switzerland)* **2018**, *8* (1). https://doi.org/10.3390/app8010090.

(163) Fink, H.-W.; Schoenenberger, C. Electrical Conduction through DNA Molecules. *Nature* **1999**, *398*, 407–410. https://doi.org/https://doi.org/10.1038/18855.

(164) Carmieli, R.; Zeidan, T. A.; Kelley, R. F.; Mi, Q.; Lewis, F. D.; Wasielewski, M. R. Excited State, Charge Transfer, and Spin Dynamics in DNA Hairpin Conjugates with Perylenediimide Hairpin Linkers. *Journal of Physical Chemistry A* **2009**, *113* (16), 4691–4700. https://doi.org/10.1021/jp900230q.

(165) Hariharan, M.; Zheng, Y.; Long, H.; Zeidan, T. A.; Schatz, G. C.; Vura-Weis, J.; Wasielewski, M. R.; Zuo, X.; Tiede, D. M.; Lewis, F. D. Hydrophobic Dimerization and Thermal Dissociation of Perylenediimide-Linked DNA Hairpins. *Journal of the American Chemical Society* **2009**, *131* (16), 5920–5929. https://doi.org/10.1021/ja900347t.

(166) Neelakandan, P. P.; Zeidan, T. A.; McCullagh, M.; Schatz, G. C.; Vura-Weis, J.; Kim, C. H.; Wasielewski, M. R.; Lewis, F. D. Ground and Excited State Electronic Spectra of Perylenediimide

Dimers with Flexible and Rigid Geometries in DNA Conjugates. *Chemical Science* **2014**, *5* (3), 973–981. https://doi.org/10.1039/c3sc52908h.

(167) Zeidan, T. A.; Carmieli, R.; Kelley, R. F.; Wilson, T. M.; Lewis, F. D.; Wasielewski, M. R. Charge-Transfer and Spin Dynamics in Dna Hairpin Conjugates with Perylenediimide as a Base-Pair Surrogate. *Journal of the American Chemical Society* **2008**, *130* (42), 13945–13955. https://doi.org/10.1021/ja803765r.

(168) Takada, T.; Otsuka, Y.; Nakamura, M.; Yamana, K. Molecular Arrangement and Assembly Guided by Hydrophobic Cavities inside DNA. *Chemistry A European Journal* **2012**, *18* (30), 9300–9304. https://doi.org/10.1002/chem.201201469.

(169) Takada, T.; Ido, M.; Ashida, A.; Nakamura, M.; Fujitsuka, M. Photocurrent Generation through Charge-Transfer Processes in Noncovalent Perylenediimide / DNA Complexes. *Chemistry A European Journal* **2015**, *21* (18), 6846–6851. https://doi.org/10.1002/chem.201406592.

(170) Takada, T.; Ashida, A.; Nakamura, M.; Fujitsuka, M.; Majima, T.; Yamana, K. Photocurrent Generation Enhanced by Charge Delocalization over Stacked Perylenediimide Chromophores Assembled within DNA. *Journal of the American Chemical Society* **2014**, *136* (19), 6814–6817. https://doi.org/10.1021/ja501535z.

(171) Franceschin, M.; Bombelli, C.; Borioni, S.; Bozzuto, G.; Eleuteri, S.; Mancini, G.; Molinari, A.; Bianco, A. A New Perylene Bisimide Bola Amphiphile: Synthesis, Characterization, Fluorescent Properties and Applications as a Potential Probe. *New Journal of Chemistry* **2013**, *37* (7), 2166–2173. https://doi.org/10.1039/c3nj00116d.

(172) Fedoroff, O. Y.; Salazar, M.; Han, H.; Chemeris, V. v; Kerwin, S. M.; Hurley, L. H. NMR-Based Model of a Telomerase-Inhibiting Compound Bound to G-Quadruplex DNA. *Biochemistry* **1998**, *37* (36), 12367–12374. https://doi.org/10.1021/bi981330n.

(173) Rossetti, L.; Franceschin, M.; Bianco, A.; Ortaggi, G.; Savino, M. Perylene Diimides with Different Side Chains Are Selective in Inducing Different G-Quadruplex DNA Structures and in Inhibiting Telomerase. *Bioorganic and Medicinal Chemistry Letters* **2002**, *12* (18), 2527–2533. https://doi.org/10.1016/S0960-894X(02)00504-8.

(174) Kaewtunjai, N.; Summart, R.; Wongnoppavich, A.; Lojanapiwat, B.; Lee, T. R.; Tuntiwechapikul, W. Telomerase Inhibition, Telomere Shortening, and Cellular Uptake of the Perylene Derivatives PM2 and PIPER in Prostate Cancer Cells. *Biological and Pharmaceutical Bulletin* **2019**, *42* (6), 906–914. https://doi.org/10.1248/bpb.b18-00860.

(175) Kerwin, S. M.; Chen, G.; Kern, J. T.; Wang Thomas, P. Perylene Diimide G-Quadruplex DNA Binding Selectivity Is Mediated by Ligand Aggregation. *Bioorganic and Medicinal Chemistry Letters* **2002**, *12* (3), 447–450. https://doi.org/10.1016/S0960-894X(01)00775-2.

(176) Micheli, E.; Altieri, A.; Cianni, L.; Cingolani, C.; Iachettini, S.; Bianco, A.; Leonetti, C.; Cacchione, S.; Biroccio, A.; Franceschin, M.; Rizzo, A. Perylene and Coronene Derivatives Binding to G-Rich Promoter Oncogene Sequences Efficiently Reduce Their Expression in Cancer Cells. *Biochimie* **2016**, *125*, 223–231. https://doi.org/10.1016/j.biochi.2016.04.008.

(177) Xu, Z.; Cheng, W.; Guo, K.; Yu, J.; Shen, J.; Tang, J.; Yang, W.; Yin, M. Molecular Size, Shape, and Electric Charges: Essential for Perylene Bisimide-Based DNA Intercalator to Localize in Cell Nuclei and Inhibit Cancer Cell Growth. *ACS Applied Materials and Interfaces* **2015**, *7* (18), 9784–9791. https://doi.org/10.1021/acsami.5b01665.

(178) Xu, Z.; Guo, K.; Yu, J.; Sun, H.; Tang, J.; Shen, J.; Müllen, K.; Yang, W.; Yin, M. A Unique Perylene-Based DNA Intercalator: Localization in Cell Nuclei and Inhibition of Cancer Cells and Tumors. *Small* **2014**, *10* (20), 4087–4092. https://doi.org/10.1002/smll.201401262.

(179) Jiao, Y.; Liu, K.; Wang, G.; Wang, Y.; Zhang, X. Supramolecular Free Radicals: Near-Infrared Organic Materials with Enhanced Photothermal Conversion. *Chemical Science* **2015**, *6* (7), 3975–3980. https://doi.org/10.1039/c5sc01167a.

(180) Lü, B.; Chen, Y.; Li, P.; Wang, B.; Müllen, K.; Yin, M. Stable Radical Anions Generated from a Porous Perylenediimide Metal-Organic Framework for Boosting near-Infrared Photothermal Conversion. *Nature Communications* **2019**, *10* (1). https://doi.org/10.1038/s41467-019-08434-4.

(181) Sun, P.; Wang, X.; Wang, G.; Deng, W.; Shen, Q.; Jiang, R.; Wang, W.; Fan, Q.; Huang, W. A Perylene Diimide Zwitterionic Polymer for Photoacoustic Imaging Guided Photothermal/Photodynamic Synergistic Therapy with Single near-Infrared Irradiation. *Journal of Materials Chemistry B* **2018**, *6* (20), 3395–3403. https://doi.org/10.1039/c8tb00845k.

(182) Li, H.; Yue, L.; Li, L.; Liu, G.; Zhang, J.; Luo, X.; Wu, F. Triphenylamine-Perylene Diimide Conjugate-Based Organic Nanoparticles for Photoacoustic Imaging and Cancer Phototherapy. *Colloids and Surfaces B: Biointerfaces* **2021**, *205*. https://doi.org/10.1016/j.colsurfb.2021.111841.

(183) Gong, Q.; Xing, J.; Huang, Y.; Wu, A.; Yu, J.; Zhang, Q. Perylene Diimide Oligomer Nanoparticles with Ultrahigh Photothermal Conversion Efficiency for Cancer Theranostics. *ACS Applied Bio Materials* **2020**, *3* (3), 1607–1615. https://doi.org/10.1021/acsabm.9b01187.

(184) Yang, Y.; He, P.; Wang, Y.; Bai, H.; Wang, S.; Xu, J.; Zhang, X. Supramolecular Radical Anions Triggered by Bacteria In Situ for Selective Photothermal Therapy. *Angewandte Chemie International Edition* **2017**, *56* (51), 16239–16242. https://doi.org/10.1002/anie.201708971.

(185) Barrio, D.; Ghosh, I.; Biedermann, F.; Lazar, A. I.; Lan, Y.; Coulston, R. J.; Nau, W. M.; Scherman, O. A. Efficient Host–Guest Energy Transfer in Polycationic Cyclophane–Perylene Diimide Complexes in Water. *Journal of the American Chemical Society* **2014**, *136* (25), 9053–9060. https://doi.org/10.1021/ja5032437.

(186) Feldman, D.; Margolis, R. *Q4 2019/Q1 2020 Solar Industry Update*; 2019.

(187) Sani, F.; Shafie, S.; Lim, H. N.; Musa, A. O. Advancement on Lead-Free Organic-Inorganic Halide Perovskite Solar Cells: A Review. *Materials* **2018**, *11* (6), 1–17. https://doi.org/10.3390/ma11061008.

(188) Xue, R.; Zhang, J.; Li, Y.; Li, Y. Organic Solar Cell Materials toward Commercialization. *Small* **2018**, *14* (41). https://doi.org/10.1002/smll.201801793.

(189) Kang, Q.; Ye, L.; Xu, B.; An, C.; Stuard, S. J.; Zhang, S.; Yao, H.; Ade, H.; Hou, J. A Printable Organic Cathode Interlayer Enables over 13% Efficiency for 1-Cm 2 Organic Solar Cells. *Joule* **2019**, *3* (1), 227–239. https://doi.org/10.1016/j.joule.2018.10.024.

(190) Li, C. Z.; Chueh, C. C.; Yip, H. L.; O'Malley, K. M.; Chen, W. C.; Jen, A. K. Y. Effective Interfacial Layer to Enhance Efficiency of Polymer Solar Cells via Solution-Processed Fullerene-Surfactants. *Journal of Materials Chemistry* **2012**, *22* (17), 8574–8578. https://doi.org/10.1039/c2jm30755c.

(191) Jia, T.; Sun, C.; Xu, R.; Chen, Z.; Yin, Q.; Jin, Y.; Yip, H. L.; Huang, F.; Cao, Y. Naphthalene Diimide Based N-Type Conjugated Polymers as Efficient Cathode Interfacial Materials for Polymer and Perovskite Solar Cells. *ACS Applied Materials and Interfaces* **2017**, *9* (41), 36070–36081. https://doi.org/10.1021/acsami.7b10365.

(192) Jin, X.; Wang, Y.; Cheng, X.; Zhou, H.; Hu, L.; Zhou, Y.; Chen, L.; Chen, Y. Fluorine-Induced Self-Doping and Spatial Conformation in Alcohol-Soluble Interlayers for Highly-Efficient Polymer Solar Cells. *Journal of Materials Chemistry A* **2018**, *6* (2), 423–433. https://doi.org/10.1039/c7ta08669e.

(193) Yin, X.; Liu, X.; Peng, Y.; Zeng, W.; Zhong, C.; Xie, G.; Wang, L.; Fang, J.; Yang, C. Multichannel Strategies to Produce Stabilized Azaphenalene Diradicals: A Predictable Model to Generate Self-Doped Cathode Interfacial Layers for Organic Photovoltaics. *Advanced Functional Materials* **2019**, *29* (4). https://doi.org/10.1002/adfm.201806125.

(194) Liu, Y.; Sheri, M.; Cole, M. D.; Yu, D. M.; Emrick, T.; Russell, T. P. Transforming Ionene Polymers into Efficient Cathode Interlayers with Pendent Fullerenes. *Angewandte Chemie* **2019**, *131* (17), 5733–5737. https://doi.org/10.1002/ange.201901536.

(195) Sorrentino, R.; Kozma, E.; Luzzati, S.; Po, R. Interlayers for Non-Fullerene Based Polymer Solar Cells: Distinctive Features and Challenges. *Energy and Environmental Science*. Royal Society of Chemistry January 1, 2021, pp 180–223. https://doi.org/10.1039/d0ee02503h.

(196) Hu, Z.; Xu, R.; Dong, S.; Lin, K.; Liu, J.; Huang, F.; Cao, Y. Quaternisation-Polymerized N-Type Polyelectrolytes: Synthesis, Characterisation and Application in High-Performance Polymer Solar Cells. *Materials Horizons* **2017**, *4* (1), 88–97. https://doi.org/10.1039/c6mh00434b.

(197) Supur, M.; Kawashima, Y.; Mase, K.; Ohkubo, K.; Hasobe, T.; Fukuzumi, S. Broadband Light Harvesting and Fast Charge Separation in Ordered Self-Assemblies of Electron Donor–Acceptor-Functionalized Graphene Oxide Layers for Effective Solar Energy Conversion. *Journal of Physical Chemistry C* **2015**, *119* (24), 13488–13495. https://doi.org/10.1021/acs.jpcc.5b03303.

(198) Chen, Q.; Worfolk, B. J.; Hauger, T. C.; Al-Atar, U.; Harris, K. D.; Buriak, J. M. Finely Tailored Performance of Inverted Organic Photovoltaics through Layer-by-Layer Interfacial Engineering. *ACS Applied Materials and Interfaces* **2011**, *3* (10), 3962–3970. https://doi.org/10.1021/am200849r.

(199) Xie, Z.; Xiao, B.; He, Z.; Zhang, W.; Wu, X.; Wu, H.; Würthner, F.; Wang, C.; Xie, F.; Liu, L.; Ma, Y.; Wong, W. Y.; Cao, Y. Self-Assembled Perylene Bisimide J-Aggregates as Promising Cathode Modifiers for Highly Efficient Inverted Polymer Solar Cells. *Materials Horizons* **2015**, *2* (5), 514–518. https://doi.org/10.1039/c5mh00056d.

(200) Zhang, Z. G.; Qi, B.; Jin, Z.; Chi, D.; Qi, Z.; Li, Y.; Wang, J. Perylene Diimides: A Thickness-Insensitive Cathode Interlayer for High Performance Polymer Solar Cells. *Energy and Environmental Science* **2014**, *7* (6), 1966–1973. https://doi.org/10.1039/c4ee00022f.

(201) Qiu, B.; Yuan, J.; Xiao, X.; He, D.; Qiu, L.; Zou, Y.; Zhang, Z. G.; Li, Y. Effect of Fluorine Substitution on Photovoltaic Properties of Alkoxyphenyl Substituted Benzo[1,2-b:4,5-B']Dithiophene-Based Small Molecules. *ACS Applied Materials and Interfaces* **2015**, *7* (45), 25237–25246. https://doi.org/10.1021/acsami.5b07066.

(202) Weng, C.; Gao, L.; Zhang, Z.; Liu, Z.; Tan, S.; Li, Y. A New Polymer Acceptor Containing Naphthalene Diimide and 1,3,4-Thiadiazole for All-Polymer Solar Cells. *Journal of Polymer Science, Part B: Polymer Physics* **2017**, *55* (13), 990–996. https://doi.org/10.1002/polb.24347.

(203) Song, C.; Liu, X.; Li, X.; Wang, Y. C.; Wan, L.; Sun, X.; Zhang, W.; Fang, J. Perylene Diimide-Based Zwitterion as the Cathode Interlayer for High-Performance Nonfullerene Polymer Solar Cells. *ACS Applied Materials and Interfaces* **2018**, *10* (17), 14986–14992. https://doi.org/10.1021/acsami.8b01147.

(204) Ye, Y.; Lü, B.; Cheng, W.; Wu, Z.; Wei, J.; Yin, M. Controllable Self-Assembly of Amphiphilic Zwitterionic PBI Towards Tunable Surface Wettability of the Nanostructures. *Chemistry - An Asian Journal* **2017**, *12* (9), 1020–1024. https://doi.org/10.1002/asia.201700246.

(205) Min, J.; Zhang, Z.; Hou, Y.; Omar, C.; Quiroz, R.; Przybilla, T.; Bronnbauer, C.; Guo, F.; Forberich, K.; Azimi, H.; Ameri, T.; Spiecker, E.; Li, Y.; Brabec, C. J. Interface Engineering of Perovskite Hybrid Solar Cells with Solution- Processed Perylene – Diimide Heterojunctions toward High Performance. *Chemistry of Materials* **2015**, *27* (1), 227–234. https://doi.org/10.1021/cm5037919.

(206) Wang, H.; Song, J.; Qu, J.; Lian, J.; Qian, P.-C.; Wong, W.-Y. R. A Novel Perylene Diimide-Based Zwitterion as the Cathode Interlayer for High-Performance Perovskite Solar Cells. *Journal of Materials Chemistry A* **2020**, *8*, 18117–18124. https://doi.org/10.1039/d0ta06006b.

(207) Freer, R.; Powell, A. v. Realising the Potential of Thermoelectric Technology: A Roadmap. *Journal of Materials Chemistry C* **2020**, *8* (2), 441–463. https://doi.org/10.1039/c9tc05710b.

(208) Zevalkink, A.; Smiadak, D. M.; Blackburn, J. L.; Ferguson, A. J.; Chabinyc, M. L.; Delaire, O.; Wang, J.; Kovnir, K.; Martin, J.; Schelhas, L. T.; Sparks, T. D.; Kang, S. D.; Dylla, M. T.; Snyder, G. J.; Ortiz, B. R.; Toberer, E. S. A Practical Field Guide to Thermoelectrics: Fundamentals, Synthesis, and Characterization. *Applied Physics Reviews* **2018**, *5* (2). https://doi.org/10.1063/1.5021094.

(209) Kroon, R.; Mengistie, D. A.; Kiefer, D.; Hynynen, J.; Ryan, J. D.; Yu, L.; Müller, C. Thermoelectric Plastics: From Design to Synthesis, Processing and Structure-Property Relationships. *Chemical Society Reviews* **2016**, *45* (22), 6147–6164. https://doi.org/10.1039/c6cs00149a.

(210) Zuo, G.; Li, Z.; Wang, E.; Kemerink, M. High Seebeck Coefficient and Power Factor in N-Type Organic Thermoelectrics. *Advanced Electronic Materials* **2018**, *4* (1), 1–6. https://doi.org/10.1002/aelm.201700501.

(211)   Chen, Y.; Zhao, Y.; Liang, Z. Solution Processed Organic Thermoelectrics: Towards Flexible Thermoelectric Modules. *Energy & Environmental Science* **2015**, *8* (2), 401–422. https://doi.org/10.1039/C4EE03297G.

(212)   Lin, S.; Li, W.; Chen, Z.; Shen, J.; Ge, B.; Pei, Y. Tellurium as a High-Performance Elemental Thermoelectric. *Nature communications* **2016**, *7*, 10287. https://doi.org/10.1038/ncomms10287.

(213)   Cowen, L. M.; Atoyo, J.; Carnie, M. J.; Baran, D.; Schroeder, B. C. Review—Organic Materials for Thermoelectric Energy Generation. *ECS Journal of Solid State Science and Technology* **2017**, *6* (3), N3080–N3088. https://doi.org/10.1149/2.0121703jss.

(214)   Kim, G.-H.; Shao, L.; Zhang, K.; Pipe, K. P. Engineered Doping of Organic Semiconductors for Enhanced Thermoelectric Efficiency. *Nature materials* **2013**, *12* (8). https://doi.org/10.1038/nmat3635.

(215)   Chabinyc, M. Thermoelectric Polymers: Behind Organics' Thermopower. *Nature Materials* **2014**, *13* (2), 119–121. https://doi.org/10.1038/nmat3859.

(216)   Sato, R.; Kiyota, Y.; Kadoya, T.; Kawamoto, T.; Mori, T. Thermoelectric Power of Oriented Thin-Film Organic Conductors. *RSC Advances* **2016**, *6*, 41040–41044. https://doi.org/10.1039/C6RA04455G.

(217)   Kim, G.; Pipe, K. P. Thermoelectric Model to Characterize Carrier Transport in Organic Semiconductors. *Physical Review B - Condensed Matter and Materials Physics* **2012**, *86* (8), 1–5. https://doi.org/10.1103/PhysRevB.86.085208.

(218)   Wang, D.; Shi, W.; Chen, J.; Xi, J.; Shuai, Z. Modeling Thermoelectric Transport in Organic Materials. *Physical chemistry chemical physics : PCCP* **2012**, *14* (48), 16505–16520. https://doi.org/10.1039/c2cp42710a.

(219)   Lüssem, B.; Riede, M.; Leo, K. Doping of Organic Semiconductors. *Physica Status Solidi A* **2013**, *210* (1), 9–43. https://doi.org/10.1002/pssa.201228310.

(220)   Dongmin Kang, S.; Jeffrey Snyder, G. Charge-Transport Model for Conducting Polymers. *Nature Materials* **2016**, *16* (2), 252–257. https://doi.org/10.1038/nmat4784.

(221)   Snyder, G. J.; Toberer, E. S. Complex Thermoelectric Materials. *Nature materials* **2008**, *7* (2), 105–114. https://doi.org/10.1038/nmat2090.

(222)   Lu, Y.; Chen, J. Prospects of Organic Electrode Materials for Practical Lithium Batteries. *Nature Reviews Chemistry* **2020**, *4* (3), 127–142. https://doi.org/10.1038/s41570-020-0160-9.

(223)   Muench, S.; Wild, A.; Friebe, C.; Häupler, B.; Janoschka, T.; Schubert, U. S. Polymer-Based Organic Batteries. *Chemical Reviews* **2016**, *116* (16), 9438–9484. https://doi.org/10.1021/acs.chemrev.6b00070.

(224)   Bhosale, M. E.; Krishnamoorthy, K. Chemically Reduced Organic Small-Molecule-Based Lithium Battery with Improved Efficiency. *Chemistry of Materials* **2015**, *27* (6), 2121–2126. https://doi.org/10.1021/cm5046786.

(225) Zhao, Q.; Guo, C.; Lu, Y.; Liu, L.; Liang, J.; Chen, J. Rechargeable Lithium Batteries with Electrodes of Small Organic Carbonyl Salts and Advanced Electrolytes. *Industrial and Engineering Chemistry Research* **2016**, *55* (20), 5795–5804. https://doi.org/10.1021/acs.iecr.6b01462.

(226) Supur, M.; Ohkubo, K.; Fukuzumi, S. Photoinduced Charge Separation in Ordered Self-Assemblies of Perylenediimide-Graphene Oxide Hybrid Layers. *Chemical Communications* **2014**, *50* (87), 13359–13361. https://doi.org/10.1039/c4cc05694a.

(227) Deng, W.; Yu, J.; Qian, Y.; Wang, R.; Ullah, Z.; Zhu, S.; Chen, M.; Li, W.; Guo, Y.; Li, Q.; Liu, L. Strongly Coupled Perylene Bisimide / Reduced Graphene Oxide as Organic Cathode Materials for Lithium Ion Batteries. *Electrochimica Acta* **2018**, *282*, 24–29. https://doi.org/10.1016/j.electacta.2018.06.033.

(228) Zhao, Y.; Ding, Y.; Li, Y.; Peng, L.; Byon, H. R.; Goodenough, J. B.; Yu, G. A Chemistry and Material Perspective on Lithium Redox Flow Batteries towards High-Density Electrical Energy Storage. *Chemical Society Reviews* **2015**, *44* (22), 7968–7996. https://doi.org/10.1039/c5cs00289c.

(229) Rhodes, Z.; Cabrera-Pardo, J. R.; Li, M.; Minteer, S. D. Electrochemical Advances in Non-Aqueous Redox Flow Batteries. *Israel Journal of Chemistry*. John Wiley and Sons Inc January 1, 2021, pp 101–112. https://doi.org/10.1002/ijch.202000049.

(230) Ding, Y.; Yu, G. The Promise of Environmentally Benign RedoxFlow Batteries by Molecular Engineering. *Angewandte Chemie* **2017**, *129* (30), 8738–8740. https://doi.org/10.1002/ange.201701254.

(231) Milton, M.; Cheng, Q.; Yang, Y.; Nuckolls, C.; Hernández Sánchez, R.; Sisto, T. J. Molecular Materials for Nonaqueous Flow Batteries with a High Coulombic Efficiency and Stable Cycling. *Nano Letters* **2017**, *17* (12), 7859–7863. https://doi.org/10.1021/acs.nanolett.7b04131.

(232) Zhang, B.; Sun, L. Artificial Photosynthesis: Opportunities and Challenges of Molecular Catalysts. *Chemical Society Reviews* **2019**, *48* (7), 2216–2264. https://doi.org/10.1039/c8cs00897c.

(233) Balzani, V.; Credi, A.; Venturi, M. Photochemical Conversion of Solar Energy. *ChemSusChem* **2008**, *1* (1–2), 26–58. https://doi.org/10.1002/cssc.200700087.

(234) Hore, P. J.; Ivanov, K. L.; Wasielewski, M. R. Spin Chemistry. *Journal of Chemical Physics* **2020**, *152* (12). https://doi.org/10.1063/5.0006547.

(235) Kirner, J. T.; Finke, R. G. Water-Oxidation Photoanodes Using Organic Light-Harvesting Materials: A Review. *Journal of Materials Chemistry A* **2017**, *5* (37), 19560–19592. https://doi.org/10.1039/c7ta05709a.

(236) Novák, P.; Müller, K.; Santhanam, K. S. v; Haas, O. Electrochemically Active Polymers for Rechargeable Batteries. *Chemical Reviews* **1997**, *97* (1), 207–281. https://doi.org/https://doi.org/10.1021/cr941181o.

(237) Berardi, S.; Cristino, V.; Canton, M.; Boaretto, R.; Argazzi, R.; Benazzi, E.; Ganzer, L.; Borrego Varillas, R.; Cerullo, G.; Syrgiannis, Z.; Rigodanza, F.; Prato, M.; Bignozzi, C. A.; Caramori, S. Perylene Diimide Aggregates on Sb-Doped SnO2: Charge Transfer Dynamics Relevant to Solar

Fuel Generation. *Journal of Physical Chemistry C* **2017**, *121* (33), 17737–17745. https://doi.org/10.1021/acs.jpcc.7b05928.

(238) Benazzi, E.; Rettenmaier, K.; Berger, T.; Caramori, S.; Berardi, S.; Argazzi, R.; Prato, M.; Syrgiannis, Z. Photoelectrochemical Properties of SnO2 Photoanodes Sensitized by Cationic Perylene-Di-Imide Aggregates for Aqueous HBr Splitting. *Journal of Physical Chemistry C* **2020**, *124* (2), 1317–1329. https://doi.org/10.1021/acs.jpcc.9b11039.

(239) Yang, L.; Wang, M.; Slattum, P. M.; Bunes, B. R.; Wang, Y.; Wang, C.; Zang, L. Donor-Acceptor Supramolecular Organic Nanofibers as Visible-Light Photoelectrocatalysts for Hydrogen Production. *ACS Applied Materials and Interfaces* **2018**, *10* (23), 19764–19772. https://doi.org/10.1021/acsami.8b05637.

(240) Kirner, J. T.; Stracke, J. J.; Gregg, B. A.; Finke, R. G. Visible-Light-Assisted Photoelectrochemical Water Oxidation by Thin Films of a Phosphonate-Functionalized Perylene Diimide plus CoOx Cocatalyst. *ACS Applied Materials and Interfaces* **2014**, *6* (16), 13367–13377. https://doi.org/10.1021/am405598w.

(241) Liu, Y.; Guo, S. X.; Bond, A. M.; Zhang, J.; Geletii, Y. v.; Hill, C. L. Voltammetric Determination of the Reversible Potentials for [{Ru 4O4(OH)2(H2O)4}(γ- SiW10O36)2]10- over the PH Range of 2-12: Electrolyte Dependence and Implications for Water Oxidation Catalysis. *Inorganic Chemistry* **2013**, *52* (20), 11986–11996. https://doi.org/10.1021/ic401748y.

(242) Lai, Y. H.; Kato, M.; Mersch, D.; Reisner, E. Comparison of Photoelectrochemical Water Oxidation Activity of a Synthetic Photocatalyst System with Photosystem II. *Faraday Discussions* **2014**, *176*, 199–211. https://doi.org/10.1039/c4fd00059e.

(243) Fielden, J.; Sumliner, J. M.; Han, N.; Geletii, Y. v.; Xiang, X.; Musaev, D. G.; Lian, T.; Hill, C. L. Water Splitting with Polyoxometalate-Treated Photoanodes: Enhancing Performance through Sensitizer Design. *Chemical Science* **2015**, *6* (10), 5531–5543. https://doi.org/10.1039/c5sc01439e.